University of Alberta

The structure and controlled relaminarization of low momentum elevated jets-in-crossflow

by

Graeme Mark Glean Watson ©

A thesis submitted to the Faculty of Graduate Studies and Research in
partial fulfillment of the requirements for the degree of Master of Science.

Department of Mechanical Engineering

Edmonton, Alberta
Fall 2007

Library and
Archives Canada

Published Heritage
Branch

395 Wellington Street
Ottawa ON K1A 0N4
Canada

Bibliothèque et
Archives Canada

Direction du
Patrimoine de l'édition

395, rue Wellington
Ottawa ON K1A 0N4
Canada

Your file Votre référence
ISBN: 978-0-494-33367-9
Our file Notre référence
ISBN: 978-0-494-33367-9

NOTICE:
The author has granted a non-exclusive license allowing Library and Archives Canada to reproduce, publish, archive, preserve, conserve, communicate to the public by telecommunication or on the Internet, loan, distribute and sell theses worldwide, for commercial or non-commercial purposes, in microform, paper, electronic and/or any other formats.

The author retains copyright ownership and moral rights in this thesis. Neither the thesis nor substantial extracts from it may be printed or otherwise reproduced without the author's permission.

AVIS:
L'auteur a accordé une licence non exclusive permettant à la Bibliothèque et Archives Canada de reproduire, publier, archiver, sauvegarder, conserver, transmettre au public par télécommunication ou par l'Internet, prêter, distribuer et vendre des thèses partout dans le monde, à des fins commerciales ou autres, sur support microforme, papier, électronique et/ou autres formats.

L'auteur conserve la propriété du droit d'auteur et des droits moraux qui protège cette thèse. Ni la thèse ni des extraits substantiels de celle-ci ne doivent être imprimés ou autrement reproduits sans son autorisation.

In compliance with the Canadian Privacy Act some supporting forms may have been removed from this thesis.

While these forms may be included in the document page count, their removal does not represent any loss of content from the thesis.

Conformément à la loi canadienne sur la protection de la vie privée, quelques formulaires secondaires ont été enlevés de cette thèse.

Bien que ces formulaires aient inclus dans la pagination, il n'y aura aucun contenu manquant.

Canada

ABSTRACT

The structure and controlled relaminarization of low momentum and Reynolds number elevated jets-in-crossflow (JICFs) are discussed. The unforced JICF is unstable except at a single jet-to-crossflow velocity ratio $R = 1.13 \pm 0.09$ where the jet shear layer is completely stable in the near field. Control is via a synthetic jet from an annular slit coaxially surrounding the jet flow. In an unstable regime, $R < 1.13$, where there is formation of strong jet shear layer instabilities, the synthetic jet can suppress them. The synthetic jet reduces the local Reynolds number of the wake-like profile between the free stream and jet flow below critical values for the growth of an unstable flow structure. The control mechanism has many similarities to base bleed suppression of Kármán vortex shedding in supercritical bluff bodies. It is demonstrated that base bleed is also a viable method for JICF control. Parts of the 3-D large-scale structure of the unforced jet shear layer vortices are also digitized with stereoscopic imaging and an Augmented Reality interface for proposal of a jet shear layer vortex skeleton model.

ACKNOWLEDGEMENTS

I received a tremendous amount of help and support over the course of this project. The project would not have been completed without the following.

I have benefited greatly from the knowledge and expertise of my advisor Dr Lorenz Sigurdson. He provided the inspiration for this project and critical guidance for all stages.

I also wish to thank other members of the Vortex Fluid Dynamics Lab (VFDL). Especially Stuart Gilbert, Justin Wiwchar and Aaron Baugh for many helpful discussions and their suggestions. Thanks go also to previous VFDL members John Diep, Chris Apps and Dr Tony Chen whose initial work and measurement techniques were especially important in understanding the phenomena.

The VFDL hosts student research scholars in the school year and during the summer, many of whom offered assistance as well as invaluable ideas. Thanks to Christopher Strand, Ryan Tucker, Joshua Nault, Jordan Leung, Nesma Ansari, Chris Ausford and Wafaa Hajar.

Special thanks to the machinists, technicians and office staff in the Department of Mechanical Engineering. Finally, I thank my family for their constant support over these years, especially Patricia Pernica whose support and advice were critical to completing this degree.

Financial support from Luscar Ltd., the R. R. Gilpin Memorial Scholarship, the University of Alberta, and from National Sciences and Engineering Research Council operating grants is also gratefully acknowledged.

CONTENTS

1 Introduction 1
- 1.1 JICF Parameters Considered 3
- 1.2 Formation and Evolution of JICF Vortex Structures 3
- 1.3 Relaminarization 4
- 1.4 Three-Dimensional JICF Large-Scale Structures 5

2 Formation and Evolution of Vortices 10
- 2.1 Introduction 10
- 2.2 Background 11
  - 2.2.1 Coherent Structures 11
  - 2.2.2 The Forced Jet-in-Crossflow 12
- 2.3 Method 13
  - 2.3.1 The Apparatus 13
  - 2.3.2 Flow Visualization 13
  - 2.3.3 Measurement of JICF Operating Points 14
- 2.4 Results and Discussion 15
  - 2.4.1 The Low Velocity Ratio Regime 15
  - 2.4.2 The High Velocity Ratio Regime 27
- 2.5 Summary and Conclusions 32

3 JICF Instability Suppression 37
- 3.1 Introduction and Background 37
- 3.2 Experimental Setup 42
  - 3.2.1 The Apparatus 42
  - 3.2.2 Flow Visualization 43
  - 3.2.3 Hot-Wire Measurements 44
  - 3.2.4 Image Correlation Velocimetry 46
  - 3.2.5 JICF Momentum Ratios 47

3.2.6 Coordinate Systems 50
3.3 The Relaminarization Phenomenon 51
3.4 Testing the Limits of the Relaminarization Phenomenon . . . 57
3.4.1 The Experiment 57
3.4.2 Synthetic Jet Measurements 58
3.4.3 Results 59
3.5 JICF Operating Points 62
3.6 Results and Discussion 65
3.6.1 Jet Velocity Profiles 65
3.6.2 Vector Field Measurements 68
3.6.3 Time-Averaged Jet Shear Layer Velocity Profiles 73
3.6.4 Critical Reynolds Numbers 80
3.6.5 Base Bleed 84
3.7 Summary and Conclusions 88

4 Digitization of JICF Vortex Structure **95**
4.1 Acknowledgements for Chapter 4 95
4.2 Introduction 95
4.3 Experimental Setup 98
4.3.1 JICF Apparatus 98
4.3.2 Stereo Image Capture 99
4.3.3 Stereo Extraction Software 99
4.4 Results and Discussion 100
4.5 Conclusions 107

5 Summary and Conclusions **113**
5.1 Formation and Evolution of the JICF Vortices 113
5.2 Relaminarization of the Elevated JICF 114
5.3 Digitization of the Three-Dimensional Large-Scale Structures . 116
5.4 Further Research 116

A Low Speed Hot-wire Calibration **120**
A.1 Background 120
A.2 Method and Results 121

B JICF Trajectories **126**
B.1 Background 126
B.2 Determining JICF Trajectories 127

B.3 Results and Discussion 129

LIST OF TABLES

3.1 Experimental Operating Parameters 63
3.2 Approximate Reynolds Numbers Computed from Velocity Profiles of the Jet Shear Layer at $s/D = 0.1$, $1.17 \leq R \leq 0.61$ . . 83
3.3 Summary of Critical Bleed Coefficients 87

B.1 Comparison of Scalar and Velocity Centrelines 133

LIST OF FIGURES

1.1 Schematic of jet-in-crossflow geometries 2

2.1 Change in structure of a forced low momentum JICF, $R < 1.13$ 19
2.2 Change in structure of an unforced low momentum JICF, $R < 1.13$ 26
2.3 Schematics of the pointing transitions that occur in the unforced and forced JICFs 28
2.4 Change in Structure of a forced JICF, $R > 1.13$ 30

3.1 Schematic of the apparatus 43
3.2 A sample image pair with time lapsed triggering of red/blue strobes 48
3.3 Coordinate systems 50
3.4 Photographs of some of the unforced JICF jet shear layer structures for the range of velocity ratios $1.36 \leq R \leq 0.69$ . . . 53
3.5 Change in structure of a low momentum elevated JICF via 60 Hz synthetic jet forcing with increasing amplitude 56
3.6 Hydrodynamic impulse verses Strouhal number 61
3.7 Visual representation of the operating parameters 64
3.8 Jet velocity and turbulence intensity profiles in no crossflow, $R \to \infty$. 66
3.9 Jet velocity and turbulence intensity profiles for unstable and relaminarized JICFs, cases BA and BC. 67
3.10 Time-averaged vector field for case AA 69
3.11 Comparison of time-averaged vector field for the unsteady and relaminarized 'B' series cases 70
3.12 Schematic of locations of velocity profiles for case BA 74
3.13 Evolution of time-averaged velocity profiles along the jet trajectory for case BA 76

3.14 Schematic of local upstream jet shear layer velocity profile parameters 78
3.15 Velocity differences, ΔU, as a function of velocity ratio, R . . 79
3.16 Changes in the local Reynolds numbers, Re_δ, with velocity ratio, R 81
3.17 A comparison of synthetic jet and based bleed suppression of the jet shear layer instability 86

4.1 Side-view photograph of jet shear layer, $R = 0.81$ 104
4.2 Stereoscopic visualization of the jet shear layer vortex structure 105
4.3 The vortex skeleton model 106
4.4 Analglyph image of the jet shear layer vortex structure 108
4.5 Anaglyph image of the vortex skeleton model 109

A.1 Low speed hot-wire calibration curve, 0 m/s $\leq U \leq$ 3 m/s . . 123

B.1 Sample image used to determine the JICF trajectory 128
B.2 Comparison of approximate unforced JICF trajectories 130
B.3 Comparison of approximate trajectories of a forced JICF, $R =$ 0.65 132

NOMENCLATURE

A_j	initial jet area at the stack exit plane
A_m	momentum-weighted area
A_{sj}	area of the synthetic jet annulus
C_b	critical bleed coefficient with base bleed
C_{sj}	critical bleed coefficient with a synthetic jet
D	outer stack diameter
d	inner stack diameter and initial jet diameter
E	hot-wire bridge voltage
F_j	jet momentum flux
F_{sj}	synthetic jet momentum flux
F_t	total momentum flux applied over the whole stack exit
f_n	frequency of large scale jet shear layer vortex structures
f_{sj}	synthetic jet frequency
H	outer annulus width

h	inner annulus width
I_o	impulse of the vortex pair formed during the synthetic jet ejection cycle, per per unit depth
L_o	slug length
M_M	momentum velocity ratio using the momentum-weighted area
R	jet-to-crossflow velocity ratio
Re_c	Reynolds number for lower limit of forced convection regime based on hot-wire diameter and cross-stream velocity
Re_d	jet Reynolds number based on jet diameter, d, and the spatially averaged jet velocity, W_j
$\mathrm{Re}_{d,\mathrm{crit}}$	critical jet Reynolds number for transition to turbulence
Re_H	approximate global Reynolds number of the jet shear layer based on outer annulus width, H, and the average peak velocity of the jet shear layer profile, U_p
Re_{I_o}	Reynolds number based on impulse of vortex pair per unit depth, I_o, and the inner annulus width, h
Re_{U_o}	synthetic jet Reynolds number based on the inner annulus width, h and the slug velocity, U_o

Re_δ	local Reynolds number of the jet shear layer based on local jet shear layer viscous thickness, δ and the velocity deficit of the local profile, $\Delta U_{profile}$
$\mathrm{Re}_{\delta,\mathrm{crit}}$	local jet shear layer Reynolds number necessary for relaminarization, based on local jet shear layer viscous thickness, δ and the velocity deficit of the local profile, $\Delta U_{profile}$
Re_∞	crossflow Reynolds number based on outer stack diameter, D, and the crossflow velocity, U_∞
St_d	Strouhal number of the jet shear layer vortex structures based on jet diameter, d
u	horizontal velocity at a point
U_o	slug velocity
U_p	potential flow decomposition in local wake flow velocity profile
U_∞	uniform, horizontal crossflow velocity
w	vertical velocity at a point
$w_{sj,o}$	centreline synthetic jet velocity
$w_{sj,max}$	maximum centreline ejection velocity in the synthetic jet cycle
W_j	spatially averaged mean jet velocity determined from a parabolic jet profile

W_o	synthetic jet slug velocity
W_{sj}	temporal averaged synthetic jet velocity measured along the centreline at $z/h = 2$
α	momentum flux correction factor. $\alpha = 4/3$ for an axi-symmetry parabolic profile
ΔU_{peak}	local velocity difference between the peaks in the jet shear layer velocity profile
$\Delta U_{profile}$	local velocity deficit within the jet shear layer velocity profile
Δt	time difference
δ	local thickness of jet shear layer
ρ_j	density of jet gases
ρ_∞	density of crossflow gases

subscripts:

b	base bleed
crit	critical, related to onset of instabilities and transition to turbulence
j	jet
max	maximum
o	centreline value, at exit plane
$peak$	peak velocities in the local jet shear layer profile
$profile$	the whole local jet shear layer profile
sj	synthetic jet
t	total
∞	crossflow

CHAPTER 1

INTRODUCTION

The flow field created by a jet which emits from an opening normal to a cross-stream has received considerable attention due to its widespread applications. For research purposes, it is common practice to simplify things by dividing the jet-in-crossflow, hence termed JICF, into two categories according to differences in the geometry of the jet exit, as seen in Figure 1.1. The jet may emit from an orifice flush with a wall or from an elevated position through a stack, however in real-world applications the geometry could be some combination of these. JICFs are in a variety of applications. They are encountered in aeronautics systems (vertical/short takeoff and landing and guidance systems), combustion applications (Broadwell and Breidenthal, 1984) and cooling (Haven and Kurosaka, 1996). The flow also arises in situations in the environmental field, notability in plume dispersion (Moussa et al., 1977) and stack flares (Johnson and Kostiuk, 2000).

JICF research spans over many decades – a review of the seminal findings are in Margason (1993). Substantial progress has been made in determining the gross characteristics of the flow field. Early studies focused on defining turbulence characteristics (Andreopoulos and Rodi, 1984; Smith and Mungal, 1998), and on developing scaling laws and models for the JICF trajectory (Briggs, 1975; Pratte and Baines, 1967; Keffer and Baines, 1963; Johnston and Wilson, 1997; Su and Mungal, 2004; Hasslebrink and Mungal, 2001). Since then, there has been an increased understanding of vorticity generation in the flow through experimentation (Fric and Roshko, 1994; Kelso et al., 1996; Eiff and Keffer, 1997; Lim et al., 2001; Huang and Lan, 2005) and computation (Cortelezzi and Karagozian, 2001; Marzouk and Ghoniem, 2007). Among the jet phenomena discovered by researchers are the formations of a range of large-scale vortical structures which strongly influence the jets be-

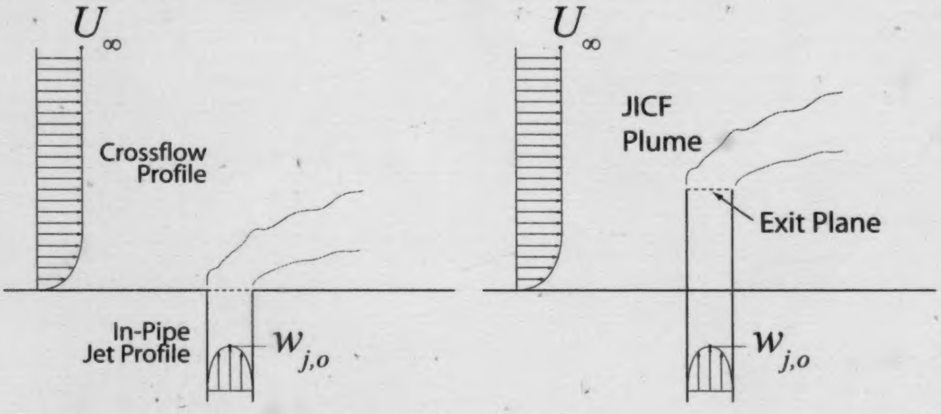

(a) (b)

Figure 1.1: Schematic of simplified jet-in-crossflow geometries. The jet fluid is injected through an opening perpendicular into the cross-stream. (a) the wall-issued case, and (b) the elevated JICF.

haviour. The least understood of these are the *jet shear layer vortices* which are the principle structures in the near field that define the mixing characteristics of the flow and the JICF penetration (Broadwell and Breidenthal, 1984; Cortelezzi and Karagozian, 2001; Marzouk and Ghoniem, 2007). These vortices are discussed at length in this thesis.

There has also been a shift in focus in recent years to using flow control to modify the JICF flow field. Fine control of the penetration, spread and mixing of JICFs would be highly beneficial for the performance and efficiency of many processes. JICF flow control research is an emerging area, but numerous advances have recently emerged (Megerian et al., 2006; M'Closkey et al., 2002; Johari et al., 1999). However, much remains unknown about the structure and control of JICFs. This thesis makes several contributions in these areas.

This thesis addresses structural changes that occur in a low momentum elevated JICF's jet shear layer vortices when it is forced by coaxial annular "blowing" from a synthetic jet. The work here is essentially an extension of Diep and Sigurdson (2002) who observed many previously undocumented phenomena in the elevated JICF. The three manuscripts presented in this thesis provide information about the fundamental natures of these phenomena.

1.1 JICF Parameters Considered

The flow field is primarily defined by the relative momenta of the jet and crossflow

$$R = \alpha^{\frac{1}{2}} \left(\frac{\rho_j W_j^2}{\rho_\infty U_\infty^2} \right)^{\frac{1}{2}} \tag{1.1}$$

written above as an effective jet-to-crossflow velocity ratio, R, where ρ_j and W_j are the density and spatially-averaged velocity of the jet, respectively, and ρ_∞ and U_∞ are the crossflow's density and velocity. In these studies, the jet and crossflow densities are equivalent. α is a momentum flux correction factor which is used here to account for the difference in momentum between an assumed top-hat velocity profile of the jet as it leaves the stack and the actual viscous velocity profile containing a boundary layer (Johnston and Wilson, 1997). The other parameters that are important to this study are, of course, the jet and crossflow Reynolds numbers Re_d and Re_∞.

The studies in this thesis relate to a low momentum elevated JICF with laminar pipe flow. We shall define the low momentum JICFs as having jet-to-crossflow velocity ratios $R \leq 1.5$, where the JICF structure and penetration are affected by strong pressure fields (Sherlock and Stalker, 1941; Keffer and Baines, 1963). Low momentum JICFs have received little attention in the literature, possibly due to the greater challenges involved in investigating their flow fields. Generally, research is carried out at higher velocity ratios around $R \approx 5$ where the jet momentum is much higher than the free stream momentum, so downwash and in pipe separation do not complicate the analysis (Overcamp and Ku, 1986). This may be the reason why many of the low momentum phenomena have not been documented despite many decades of JICF research.

1.2 Formation and Evolution of JICF Vortex Structures

Chapter 2 is the first manuscript entitled "Structural changes in synthetic jet forced elevated jet-in-crossflow." This chapter discusses structural changes in an elevated JICF that occur when it is forced by a synthetic jet coaxial to the jet flow. The experiment replicates phenomena observed by Diep and

Sigurdson (2001). New visualization techniques allow for a more detailed analysis of the flow field and provide new information related to the natures of the phenomena.

Studies into the structure and control of elevated JICFs are rare despite what is known from preliminary investigations, that the elevated JICF's jet shear layer vortices have a different structure and behaviour from its wall-issued counterpart (Andreopoulos, 1989; Huang and Lan, 2005). The elevated JICF and synthetic jet interaction produces unique arrangements of vortical structures which have a wide range of behaviors. The structural changes are a strong function of forcing amplitude. A detailed exploration is undertaken to characterize the low momentum forced elevated JICF at different velocity ratios and to track the formation and evolution of the vortices in the structures.

1.3 Relaminarization

Chapter 3 contains the second manuscript entitled "Suppression of jet shear layer instabilities in a low momentum elevated jet-in-crossflow." The elevated JICF's jet shear layer instabilities are completely suppressed and made steady in the near field when the JICF is forced with a low amplitude synthetic jet coaxial to the jet flow. The phenomenon is studied and the mechanism responsible for "relaminarization" of the flow is explained.

Most strategies proposed for JICF control involve full modulation of the jet flow by flow constriction or by acoustics. However, using direct pulsation of the jet stream in an elevated geometry may not be as effective due to the viscous losses that occur as the flow travels up the stack. Flow control in this thesis uses an alternative strategy developed by Diep (2001) whereby the elevated JICF's structure and penetration is modified by the synthesis of another fluid stream, a *synthetic jet* (Smith and Glezer, 1998), coaxial to the jet flow.

The ability to control mixing between the jet and cross-stream has the potential of improving efficiencies in may applications. Flow control strategies to enhance the JICF penetration, spread and apparent mixing of the two fluid streams are documented in the literature (Johari et al., 1999; M'Closkey et al., 2002; Eroglu and Breidenthal, 2001). However, more mixing is not always desirable, for example in film cooling applications (Haven and Kurosaka, 1996). The development of strategies for the suppression of mixing and JICF instabilities has received little attention. This study is one of the first investigations in this area.

1.4 Three-Dimensional JICF Large-Scale Structures

Chapter 4 is the third and final manuscript entitled "Digitization of jet-in-crossflow jet shear layer vortex structure via augmented reality." The three-dimensional large-scale vortex structure of the elevated JICF is obtained for the first time using a stereoscopic visualization data extraction system developed by Strand et al. (2007). Its spatial co-ordinates are extracted for proposal of a three-dimensional vortex tube model of the jet-shear layer vortex structure.

In JICFs, and other turbulent flows, there are large-scale structures composed of vortices whose behaviour dictates the gross characteristics of the flow field (Roshko, 1976). Knowledge of these structures is required to formulate effective strategies for flow control. The unforced JICF's flow behaviour is a result of the formation and evolution of systems of vortices that coexist in the turbulent plume. The structures are complex and highly three-dimensional. There has been substantial progress in understanding the nature of the vortex structures in wall-issued JICFs (Fric and Roshko, 1994; Kelso et al., 1996; Cortelezzi and Karagozian, 2001), however must less is known about the elevated case. Studies relating to the elevated JICF's jet shear layer vortex structures are particularly rare. Recently, Huang and Lan (2005) made some progress in understanding the evolution of the jet shear layer vortices in the low momentum elevated JICF, however their use of a laser sheet through the symmetry plane limited their ability to make conclusions about the complete jet shear layer vortex structure. The aim of this chapter is to extend our understanding of the jet shear layer by determining its three-dimensional vortex structure.

Finally, Chaper 5 presents a summary of the conclusions and provides recommendations for future work.

BIBLIOGRAPHY

Andreopoulos, J. (1989). Wind tunnel experiments on cooling tower plumes. I. in uniform crossflow. *Transactions of the ASME. Journal of Heat Transfer*, 111(4):941–8.

Andreopoulos, J. and Rodi, W. (1984). Experimental investigation of jets in a crossflow. *Journal of Fluid Mechanics*, 138:93–127.

Briggs, G. (1975). *Plume rise predictions, Lectures on Air Pollution and Environmental Impact Analyses*, pages 59–111. American Meteorological Society.

Broadwell, J. E. and Breidenthal, R. E. (1984). Structure and mixing of a transverse jet in incompressible flow. *Journal of Fluid Mechanics*, 148:405–12.

Cortelezzi, L. and Karagozian, A. R. (2001). On the formation of the counter-rotating vortex pair in transverse jets. *Journal of Fluid Mechanics*, 446:347–73.

Diep, J. (2001). Flow Control Reduction of Smokestack Downwash. Master's thesis, Department of Mechanical Engineering, University of Alberta.

Diep, J. and Sigurdson, L. (2001). Cross-jet influenced by a concentric synthetic jet. *Physics of Fluids*, 13(9):S16.

Diep, J. and Sigurdson, L. (2002). *Low velocity ratio transverse jets influenced by concentric synthetic jets.* Manipulation and Control of Jets in Crossflow, CISM Courses and Lectures No. 439. International Centre for Mechanical Sciences.

Eiff, O. S. and Keffer, J. F. (1997). On the structures in the near-wake region of an elevated turbulent jet in a crossflow. *Journal of Fluid Mechanics*, 333:161–95.

Eroglu, A. and Breidenthal, R. E. (2001). Structure, penetration, and mixing of pulsed jets in crossflow. *AIAA Journal*, 39(3):417–23.

Fric, T. F. and Roshko, A. (1994). Vortical structure in the wake of a transverse jet. *Journal of Fluid Mechanics*, 279:1–47.

Hasslebrink, E. F. and Mungal, M. G. (2001). Transverse jets and jet flames. Part 1. Scaling laws for strong transverse jets. *Journal of Fluid Mechanics*, 443:1–25.

Haven, J. P. and Kurosaka, M. (1996). Improved Jet Coverage Through Vortex Cancellation. *AIAA Journal*, 34(11):2443–4.

Huang, R. F. and Lan, J. (2005). Characteristic modes and evolution processes of shear-layer vortices in an elevated transverse jet. *Physics of Fluids*, 17(3):034103.

Johari, H., Pacheco-Tougas, M., and Hermanson, J. C. (1999). Penetration and mixing of fully modulated turbulent jets in crossflow. *AIAA Journal*, 37(7):842–50.

Johnson, M. R. and Kostiuk, L. W. (2000). Efficiencies of low-momentum jet diffusion flames in crosswinds. *Combustion and Flame*, 123(1):189–200.

Johnston, C. R. and Wilson, D. J. (1997). A vortex pair model for plume downwash into stack wakes. *Atmospheric Environment*, 31(1):13–20.

Keffer, J. F. and Baines, W. D. (1963). The round turbulent jet in a crosswind. *Journal of Fluid Mechanics*, 15(4):481–96.

Kelso, R. M., Lim, T. T., and Perry, A. E. (1996). An experimental study of round jets in cross-flow. *Journal of Fluid Mechanics*, 306:111–44.

Lim, T. T., New, T. H., and Luo, S. C. (2001). On the development of large-scale structures of a jet normal to a cross flow. *Physics of Fluids*, 13(3):770–75.

Margason, R. J. (1993). Fifty years of jet in cross flow research. Technical Report AGARD-CP-534.

Marzouk, Y. M. and Ghoniem, A. F. (2007). Vorticity structure and evolution in a transverse jet. *Journal of Fluid Mechanics*, 575:267–305.

M'Closkey, R. T., King, J. M., Cortelezzi, L., and Karagozian, A. R. (2002). The actively controlled jet in crossflow. *Journal of Fluid Mechanics*, 452:325–35.

Megerian, S., Davitian, J., de B. Alves, L. S., and Karagozian, A. R. (2006). Transverse jet shear layer instabilities - Part I: Experimental studies. to appear in the *Journal of Fluid Mechanics.*

Moussa, Z. M., Trischka, J. W., and Eskinazi, S. (1977). The near field in the mixing of a round jet with a cross-stream. *Journal of Fluid Mechanics*, 80(1):49–80.

Overcamp, T. J. and Ku, T. (1986). Effect of a virtual origin correction on entrainment coefficients as determined from observations of plume rise. *Atmospheric Environment*, 20(2):293–300.

Pratte, B. D. and Baines, W. D. (1967). Profiles of round turbulent jet in cross flow. *American Society of Civil Engineers Proceedings, Journal of the Hydraulics Division*, 92:53–64.

Roshko, A. (1976). Structure of turbulent shear flows: a new look. *AIAA Journal*, 14(10):1349–57.

Sherlock, R. H. and Stalker, E. A. (1941). A study of flow phenomena in the wake of smokestacks. *Engineering Research Bulletin No. 29, University of Michigan, Ann Arbor, MI. 49 pp.*

Smith, B. L. and Glezer, A. (1998). The formation and evolution of synthetic jets. *Physics of Fluids*, 10(9):2281–97.

Smith, S. H. and Mungal, M. G. (1998). Mixing, structure and scaling of the jet in crossflow. *Journal of Fluid Mechanics*, 357:83–122.

Strand, C., Watson, G., Nault, J., Tucker, R., Ausford, C., and Sigurdson, L. (2007). An Augmented Reality 3-D digitization system for stereoscopic flow visualization images. In preparation for submission to the *Journal of Visualization*.

Su, L. K. and Mungal, M. G. (2004). Simultaneous measurements of scalar and velocity field evolution in turbulent crossflowing jets. *Journal of Fluid Mechanics*, 513:1–45.

CHAPTER 2

FORMATION AND EVOLUTION OF LOW MOMENTUM ELEVATED JET-IN-CROSSFLOW VORTICES

2.1 Introduction

The jet-in-crossflow's (JICF's) response to forcing is quite complex. Results from numerous studies (Johari et al., 1999; M'Closkey et al., 2002; Narayanan et al., 2003; Megerian et al., 2006), including this one, hint to variability in the JICF's response to external conditions. Its response depends on the JICF's flow geometry and on the jet-to-crossflow velocity ratio written here in its simple form $R = W_j/U_\infty$, where W_j is the spatially averaged jet velocity and U_∞ is the crossflow velocity . In this study, flow visualization experiments were carried out on the low momentum elevated JICF to identify and characterize changes in the jet shear layer vortex structure when the JICF is forced by an annular synthetic jet coaxial to the jet flow.

This experiment is a follow-up of the work of Diep and Sigurdson (2001) whose results were the first of its kind for this geometry and forcing technique. Diep and Sigurdson (2001) presented visualizations of the structural changes in the forced JICF. Through key questions remained relating to the role of the synthetic jet's vorticity in the structural changes. The results presented here give an in depth analysis of the phenomena and provide new information related to the changes in the vortices' arrangements.

As will be seen in the results, the low momentum elevated JICF's forced behaviour is best classified by splitting the JICF operating parameters into two regimes based on the JICF's initial unforced velocity ratio. A "low momentum" elevated JICF has been defined as one having a velocity ratio of $R < 1.5$ where downwash has a noticeable influence on the jet penetration (Sherlock and Stalker, 1941). In this R range, the results will be presented in two regimes which are on opposite sides of $R = 1.13$, where there are marked changes in the unforced jet shear layer's behaviour. We shall label the range $R < 1.13$ as the "low velocity ratio regime" and $1.13 < R \leq 1.5$ as the "high velocity ratio regime."

2.2 Background

2.2.1 Coherent Structures

Four types of coherent structures have been identified in the near field of the unforced elevated JICF. The structures are briefly commented on here. (i) Kármán vortices are shed from the stack boundary layer into the stack-wake. The wake's effect on the elevated JICF mean flow field has been the subject of numerous studies, especially in the area of plume dispersion (Snyder and Lawson, 1991; Overcamp, 2001; Johnston and Wilson, 1997). (ii) Jet shear layer vortices are coherent structures which are a distinguishable feature in the near field (Huang and Lan, 2005). The jet shear layer vortices will be discussed in great detail in this chapter. (iii) Some vorticity in the jet shear layer is also thought to be "shed" into the jet-wake in the form of "jet-wake vorticity." The jet-wake structure is locked into the Kármán shedding frequency, however the structures have only been investigated for $R > 1.5$ (Eiff and Keffer, 1997). Jet-wake vortices have also been observed in a wall-issued JICF by Fric and Roshko (1994). They argue that the source of the vorticity is not from the jet, but is from separation events in the wall boundary layer on the lee side of the JICF. However, the wall boundary layer is not a factor in elevated JICF experiments. (iv) Finally, a counter rotating vortex pair (CVP) whose vorticity points in the stream-wise direction begins to form in the near field and is the dominant feature in the far field. The CVP is a time averaged feature of the flow and it is thought to be formed by jet shear layer vorticity (Cortelezzi and Karagozian, 2001). It is also the dominant source of mixing between the jet and crossflow in the far field. This study focuses on the structural changes that occur in the jet shear layer vortices when the JICF is forced via open loop control.

Research related to the structure and control of the elevated JICF jet shear layer vortices is rare. Andreopoulos (1989) observed and sketched three types of vortex structures that occur within an unforced jet shear layer. The structures were termed mushroom-type, wake-like and jet-like vortices. The occurrences of the structures were highly dependent on R. Diep and Sigurdson (2001) presented a series of images showing the response of a low momentum, forced and elevated JICF's jet shear layer vortices to an annular synthetic jet and noted some vortex structural change as a function of forcing amplitude. Follow-up work on these observations is the subject of this chapter. Recently, Huang and Lan (2005) presented a more in depth survey of the evolution process of unforced jet shear layer vortices in low momentum elevated JICFs. Their survey revealed five characteristic flow structures (three of which were the structures observed by Andreopoulos (1989)) whose behavior was highly depended on the R. Some of the structural changes they found have similarities to Diep and Sigurdson (2001). A comparison between the forced case (Diep and Sigurdson, 2001) and the unforced case (Huang and Lan, 2005) is undertaken in Section 2.4.2.

2.2.2 The Forced Jet-in-Crossflow

The JICF's response to forcing is well documented for the wall-issued case. However, the method of forcing used in the wall-issued cases is quite different than the technique used here. For the wall-issued case, the JICF has been forced by perturbing the entire jet flow either by mechanical restriction of the jet fluid inside the pipe (Johari et al., 1999; Eroglu and Breidenthal, 2001; Johari, 2006) or by acoustic excitation (M'Closkey et al., 2002; Shapiro et al., 2006). The studies report increased jet penertration and spread at specific conditions of excitation. At low velocity ratios, $2.6 \leq R \leq 4$, large amplitude sinusoidal excitation often does not produce significant JICF response, however the effect of forcing is more pronounced with square wave excitation at low duty cycles. Forcing under these conditions leads to a bifurcated structure with deeply penetrating "puffs" of vorticity.

The technique used here uses a unique method of forcing via a synthetic jet at the stack tip rather than pulsation of the entire jet flow. However, experiments by Smith and Glezer (2002) have looked at the behavior of two dimensional conventional jets in response to the application of a single synthetic jet on both sides.

2.3 Method

2.3.1 The Apparatus[1]

The apparatus consisted of a 25.4 mm diameter, D, "stack" inserted half way into a 30.5 cm by 30.5 cm wind tunnel test section[2]. The jet flow issued perpendicularly into the cross-stream through a central tube aligned with the stack centre which had an inside diameter, d, of 19.12 mm. Hot-wire measurements of the jet flow in crossflow indicated a that the jet flow inside the pipe was laminar with a fully developed parabolic profile for the experiments reported here.

Surrounding the central tube was an annulus with an inner width, h, of 1.64 mm through which a sinusoidal velocity fluctuation was introduced. The fluctuation was generated by a shaker table/piston assembly connected to a sealed chamber at the the bottom of the annulus. The cyclic action of sucking in ambient fluid then ejecting vorticity created a zero-net mass flux synthetic jet which was coaxial to the jet flow.

The synthetic jet frequency, f_{sj}, was measured with a pressure transducer tracking pressure fluctuations in the sealed chamber. Unforced JICF operating parameters and the synthetic jet forcing amplitude were characterized by low speed hot-wire measurements above the annulus exit[3].

2.3.2 Flow Visualization

Two methods of flow visualization were used to selectively capture the evolution of vorticity in the jet shear layer vortex structure. First, the jet was seeded with neutrally buoyant glycol fog vapour to track vorticity originating in the inner pipe boundary layer. Then, the crossflow was seeded with a smoke-wire placed upstream of the JICF to track vorticity generated on the outside of the stack. Photographs were illuminated by a collimated light sheet provided by a General Radio Type 1540 Strobalume. The light sheet was approximately one and a half stack diameters wide, measured along the stack exit plane.

The diameter of the smoke-wire is rather small (0.005"), however the wire's wake could have been a problem if it had been placed incorrectly.

---

[1] A full description of the apparatus is in Section 3.2. The development of the apparatus is discussed in detail in Diep (2001).

[2] A sketch of the apparatus is in Figure 3.1.

[3] A description of the hot-wire calibration method is in Appendix A.

Vorticity shed from the smoke-wire can pile up inside the stagnation region on the upstream side of the JICF distorting the jet shear layer vortex structure. To get around this problem, the smoke-wire must be placed either close to the JICF in the lower stagnation velocities where the smoke-wire's wake would be weakened, or far from the JICF so that the wake has time to diffuse. It was unfeasible to place the smoke-wire close to the stack due to the changing position of the stagnation region along the jet trajectory. Instead, the smoke-wire was placed three stack diameters upstream of the stack. At this position, the smoke wire was observed to have a negligible effect on the jet shear layer vortex structure.

Smoke injected directly into vorticity bearing fluid, into the jet or the outer stack boundary layer, will mark the progress of the vorticity and the roll-up of vortices. However, the tracer can also reveal the formation of other vortices if the fluid that it marks is drawn into the vortices' cores. It should be noted that smoke diffuses at a slower rate than vorticity, therefore the smoke's reliability as a marker of the vorticity deteriorates over time.

2.3.3 Measurement of JICF Operating Points

A 1.25 mm long, 5 μm diameter, single-component hot-wire (Dantec Dynamics, platinum-plated tungsten, type 55P1) in constant temperature mode was used to obtain low velocity measurements of the flow field.

The JICF parameters U_∞ and W_j were based on nominal jet and crossflow profiles. They were the crossflow conditions with no jet flow and jet conditions with no crossflow, respectively. For all cases reported here the jet flow at the stack exit is was fully developed parabolic profile.

It must be emphasized that the jet-to-crossflow velocity ratio $R = W_j/U_\infty$ is a simplified form of a momentum ratio shown in expanded form below

$$R = \alpha^{\frac{1}{2}} \left(\frac{\rho_j}{\rho_\infty}\right)^{\frac{1}{2}} \left(\frac{W_j^2}{U_\infty^2}\right)^{\frac{1}{2}} \tag{2.1}$$

where α is a correction factor to account for the difference in momentum between an assumed top-hat velocity profile in the momentum flux equation and the actual viscous velocity profile of the jet flow. $\alpha = 4/3$ for a fully developed, parabolic profile. The JICF is neutrally buoyant, therefore the density ratio ρ_j/ρ_∞ is unity.

The hot-wire was also used to characterize the synthetic jet flow. Hot-wire measurements determined the peak centreline ejection velocity $w_{sj,max}$ at the exit plane $z/h = 0$ and the average synthetic jet velocity W_{sj} at $z/h = 2$. $w_{sj,max}$ was used to characterize synthetic jet forcing amplitude $w_{sj,max}/W_j$. The measurement point for W_{sj} was chosen as a compromise of not being too close to the annulus exit where there is flow reversal and too far away where the synthetic jet has less of an effect on the jet flow.

The synthetic jet adds momentum to the total JICF profile. It was useful to approximately account for the added momentum in a new formulation of the velocity ratio named the "momentum velocity ratio", M_M, which was derived by Diep and Sigurdson (2002). Like R, M_M is also a ratio of momentum fluxes

$$M_M = \left(\frac{F_t}{\rho_j U_\infty^2 A_m} \right)^{\frac{1}{2}} \tag{2.2}$$

where F_t is the total momentum flux applied over the whole stack area ($F_t = F_j + F_{sj}$) and A_m is the "momentum-weighted area." A_m is an empirical weighting based on Diep and Sigurdson's experimental data which showed that the synthetic jet momentum dominates the elevated JICF at high velocity ratios. Both terms are shown in expanded form below

$$F_t = \alpha \rho_j A_j W_j^2 + \frac{\rho_\infty + \rho_j}{2} A_{sj} W_{sj}^2 \tag{2.3}$$

$$A_m = \frac{F_j A_j + F_{sj} A_{sj}}{F_t} \tag{2.4}$$

where A_j and A_{sj} are the initial jet and synthetic jet annulus areas, respectively. The synthetic jet momentum flux was estimated using the average centerline velocity of the synthetic jet, W_{sj}, and the exit area of the annular slit assuming a top-hat profile. F_{sj} was not calculated by measuring a time averaged velocity profile across the synthetic jet. Although the calculation is not precisely the momentum flux, the value F_{sj} is expected to be proportional to the true momentum flux of the synthetic jet. It should be noted that for the case of no forcing ($F_{sj} = 0$), Equation 3.2 simplifies to yield $M_M = R$.

2.4 Results and Discussion

2.4.1 The Low Velocity Ratio Regime

We shall start the discussion in the low velocity ratio regime where Diep and Sigurdson (2001) presented their results. This experiment is a follow-up investigation, therefore the flow parameters for this experiment were chosen to be approximately identical to their case. Experiments were performed on the elevated JICF at a crossflow Reynolds number of $\text{Re}_\infty = 1270$ at an initial, unforced velocity ratio of $R = 0.69$. Figure 2.1(a) shows side view photographs of the initial, unforced JICF jet shear layer vortex structure using the two alternative visualization techniques: jet-seeded smoke visualization in (i), and crossflow-seeded in (ii). Although the images were not taken simultaneously, care was taken to ensure that all photographic pairs in the experiment were taken at the same operating parameters. Photographs for the image pairs were also chosen so that the images captured the JICF at approximately the same stage in the vortex structures' evolution. The methodology to take the photographs was the same for all image pairs presented in this section. First, the jet-seeded photographs were taken, then without the controls being changed crossflow-seeded photographs were taken approximately five minutes after – just enough time for the smoke in the jet to clear.

Comparisons will be made between the results presented in this section and those in Huang and Lan (2005). They presented an extensive survey of an unforced elevated JICF jet shear layer vortices' evolution over a range of velocity ratios $R < 1.29$. However, in this experiment the velocity ratio of the forced JICF was progressively increased by the addition of momentum from a synthetic jet. The crossflow Reynolds number of $\text{Re}_\infty = 2051$ in Huang and Lan (2005) was approximately twice the crossflow Reynolds number used in this experiment. Parabolic velocity profiles at the stack exit were measured for both experiments. It should also be noted that the velocity ratios of Huang and Lan (2005) reported here have been corrected to account for their parabolic velocity profile. In Huang and Lan (2005), the elevated JICF was observed to pass through two regimes. First, for $R < 1.16$, the unforced jet shear layer vortex structure was highly dependent on velocity ratio and vortices were consistently shed into the crossflow at a characteristic frequency. The Strouhal number of the jet shear layer vortices decreased exponentially with increased velocity ratio and approached a constant of about 0.61 as R approached one. In their experiment, the Strouhal number was defined as $\text{St}_d = f_n d/W_j$ where f_n was the frequency of the vortices shed into the jet shear layer. We shall use the same notation here. Secondly, in a jet dominated regime where $R > 1.16$, the jet shear layer vortices' appearance was intermittent. Experiments using the apparatus in present study with no forcing have reproduced the same characteristic vortex structures observed by Huang and Lan (2005). This is not surprising since the dimensions of the JICF apparatus in this study and Huang and Lan (2005) are similar.

Figure 2.1(a) shows photographs of the initial unforced JICF. The naturally occurring jet shear layer vortex structure is visible in the jet-seeded photograph. As the vorticity evolves along the jet shear layer, it rolls up into what will be referred to as a "tri pole." The tri-pole consists of a mushroom structure containing a counter-rotating pair of vortices (a dipole) on the upstream side of the JICF and a vortex of negative vorticity[4] on the downstream side of the JICF. The vortex structure's arrangement resembles Huang and Lan's "backward-rolling" vortices, which they observed over a range of velocity ratios, $0.45 < R < 0.66$. The velocity ratio in this experiment is in the upper end of that range. Under these conditions, the natural roll up of the vortices in the jet shear layer are regular and periodic over a wide Reynolds number range (Huang and Lan, 2005). The natural roll up frequency of the vortices in the jet shear vortex structure was measured with a stroboscope to be $\mathrm{St}_d = 0.82$, which is 17% larger than the measurements of Huang and Lan (2005).

The crossflow-seeded photograph in Figure 2.1(a) provides clues to the origin of the vorticity in the unforced jet shear layer. Streaklines clearly show the roll up of negative vorticity at the leading edge of the stack exit. Since the crossflow fluid is irrotational, it is surmised that the negative vorticity in the counter-rotating mushrooms are formed when cross-stream fluid travels up the outer solid wall of the stack and separates at the stack leading edge. The photograph also shows that the negative "outer stack" vorticity periodically moves away from the stack exit and travels along the jet shear layer at the natural roll up frequency of the jet shear layer.

A striking change in the jet shear layer vortex structure occurs when the JICF is forced with a 60 Hz, low amplitude synthetic jet. Eventually, by increasing the forcing amplitude, the JICF can be made steady and completely relaminarized in the near field. The near field is defined as the area where the JICF's trajectory still has a non-negligible vertical component, which is approximately three to four jet diameters in this case. Figure 2.1(b) shows that the forced JICF lacks the complicated vortex structure of the unforced case, although small ridges coupled to the forcing frequency are still apparent on the upstream side of the jet shear layer. Relaminarization is a suppression of the naturally occurring jet shear layer instability in the unforced JICF[5]. In these photographs, the relaminarized JICF jet shear layer is forced by fluctuating velocity magnitudes that were approximately 60% of the mean jet velocity, measured along the synthetic jet centreline at $z/h = 0$.

---

[4] into of the page by the right-hand-rule through the centre plane of the JICF, clockwise.

It is possible to trace the flow on the upstream side of the jet shear layer using cross-seeded flow visualization in Figure 2.1(b). Close to the stack exit, clockwise-rotating vortices are visible along the upstream side of the jet shear layer with a frequency that is equal to the synthetic jet forcing frequency. At the stack's leading edge, the streaklines hint to an inward flow into the synthetic jet annulus. This image was probably taken during the suction phase when ambient and jet fluid is sucked into the synthetic jet orifice. The fluid is then ejected into the flow at a later time in the synthetic jet actuator's cycle. The sign of vorticity which dominates in the ejected vortices is the same as the outer stack vorticity. Perhaps the net vorticity which leaks into the flow during the ejection stroke is not visible because the vortices in the synthetic jet are too weak to entrain marked fluid into their cores. However, there is definitely a measurable increase in velocity over the annulus due to what we believe is the addition of synthetic jet momentum into the flow.

One must be careful in drawing conclusions from the streaklines since the unsteady structures' appearance is an integration of their motions (Cimbala et al., 1988). However, the well defined smoke structures in Figure 2.1(b)(ii) that form close to the annulus become stretched and flattened as they evolve along the jet shear layer. The fact that the definition of the structures and their wavelengths diminish suggests that when the vortices break down, the flow induced by the synthetic jet stays laminar as its convects along the jet shear layer.

An instability grows out of the relaminarized JICF with an increase in forcing amplitude. In Figure 2.1(c), there are structures on the upstream side of the jet shear layer resembling mushroom vortices which generally point upstream. "Pointing" is a term first used by Diep and Sigurdson (2002) to refer to the direction that the pairs would self-propagate, which is connected to the impulse of the pair. Although all the mushroom vortices generally point upstream, their pointing direction changes as they evolve. Initially, the pointing of the vortices closest to the stack exit are upward-biased. As they convect around the bend in the jet, their pointing rotates in a counter clockwise direction from an upward-biased direction to a downward-biased direction.

---

[5] The mechanism behind the phenomenon is described in detail in Chapter 3.

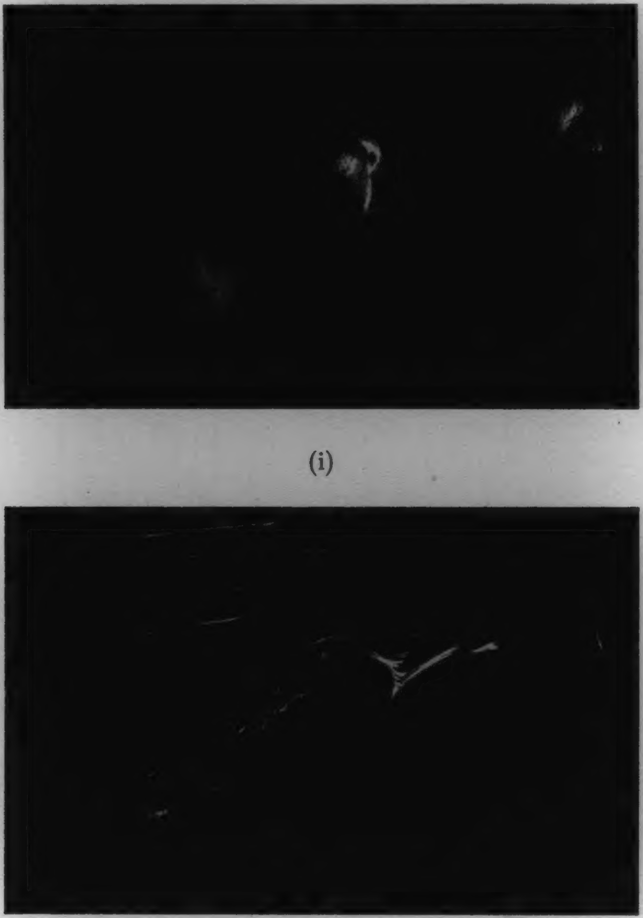

(i)

(ii)

Figure 2.1: (a) Change in structure of a low momentum JICF with laminar pipe flow with a 60 Hz synthetic jet, with increasing synthetic jet amplitude. These are reference photographs of the JICF with no forcing. Unforced JICF parameters are $\mathrm{Re}_\infty = 1270$ and $\mathrm{Re}_d = 570$ which gives the velocity ratio $R = M_m = 0.69$. The jet and crossflow velocities are constant throughout the sequence. All jet Reynolds numbers are back calculated from M_M. Paired photographs show the JICF with the same operating parameters, but are visualized with jet-seeded and crossflow-seeded flow in the top and bottom photographs, respectively.

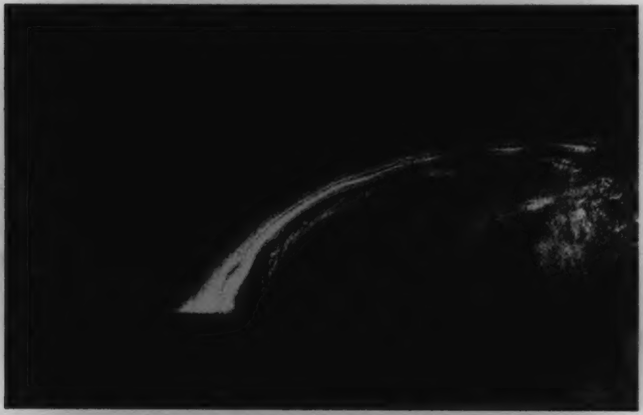

(i)

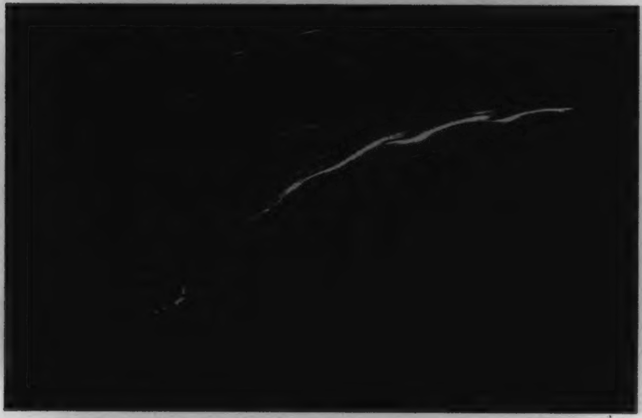

(ii)

Figure 2.1: (b) Change in structure of low momentum JICF under synthetic jet forcing *cont'd*. JICF relaminarises, $W_{sj} \approx 0.3$ m/s, $\mathrm{Re}_d \approx 660$, $M_M \approx 0.77$.

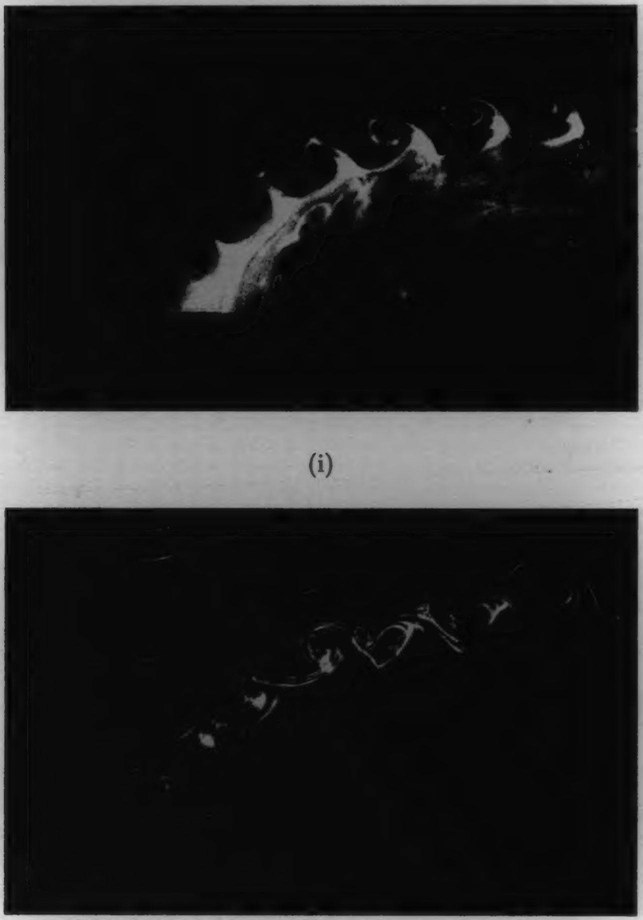

(i)

(ii)

Figure 2.1: (c) Change in structure of low momentum JICF under synthetic jet forcing *cont'd.* Upstream-pointing mushroom vortices, $W_{sj} \approx 0.9$ m/s, $\mathrm{Re}_d \approx 1130$, $M_M \approx 1.26$.

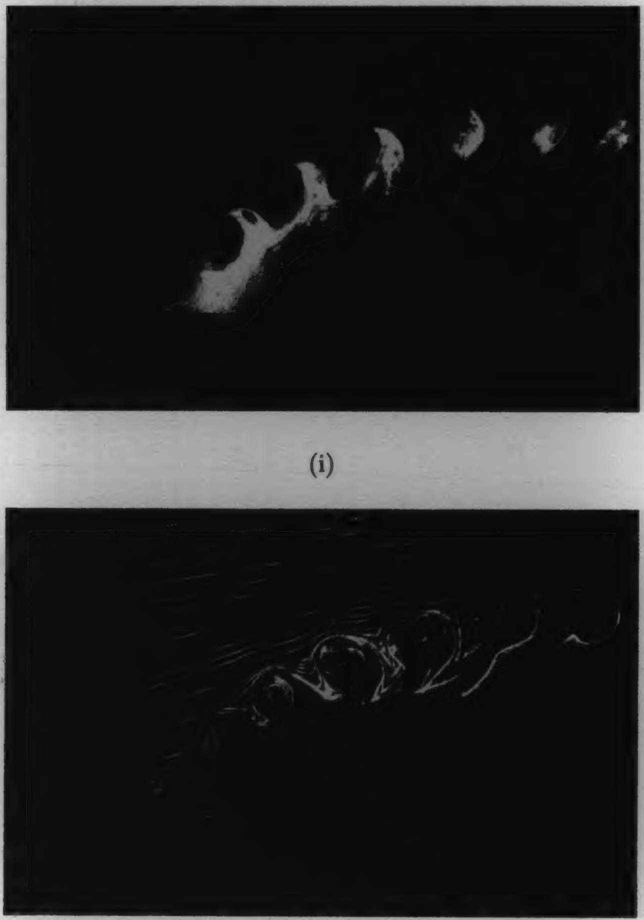

(i)

(ii)

Figure 2.1: (d) Change in structure of low momentum JICF under synthetic jet forcing *cont'd.* Downstream-pointing mushroom vortices, $W_{sj} \approx 0.9$ m/s, $\mathrm{Re}_d \approx 1130$, $M_M \approx 1.26$.

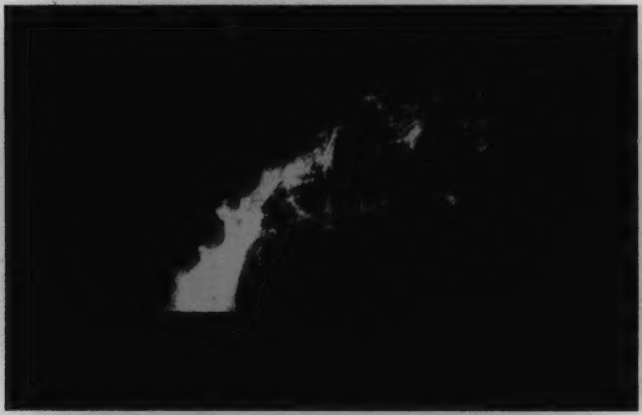

(i)

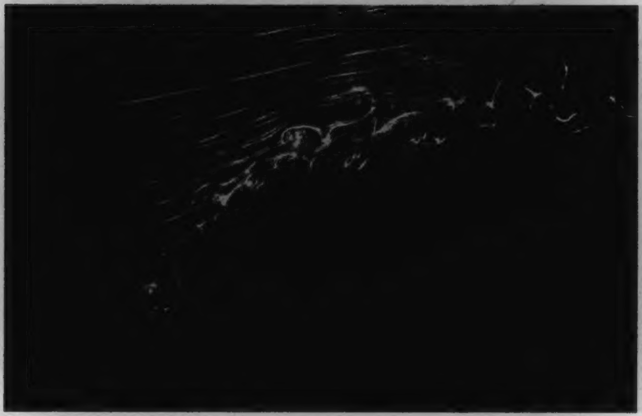

(ii)

Figure 2.1: (e) Change in structure of low momentum JICF under synthetic jet forcing *cont'd*. JICF lifting off and more turbulent, $W_{sj} = 1.2$ m/s, $\mathrm{Re}_d \approx 1500$, $M_M \approx 1.6$.

From now on, this arrangement of mushroom vortices will be termed the "upstream-pointing vortex structure." Visually studying the smoke intensity suggests that as the mushroom vortices evolve downstream, the size of the smoke region in the positive vorticity within the structure seems to grow with downstream distance. In any case, Diep (2001) observed that the smoke intensity in these structures is small, indicating not a lot of jet fluid entered the structures. However, mixing by entrainment of the cross-stream into the jet flow appears to have increased from the relaminarized case.

The crossflow-seeded photograph gives an alternative view of the jet-crossflow entrainment process. The photograph suggests that the mushroom vortices form during the ejection stroke from the synthetic jet annulus. It is not as clearly seen in the jet-seeded photograph, which suggests that the vortex pairs leaving the annulus are initially composed mostly of crossflow fluid. The vortex pairs in the synthetic jet are presumably strengthened due to the increased forcing amplitude, and consequently both signs of vorticity are visible in the mushroom vortices. The crossflow-seeded photograph shows that, initially, the relative smoke intensities of the vortices in the mushroom structure are different, with the positively signed vorticity having a higher concentration of white smoke in it. This is likely due to the pair's initial orientation and its tendency to entrain fluid from its surroundings. Due to the pairs' initial upwards pointing direction, the positive side (left) entrains the white smoke in the cross-stream getting whiter, while the negative (right) side entrains the un-seeded jet fluid getting blacker. As the pairs become the mushroom vortices in the upstream-pointing vortex structure, their change in orientation with respect to the two fluid streams changes their entrainment characteristics. Overtime the white, smoke-filled positive vortex core is replaced with a "black void" of jet fluid.

With a small increase in forcing amplitude, there is an abrupt transition in the vortex structures' arrangement to that shown in Figure 2.1(d). Figure 2.1(d) shows that, at this forcing amplitude, the mushroom vortices' pointing direction initially point upstream when close to the jet exit, but then rotate clockwise to point downstream with an upward-bias direction as they evolve around the bend in the JICF. Overall, these mushroom vortices have more upward momentum than the upstream-pointing vortex structure which occurred before the pointing transition. This could be related to the additional impulse of the vortex pairs due to a higher forcing amplitude. From now on, this vortex arrangement will be termed the "downstream-pointing vortex structure." Again, the size of the smoke in positive vorticity within the downstream-pointing vortex structure grows with downstream distance. The structure also appears to contain more jet fluid than did the upstream-pointing vortex structure which is suggested by the brighter smoke contained in the vortices.

A transition in the vortex structure similar to the Diep and Sigurdson (2002) "pointing" transition was observed by Huang and Lan (2005) for an unforced elevated JICF. Huang and Lan reported two adjacent domains of the velocity ratio where mushroom vortices turned to point downstream when $0.45 < R < 0.67$, then turned to point upstream when $0.67 < R < 0.81$. They termed the vortex structures in these domains "backward-rolling" and "forward-rolling", respectively. Representative photographs of the structures observed in the unforced JICF are shown in Figure 2.2. The structures were photographed with the apparatus in this study. The backward-rolling vortex structure's behaviour (Figure 2.2a) is similar to the downstream-pointing vortex structure in the forced case. The flow visualizations of Huang and Lan (2005) showed that, although the mushroom vortices initially pointed upstream near the jet exit they rotated clockwise to point in a downstream direction as they evolved around the bend in the jet. The JICF in Huang and Lan (2005) and in our study were viewed from the same perspective, therefore, "clockwise" represents the same direction of rotation for both cases. The size of the positive vorticity region in this structure appeared to grow with downstream distance. However, the forward-rolling vortex structure (Figure 2.2b) consisted of mushroom vortices pointing upstream which initially had an upward-biased pointing direction, but then with advection downstream, rotated counter clockwise to a downward-biased direction. This behaviour was identical to our upstream-pointing vortex structure. However, the size of the negative vorticity region within the forward-rolling vortex structure seems to grow with downstream distance, which is contrary to what is observed in the upstream-vortex structure.

Another difference should be noted in the behaviour of the unforced and forced "pointing" transitions is displayed schematically in Figure 2.3. The figure shows a comparison between the transitions that occur in the unforced and forced JICF structures. The change in the prominent pointing direction of the vortex structure after transition is different. With increasing R, the unforced structures' direction changed from pointing upstream to pointing downstream. The pointing direction could certainly be explained kinematically if the unforced JICF vortex structure's behaviour is taken to be primarily two-dimensional in nature. It is expected that the stack vorticity in the

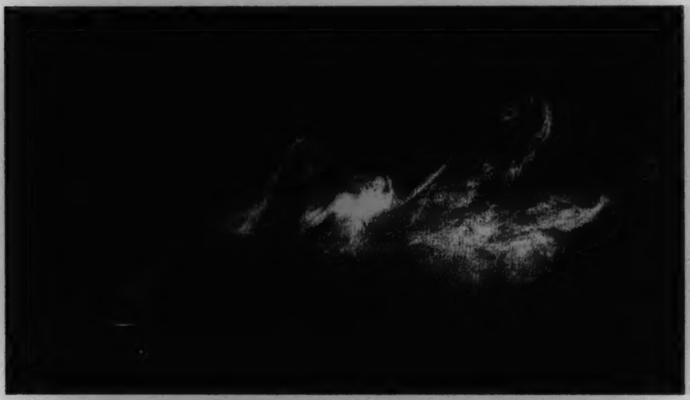

(a)

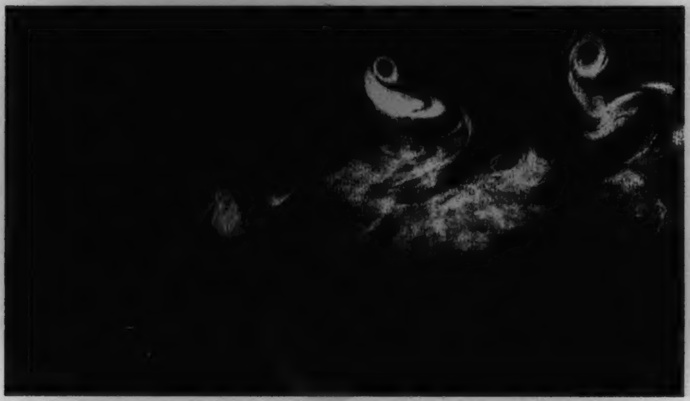

(b)

Figure 2.2: Change in structure of an unforced low momentum elevated JICF with increasing velocity ratio. The transition was first observed by Huang and Lan (2005). (a) backward-rolling vortices, (b) forward-rolling vortices.

mushroom structures relative to the vorticity in the jet column will become weaker as the velocity ratio decreases (Huang and Lan, 2005). This could shift the centre of vorticity in the mushroom structure to the right of the jet flow vortex thus creating the switch from a counter-clockwise to clockwise rotation. However, if this a correct interpretation, it does not hold for the forced case. In the forced case, pointing changed in the opposite direction as additional upward synthetic jet momentum was supplied to the jet flow.

As forcing amplitude is further increased, the vortices on the upper surface of the JICF continue to lift off in what appears to be a turbulent jet shear layer vortex structure, as suggested by Figure 2.1(e). The JICF is clearly higher than in the unforced case and shows an increased amount of spread in the vertical direction, which suggests significantly enhanced mixing between the jet and crossflow fluid streams. The crossflow-seeded photograph shows that the vortex pairs ejecting from the annulus are laminar, however the vortices break down and become turbulent after convecting a short distance along the jet shear layer. This evolution behaviour is also commonly seen in visualizations of fully formed synthetic jets in a quiescent fluid. Smith and Glezer (1998) propose that the strong adverse pressure gradients generated by the suction phase are responsible for the transition. It should be noted that the velocity fluctuations at the synthetic jet exit were 260% of the mean jet velocity, measured at $z/h = 0$. The forcing amplitudes are indeed high and as a result, it is thought that the adverse pressure gradient may have a similar effect on the jet shear layer.

2.4.2 The High Velocity Ratio Regime

This section presents additional observations for a forced elevated JICF in the high velocity radio regime, $R > 1.13$. An initial unforced velocity ratio of $R = 1.39$ was used. The crossflow velocity was matched with the case in Section 2.4.1 ($\mathrm{Re}_\infty = 1270$), therefore a higher jet constant velocity of $W_j = 0.9$ m/s ($\mathrm{Re}_d = 1147$) is used in this sequence of photographs, however the flow inside the pipe is still laminar.

The unforced jet shear layer is also unstable in this regime. Figure 2.4(a) shows a side view photograph of the unforced JICF at $R = 1.39$ and a crossflow Reynolds number $\mathrm{Re}_\infty = 1270$. The structure and behaviour of the unforced jet shear layer vortices are different from what is observed in the low R regime. A train of counter-clockwise rotating vortices appear on the upstream side of the JICF after the jet fluid has moved some distance along

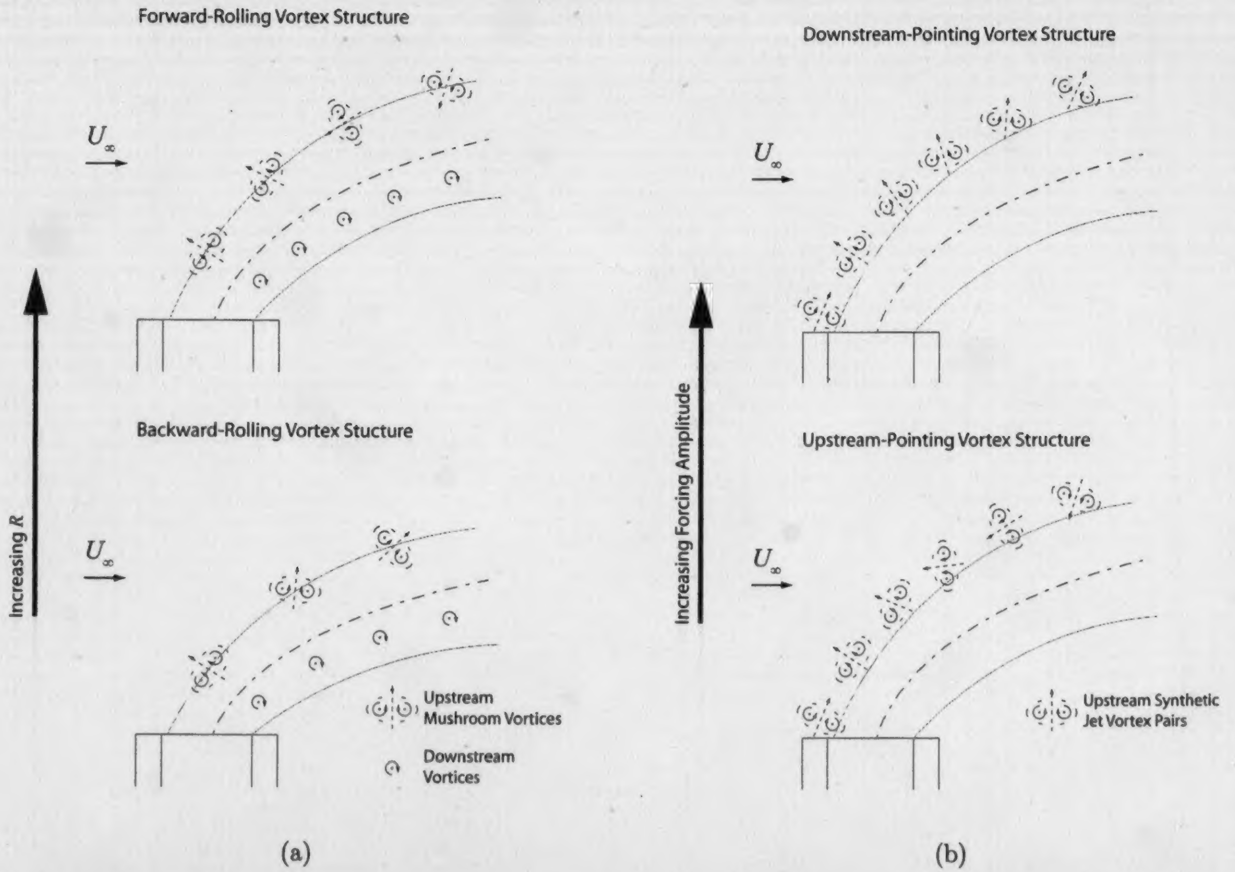
Forward-Rolling Vortex Structure
U_∞
Backward-Rolling Vortex Stucture
U_∞
Increasing R
Upstream Mushroom Vortices
Downstream Vortices
(a)
Downstream-Pointing Vortex Structure
U_∞
Upstream-Pointing Vortex Structure
U_∞
Increasing Forcing Amplitude
Upstream Synthetic Jet Vortex Pairs
(b)

Figure 2.3: Schematics of the pointing transitions that occur in the unforced and forced JICFs. The vortices shown are those that have been identified by smoke visualizations of the JICF plume. The pointing directions of the mushroom structures are shown with dashed arrows. (a) backward-rolling and forward-rolling vortex structures first documented by Huang and Lan (2005), (b) the Diep and Sigurdson (2001) pointing transition: upstream and downstream-pointing vortex structures.

the jet shear layer. The instability is intermittent, but when it occurs the frequency of roll up of the vortices appears to be consistent. It is difficult to capture the frequency of the vortices with a stroboscope or with hot-wire measurements due to the intermittency of the instability. Instead, time lapse photographs containing two instantaneous images of the vortex train 4 ms apart (consult Apps (2001) and Apps et al. (2003) for a description of the ICV apparatus and method) were taken to estimate the frequency of the vortex roll up. Measurements of the average wavelength and the convection velocity of the vortex train yields an approximate roll up frequency of $f_n \approx 68$ Hz ($\mathrm{St}_d \approx 1.86$ based on f_n). The frequency estimate is based on an average of four time lapse photographs of the flow structure. Huang and Lan (2005) have termed this flow structure "jet-type vortices," however the structure was also observed earlier by Andreopoulos (1989).

The jet shear layer instability occurs regularly with low amplitude, 60 Hz forcing ($\mathrm{St}_d = 1.64$ based on f_{sj}). In this case, the peak amplitude of the velocity fluctuation at the synthetic jet orifice, $z/h = 0$, is less than 10% of the mean jet velocity. The velocity, W_{sj}, of the resulting synthetic jet was too weak to be reliably measured by the hot-wire. Figure 2.4(b) shows the vortex structure which results from the forcing. The vortex train appears closer to the stack exit on the upstream side of the jet shear layer. Further downstream along the JICF trajectory, mushroom vortices of opposite signed vortices are discernible. The mushroom vortices appear to have more upward impulse than the vortices in Figure 2.4(a), which may have resulted from the additional momentum from the synthetic jet. Stroboscope measurements indicate that the vortex structure is locked into the 60 Hz forcing frequency. The instability seems to have a strong frequency preference. In this case, the chosen forcing frequency is close to the natural frequency of the unforced jet shear layer instability. Forcing at other frequencies further from the natural roll up frequency of the vortices did not visibly influence the natural jet shear layer instability, even at larger amplitudes.

When the forcing amplitude is increased, there is initially little change in the jet shear layer vortex structure. Figure 2.4(c) shows the resulting vortex structure when the peak amplitude of the fluctuating velocity at the synthetic jet exit plane is 140% of the mean jet velocity. For this case, $W_{sj} \approx 0.56$ m/s. In this photograph, perceptible growth of the jet shear layer instability occurs close to the stack exit. Pointing of the mushroom vortices is also more vertical which is consistent with the idea of increased synthetic jet momentum.

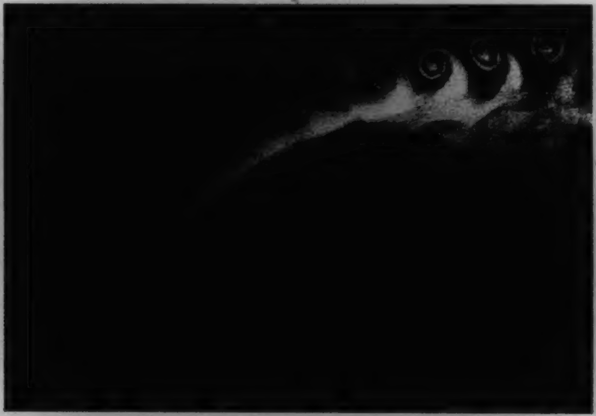

(a) The unforced JICF vortex structure. $R = M_M = 1.39$ and $\mathrm{Re}_d = 1147$. Vortex roll-up on the upstream side appears to be periodic, but the instability occurs intermittently.

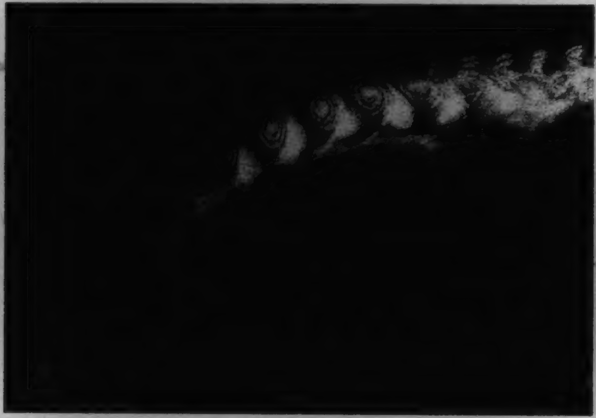

(b) Regular, periodic vortices appear on the upstream side of the jet shear layer with low amplitude synthetic jet forcing at frequency $f_{sj} = 60Hz$. W_{sj} is unknown but is small. $M_M \approx 1.39$, $\mathrm{Re}_d \approx 1147$.

Figure 2.4: Change in structure of a JICF at $R = 1.39$ with laminar pipe flow and a 60 Hz synthetic jet, with increasing synthetic jet amplitude. Crossflow Reynolds number is $\mathrm{Re}_\infty = 1270$ in all photographs. All jet Reynolds numbers are back calculated from M_M.

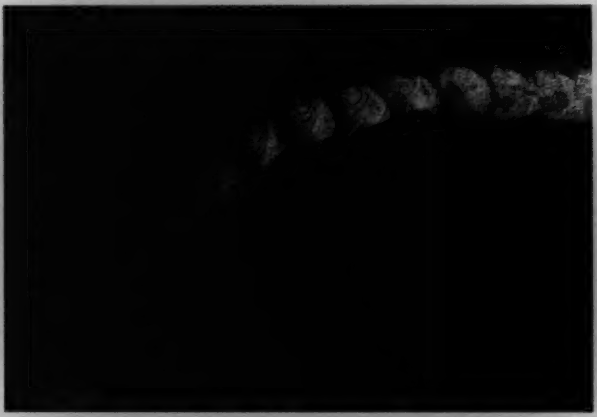

(c) The instability occurs closer to the jet shear layer at higher amplitudes. The upstream and downstream jet shear layer are unstable. Vortex pairs have more of an upward impulse. $W_{sj} \approx 0.56$ m/s, $M_M \approx 1.51$, $\mathrm{Re}_d \approx 1250$.

(d) JICF transitions to a fully turbulent structure in the near field when forced with a high amplitude synthetic jet. $W_{sj} \approx 1.24$ m/s, $M_M \approx 1.97$, $\mathrm{Re}_d \approx 1630$.

Figure 2.4: Change in structure of a JICF at $R = 1.39$, *cont'd.* Crossflow Reynolds number is $\mathrm{Re}_\infty = 1270$ in all photographs. All jet Reynolds numbers are back calculated from M_M.

With high amplitudes of forcing, in Figure 2.4(d), the JICF becomes too turbulent to discern the structure within it. The forcing amplitude is approximately 390% of the jet's mean velocity. $W_{sj} \approx 1.24$ m/s, which corresponds to the same level of forcing as the fully turbulent case in the low R regime (Figure 2.1e). Overall, the sequence of photographs demonstrates that in this regime, synthetic jet excitation induces an apparent enhancement in mixing. Little alteration in the jet penetration is achieved, however there is a visible change in the near field JICF trajectory which is probably due to increased entrainment and mixing of crossflow and jet momentum. It must be emphasized that the effect of synthetic jet in this regime is only to make the JICF more turbulent. Relaminarization of the initially unstable jet shear layer does not occur.

2.5 Summary and Conclusions

A wide variety of phenomena has been observed in the low momentum elevated JICF jet shear layer which are dependent on velocity ratio. In the low R range, $R < 1.13$, the vortex structures in the unforced jet shear layer appeared to have the same formation and evolution as the structures reported in Huang and Lan (2005). Crossflow-seeded photographs revealed the roll-up of a vortex above the leading edge of the stack whose properties depended on the stability of the jet shear layer. The vortex consisted mostly of vorticity from separated flow on the stack outer wall. When the jet shear layer was unstable, this vorticity was swept up into the jet shear layer and was a component of the tri pole jet shear layer vortex structure. It is puzzling that Huang and Lan (2005) neglect to mention the tri pole arrangement in their survey of the vortex arrangements. Close study of their images do in fact show the roll-up of jet vorticity on the lee side of the jet shear layer as well as a mushroom structure on the upstream side, however the vortices on the lee side are somewhat obstructed from view by smaller scales. The vortices on the lee side also had a wavelength that was noticeably larger than the mushroom vortices on the upstream side – the downstream vortices' wavelength approximately scales with the stack diameter. All three signs of vorticity must be accounted for to model the complete jet shear layer vortex structure.

Crossflow-seeded photographs were particularly helpful in strengthening our understanding of the Diep and Sigurdson (2001) phenomena that occur in the low velocity ratio regime. Seeding the crossflow allowed for the visualization of the initial evolution of the vortex pairs emerging from the synthetic jet annulus, which was previously not observed in the visualizations of Diep and Sigurdson (2001). The increasingly complex periodic vortex structure that emerged from the relaminarized jet at higher forcing amplitudes was made up of mushroom vortices from the synthetic jet annulus. The synthetic jet, therefore, had the effect of reorienting the vorticity in the forced jet shear layer.

Interesting similarities to the mode switching of the vortex structure found by Huang and Lan (2005) have been noted. Further work is necessary to fully understand the natures of these complex vortex arrangements. The abrupt "pointing" transition first noted by Diep and Sigurdson (2002), discussed in Section 2.4.1, coincides with an apparent increase in mixing of the jet flow with the crossflow. As the forcing becomes more powerful, the vortices that result from the forcing become stronger and entrain jet fluid more quickly. As the mushroom structures evolve downstream, the positively signed jet vorticity on the upstream side of the jet shear layer is entrained into the mushroom structures. This may be why the sign of the jet fluid appears to dominate in the mushroom structures as they evolve along the jet shear layer while the oppositely signed vorticity in the structures appears to diminish.

The elevated JICF's response to forcing in the high velocity ratio regime ($1.13 < R \leq 1.5$) has also been tested. The unforced jet shear layer instabilities behaved much differently from the regular, periodic instabilities that occurred at lower velocity ratios. Its global structure was not changed unless the jet was forced near to the frequency associated with the roll-up of the unforced jet shear layer vorticity. No relaminarization of the jet shear layer was observed in this regime. The synthetic jet's effect in this case was only to make the JICF more turbulent. In any case, relatively little change was attained in the vortex structure, jet penetration and spread though this method of forcing.

BIBLIOGRAPHY

Andreopoulos, J. (1989). Wind tunnel experiments on cooling tower plumes. I. in uniform crossflow. *Transactions of the ASME. Journal of Heat Transfer*, 111(4):941–8.

Apps, C. P. (2001). Study of synthetic fence jets using image correlation velocimetry. Master's thesis, Department of Mechanical Engineering, University of Alberta.

Apps, C. P., Chen, T., and Sigurdson, L. (2003). Image correlation velocimetry applied to discrete smoke-wire streaklines in turbulent pipe flow. *Experiments in Fluids*, 35:288–90.

Cimbala, J., Nagib, H., and Roshko, A. (1988). Large structure in the far wakes of two-dimensional bluff bodies. *Journal of Fluid Mechanics*, 190:265–98.

Cortelezzi, L. and Karagozian, A. R. (2001). On the formation of the counter-rotating vortex pair in transverse jets. *Journal of Fluid Mechanics*, 446:347–73.

Diep, J. (2001). Flow Control Reduction of Smokestack Downwash. Master's thesis, Department of Mechanical Engineering, University of Alberta.

Diep, J. and Sigurdson, L. (2001). Cross-jet influenced by a concentric synthetic jet. *Physics of Fluids*, 13(9):S16.

Diep, J. and Sigurdson, L. (2002). *Low velocity ratio transverse jets influenced by concentric synthetic jets.* Manipulation and Control of Jets in Crossflow, CISM Courses and Lectures No. 439. International Centre for Mechanical Sciences.

Eiff, O. S. and Keffer, J. F. (1997). On the structures in the near-wake region of an elevated turbulent jet in a crossflow. *Journal of Fluid Mechanics*, 333:161–95.

Eroglu, A. and Breidenthal, R. E. (2001). Structure, penetration, and mixing of pulsed jets in crossflow. *AIAA Journal*, 39(3):417–23.

Fric, T. F. and Roshko, A. (1994). Vortical structure in the wake of a transverse jet. *Journal of Fluid Mechanics*, 279:1–47.

Huang, R. F. and Lan, J. (2005). Characteristic modes and evolution processes of shear-layer vortices in an elevated transverse jet. *Physics of Fluids*, 17(3):034103.

Johari, H. (2006). Scaling of Fully Pulsed Jets in Crossflow. *AIAA Journal*, 44(11):2719–25.

Johari, H., Pacheco-Tougas, M., and Hermanson, J. C. (1999). Penetration and mixing of fully modulated turbulent jets in crossflow. *AIAA Journal*, 37(7):842–50.

Johnston, C. R. and Wilson, D. J. (1997). A vortex pair model for plume downwash into stack wakes. *Atmospheric Environment*, 31(1):13–20.

M'Closkey, R. T., King, J. M., Cortelezzi, L., and Karagozian, A. R. (2002). The actively controlled jet in crossflow. *Journal of Fluid Mechanics*, 452:325–35.

Megerian, S., Davitian, J., de B. Alves, L. S., and Karagozian, A. R. (2006). Transverse jet shear layer instabilities - Part I: Experimental studies. to appear in the *Journal of Fluid Mechanics*.

Narayanan, S., Barooah, P., and Cohen, J. (2003). Dynamics and control of an isolated jet in crossflow. *AIAA Journal*, 41(12):2316–2330.

Overcamp, T. J. (2001). A review of the conditions leading to downwash in physical modeling experiments. *Atmospheric Environment*, 35:3503–8.

Shapiro, S. R., King, J. M., M'Closkey, R. T., and Karagozian, A. R. (2006). Optimization of controlled jets in crossflow. *AIAA Journal*, 44:1292–8.

Sherlock, R. H. and Stalker, E. A. (1941). A study of flow phenomena in the wake of smokestacks. *Engineering Research Bulletin No. 29, University of Michigan, Ann Arbor, MI. 49 pp.*

Smith, B. L. and Glezer, A. (1998). The formation and evolution of synthetic jets. *Physics of Fluids*, 10(9):2281–97.

Smith, B. L. and Glezer, A. (2002). Jet vectoring using synthetic jets. *Journal of Fluid Mechanics*, (458):1–34.

Snyder, W. H. and Lawson, R. E. (1991). Fluid modeling simulation of stack-tip downwash for neutrally buoyant plumes. *Atmospheric Environment*, 25A(12):2837–50.

CHAPTER 3

SUPPRESSION OF JET SHEAR LAYER INSTABILITIES IN A LOW MOMENTUM ELEVATED JET-IN-CROSSFLOW[1]

3.1 Introduction and Background

Jets-in-crossflow (JICFs) are typically formed from two geometries whereby the jet flow is injected perpendicularly into a cross-stream either from a pipe which is flush with a wall or from an elevated position through a stack. There is widespread use of the flow type in technological applications. In many of these applications the JICF's mixing characteristics have a direct impact on the performance and efficiency of the system. Usually, it is the thorough mixing of the fluids which is of critical importance. JICFs are indeed used for this purpose in combustion processes to mix fuel and oxidizer streams (Broadwell and Breidenthal, 1984), and in the environmental field for plume dispersion (Moussa et al., 1977) and stack flares (Johnson and Kostiuk, 2000). Naturally, an enhancement in JICF mixing would be beneficial in these systems. However, depending on the objectives of the application more mixing may not always be desirable. JICFs are also used in cooling applications, for example to apply film coolant to the surfaces of turbine blades. In this application coolant forms a film layer over the turbine walls to protect the surface from direct exposure to hot gases in the cross-stream. In this case it would be an advantage to suppress JICF mixing since convective mixing of the coolant with the cross-stream degrades the effectiveness of the film layer in protecting the surface (Haven and Kurosaka, 1996). For these reasons there is naturally a great deal of interest to control the properties of JICFs. Control of JICF mixing could significantly improve a great number of applications.

---

[1] Parts of these results were presented in two talks by the author. The first was a presentation entitled "Relaminarization of the vortex structure in a low velocity ratio jet in crossflow", by Watson, G. and Sigurdon, L., at the Annual Meeting of the Fluid Dynamics Division of the American Physics Society, Tampa, FL., Nov. 2006. The abstract was published in the Bulletin of the APS (Watson and Sigurdson, 2006). A second talk entitled "Suppression of jet shear layer instabilities in a low momentum elevated jet in crossflow", by Watson, G. and Sigurdon, L., presented further results at the Canadian Congress of Applied Mechanics Meeting in Toronto, ON., Jun. 2007. The abstract is published in the conference proceedings (Watson and Sigurdson, 2007).

Flow control techniques to modify the structure and penetration of wall-issued JICFs are in the literature. They were controlled by direct pulsation of the entire jet stream either by mechanically restricting the flow (Johari et al., 1999; Eroglu and Breidenthal, 2001; Johari, 2006) or by acoustic pulsation (M'Closkey et al., 2002; Shapiro et al., 2006). The studies demonstrated that under some conditions, the wall-issued JICF's penetration and/or spread could be modified by pulsation of the jet's velocity. The studies also report that when this occurs, there is only what appears to be an enhancement in mixing between the two fluid streams. The extent to which these strategies have an effect on the flow field depends on the JICF's initial unforced jet and crossflow momentum. The relative momentum of the fluids collapses into a single parameter termed the "jet-to-crossflow velocity ratio" defined in simplified form as $R \simeq W_j/U_\infty$ for a neurally buoyant JICF. W_j and U_∞ are the spatially-averaged jet and crossflow velocities, respectively. However, the JICF's response to forcing is complicated as there is a great deal of variability in the reported results.

The forcing technique in the present study differs from the techniques used in the wall-issued cases. In this case an elevated JICF, which is isolated from the effects of the wall boundary layer, is forced at the stack tip by a synthetic jet coaxial to the jet flow. The present study is an extension of the work of Diep and Sigurdson (2001) whose results were the first of its kind for this JICF geometry and forcing technique. The control method was initially developed to reduce downwash in low momentum elevated JICFs. We define a low momentum elevated JICF here as having a velocity ratio in the range $R \leq 1.5$ where the JICF penetration is adversely affected by pressure effects such as downwash and in-pipe separation, which are negligible at higher velocity ratios (Sherlock and Stalker, 1941). Synthetic jet forcing was indeed effective in reducing downwash (Diep and Sigurdson, 2002), however Diep and Sigurdson (2001) also observed that the forcing resulted in unexpected

JICF behaviour. A low amplitude coaxial synthetic jet has the effect of suppressing instabilities in the low momentum JICF to the point of complete "relaminarization" of the jet flow. Increased forcing, therefore, does not always increasing mixing. More work, which is reported here, was undertaken to understand the nature of the instability suppression phenomenon.

Smith and Glezer (1998) present detailed visualizations and measurements of the formation and evolution of nominally two dimensional synthetic jets. Synthetic jets are synthesized from a train of vortices which breakdown to form a mean flow which resembles a momentum jet. The vortices are formed at the edges of an orifice which has an oscillating flow of zero average mass flux passing through it. The flow field is similar to a conventional jet, however the synthetic jet flow consists only of ambient fluid. Conventional jets consist of source jet fluid as well as additional ambient fluid which is entrained into the jet flow from its surroundings. A synthetic jet has no source jet fluid. It consists only of ambient fluid in the vicinity of the orifice.

The vortex system of an elevated JICF is made up of several vortex structures. Four structures have been identified in the unforced elevated JICF: (i) Kármán-like stack wake vortices that are shed into the flow from the boundary layer on the outside of the stack (Eiff et al., 1995), (ii) jet wake vortices which connect vorticity just below the jet flow to vorticity within the stack wake (Eiff and Keffer, 1997), (iii) jet shear layer vortices which dominate in the near field (Huang and Lan, 2005), and (iv) the time-averaged formation of a counter rotating vortex pair (CVP) which is the dominant feature in the far field. This study focuses on structural modifications that occur in the jet shear layer vortices when the JICF is forced via open loop control.

Research into the structure and control of elevated JICF jet shear layer vortices are rare. Andreopoulos (1989) observed and sketched three types of vortex structures that occur within the unforced jet shear layer. The structures were termed mushroom-type, wake-like and jet-like vortices. The jet shear layer structure is highly dependent on the jet-to-crossflow velocity ratio. Diep and Sigurdson (2001) presented a series of images showing the jet shear layer's response to annular synthetic jet forcing and noted some vortex structural change as a function of forcing amplitude. The method of forcing is identical to the method used here. Additional work related to the JICF relaminarization is the subject of this paper. Recently, Huang and Lan (2005) have presented an in depth survey of the evolution process of unforced jet shear layer vortices in the low momentum elevated JICF. Their survey revealed five characteristic flow structures (three of which were first observed by Andreopoulos (1989)) whose behavior depended on the the jet-to-crossflow momentum ratio, R^2.

The Diep and Sigurdson (2001) relaminarization phenomenon is linked to the fundamental nature of the instabilities in the JICF. There has been substantial progress in the development of hydrodynamic stability theories for open shear flows. The instabilities are described based on their local and global characteristics. Here, the terms "local" refers to instabilities in the local profile and "global" refers to instabilities in entire flow field. The local instability in these cases is categorized as either *convective* or *absolute*. The difference between the categories is in the way that disturbances propagate in the fluid. In a locally convectively unstable flow disturbances propagate only in the downstream direction, however in a locally absolutely unstable flow disturbances grow both upstream and downstream. Put another way, convectively unstable profiles allow for temporal growth of disturbances, but the disturbances convect away from its origin with the bulk fluid motion. Absolutely unstable profiles allow for temporal growth of disturbances, but also allow for the spatial growth of disturbances originating at fixed streamwise locations.

The local instabilities' potential to dictate the global structure of the flow is best illustrated using simple mixing layers, free jets and wake flows as examples. These examples will be important for future discussions. In simple nominally two-dimensional mixing layers, the flow is *locally convectively stable* everywhere. As the disturbances convect along the streamwise direction their amplitude grows and their frequency diminishes as the shear layer thickens. However, due to the local convective nature of the profiles, the layer is *globally stable* in the sense that the disturbances cannot grow at fixed locations along the mixing layer since no "self-sustained resonant states" (Huerre and Monkewitz, 1990) can arise.

Huerre and Monkewitz (1990) describe the free jets as being split into two regions of local instability. In the near field, the developing jet shear layer profiles are *locally convectively unstable*. In the far field, at the limit of the potential core, the jet shear layer thickens to the point where the vortices on either side of the jet boundary interact with one another resulting in a global mode which has been termed the "preferred mode" of the free jet (Crow and Champagne, 1971). Huerre and Monkewitz (1990) classifies the far field profiles as "almost absolutely unstable." The global modes are preferentially amplified by forcing the flow in the neighborhood of the jet's global frequency.

Monkewitz (1988) describes two-dimensional wakes as also having two regions of local instability. In the near wake region, there is a large velocity deficit in the mean wake velocity profile that acts as a "resonance chamber" which preferentially amplifies some disturbances. These local profiles are *locally absolutely unstable.* In the far wake region, where the velocity deficit is reduced or eliminated, the wake flow is almost always *locally convectively unstable.* The preferentially amplified disturbances generated in the near wake region are swept downstream and amplified by the convectively unstable mean flow. Therefore, the global structure of the wake flow is first "selected" by a resonance effect in the near wake region and then amplified as he flow moves downstream (Koch, 1985). The wake flow, then, is *globally unstable* in the sense that there is a feedback of amplified disturbances causing self-excited global modes.

Nature of the instabilities in the JICF jet shear layer are complex. Until recently, it was generally thought that the initial formation of the jet shear layer vortices resulted from a Kelvin-Helmholtz-like instability similar to the convective instabilities in the near field of the free jet (Fric and Roshko, 1994; Kelso et al., 1996). Such an assumption does indeed appear to be valid at the high velocity ratios (Fric and Roshko, 1994). However, recent measurements by Megerian et al. (2006) suggest that this may not be the case at lower velocity ratios. Megerian et al. (2006) carried out a comprehensive survey of the JICF jet shear layer instabilities over a range of velocity ratios $1 \lesssim R \leq \infty$ for wall-issued and elevated JICFs. They noted some interesting observations related to the nature of the elevated JICF jet shear layer. At high velocity ratios $3.5 \leq R < \infty$, the spectral characteristics of the jet shear layer instabilities are similar to a free jet. However, at lower velocity ratios there were what appeared to be two prominent transitions in the nature of the elevated JICF instabilities. At $R \approx 1.5$ Megerian et al. (2006) measured a weakening in the instabilities which they attributed to growth of a non-negligible co-flow external to the upstream jet shear layer. Then for $R \leq 1.2$, strong instabilities returned in the jet shear layer which had different spectral characteristics from what they had measured at higher velocity ratios. It is in the lowest R range where Diep and Sigurdson (2001) observed the relaminarization phenomenon. Megerian et al. (2006) hypothesized that there may be a transition in the nature of the JICF jet shear layer instabilities from a convectively unstable flow at the higher velocity ratios to a flow with local profiles that are absolutely unstable at lower velocity ratios.

The aim of the present study was to determine the mechanism responsible for relaminarization of the low momentum elevated JICF. Since the relaminarization phenomenon is linked to the nature of the jet shear layer instabilities, the results have also shed further light on the fundamental nature of the instabilities in the low R range. The chapter is organized as follows. Section 3.2 describes the apparatus and measurement techniques. Section 3.3 presents a brief overview of the low momentum elevated JICF's structure and behaviour and Section 3.4 reports on the robustness of the Diep and Sigurdson (2001) relaminarization phenomenon. A description of the experiment is in Section 3.5 and a discussion of the results is presented in Section 3.6. Finally, Section 3.7 summarizes the experiments and presents the major conclusions.

3.2 Experimental Setup

3.2.1 The Apparatus

Experiments were carried out in a suction-type open-circuit wind tunnel with a measured turbulence intensity of 0.6%. The apparatus in this study was virtually identical to the one used in Diep and Sigurdson (2001). It is shown in Figure 3.1. The elevated JICF consisted of a one inch outer diameter, D, cylinder, or "stack", inserted half way into a 30.5 cm by 30.5 cm wind tunnel test section. The stack was constructed from two thin-walled brass tubes with one placed inside the other. The outer diameters of the inner and outer tubes were 20.6 mm and 25.4 mm (1"), respectively, and the wall thickness of both tubes was 0.74 mm. The jet flow issued from the inner tube with an initial jet diameter, d, of 19.12 mm and radius of $0.38D$, which gave an initial jet area that was 57% of the total stack cross-sectional area. The jet flow was laminar and was powered by a radial vane centrifugal blower.

A sinusoidal velocity fluctuation was introduced into the flow through a concentric annulus created from the space between the inner and outer tubes. The annulus had an inner width, h, of 1.64 mm. The annulus extended the length of the stack and through the wind tunnel wall to a sealed chamber fitted with a 8" diameter piston. The piston was driven by a shaker table (B&K Vibration Exciter Type 4809) which was excited by a specially built power oscillator and amplifier. The shaker table motion resembled the movement of a speaker, however the shaker table had the capability of supplying much higher pressure oscillations in order to overcome high viscous losses in the annulus. The piston movement created a sinusoidally varying pressure

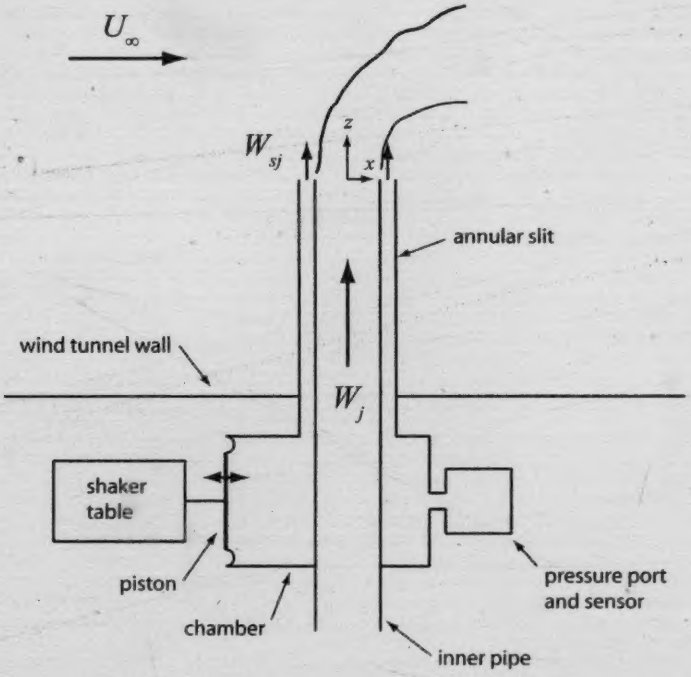

Figure 3.1: Schematic of the apparatus. The drawing is not to scale.

in the chamber which produced an oscillating flow within the annulus. The oscillating flow resulted in the formation of a synthetic jet flow at the stack exit plane. The flow created at the annulus will be termed "the synthetic jet" as opposed to the flow which emerged from the central pipe. The flow from the central pipe will be termed "the jet."

3.2.2 Flow Visualization

Smoke-seeded flow visualization was used extensively to obtain qualitative and quantitative information of the flow field. The jet was uniformly seeded with a glycerol and water based fog vapour from a RadioShack fog machine. The fog vapour was first injected into a plenum where it could be mixed with ambient air and cooled before it was drawn into the stack.

A smoke-wire visualization technique (Chapple, 1998; Corke et al., 1977), which places closely spaced streaklines into the flow, was used to seed the crossflow. A 0.005" wire was placed three diameters upstream from the stack just outside the viewing area of the camera. This position was used as a compromise between being too close to the JICF where the vorticity shed by the wire would have piled up in the stagnation region before it had time to diffuse, and being too far to reduce 3-D effects due to the diffusion of smoke from its initial line source. The alternating heating and cooling of the wire caused by a 60 Hz electric current created the effect of vertical timelines of denser and lighter smoke. The timelines have a frequency of 120 Hz due to the rectification property of resistive heating.

It was important to determine errors due to buoyancy effects of the slightly heated smoke. It was determined from flow images that the smoke rose 0.03 m/s in a uniform crossflow of $U_\infty = 0.7$ m/s, which was the lowest crossflow speed used in this study. The rise velocities were more or less constant over the range of crossflow velocities used, however the error in the measurements due to buoyancy will decrease with increasing crossflow velocity.

Photographs were taken from the side with a Nikon D1X camera using Nikon 60 mm and 105 mm lenses. The JICF was illuminated from above using General Radio Type 1540 Strobolumes. Light from the flash was collimated into a 1.0' to 1.5' wide light sheet along the JICF centerline.

3.2.3 Hot-Wire Measurements

Flow velocities in this study were on the order of 1 m/s. Their measurement required sensors with high sensitivities. Pitot-static readings were unreliable in this velocity range since the low differential pressures led to high uncertainties in the transducer reading (approximately 10% at 1 m/s). Instead, a 1.25 mm long, 5 μm diameter single-component hot-wire (Dantec Dynamics, platinum-plated tungsten, type 55P1) was used to obtain mean and fluctuating velocities in the flow field.

Horizontal velocity measurements of streakline images were used as the velocity standard for the low speed hot-wire calibration. An overview of the calibration method will only be provided here. It is described in detail in Appendix A. With all obstructions removed from the test section, a vertically mounted smoke-wire was placed a short distance downstream from the wind tunnel contraction. The hot-wire was also mounted in the wind tunnel test section, moved off to one side such that it was in a region of unform flow unaffected by perturbations from the smoke-wire. Velocity measurements were extracted from a single photograph of the streaklines exposed to two consecutive flashes of red and blue strobes set at a predetermined time difference. The errors in the velocity measurements were kept approximately constant at 1.5% of velocity reading. Overall, the time of flight method worked well over the calibration range, except below 0.08 m/s where the smoke's buoyancy affected the results.

Nominal jet and crossflow velocities were used in this study to describe unforced JICF operating parameters. Nominal conditions are those where the effects of the jet on the crossflow, or vice versa, were not present. Jet flow rates were determined by using a calibration of the jet velocity profile in no crossflow against the measured pressure drop across approximately thirty diameters of straight pipe. The jet velocity profiles were measured by a hot-wire traversed across the stack exit along the JICF centre plane two inner annulus widths, h, above the stack exit plane. Therefore, the spatially-averaged jet velocity, W_j, was based on an integration of the jet velocity profile. During the experiment, jet velocities were kept constant by dialing into the predetermined pressure drop value.

Crossflow velocities were also determined based on a calibration that used hot-wire measurements of the uniform cross-stream as the standard. A tachometer connected to the wind tunnel fan's drive motor allowed adjustment of the cross-stream velocity, due to the fact that the flow rate through the tunnel is linearly proportional to the rotational speed of the fan. A porous plate was installed upstream of the fan to increase the resolution of the calibration to 0.0079 m/s per RPM. A retractable TSI VelociCheck probe (Model 8330) with an accuracy of ±2.5 cm/s was also used to double check the crossflow measurements while running experiments.

Turning on the crossflow or the jet changes the velocity of the other, therefore there was some error in using the nominal values to describe the actual JICF operating parameters. Some factors which contributed to these errors were static pressure changes in the wind tunnel test section and blockage effects due the stack and jet flow. Errors due to blockage effects were not determined, however the effect of pressure changes on the jet flow rate was explored. Determination of this error was especially important due to the method employed to "dial in" the jet flow rate based on pressure drop during the experiments. The pressure drop used in the calibration was measured along a region of pipe where there was a *developing* velocity profile. Pressure drop is proportional to the jet flow rate, however the change in the static pressure difference between the wind tunnel test section and the atmosphere changed the evolution of the developing profile, complicating the calibration. Errors in the jet flow rate calibration due to this effect were determined by creating a static pressure difference in the wind tunnel without a crossflow by sealing the bell-mouth and using the wind tunnel fan to create suction in the test section. The velocity profiles of the jet flow were measured at different static pressures while the pressure drop along the pipe length was held constant. Actual jet momenta were found to be a maximum of 11% higher than their nominal values by integrating the velocity profiles. Accounting for all the errors in the analysis, there was to up to a 9% total uncertainty in the jet-to-crossflow velocity ratios in these experiments.

The hot-wire was also used in cases where point measurements were needed to characterize the synthetic jet flow. Hot-wires offer advantages in spatial resolution and frequency response which were important factors considering the width of the orifice and the oscillatory flow conditions in the synthetic jet's near field. The synthetic jet's velocity was determined along the centreline of the annulus from time traces containing at least 100 full synthetic jet cycles. The readings were ensemble averaged and phase locked to the actuation frequency. The measurements determined the peak centreline ejection velocity $w_{sj,max}$ at the exit plane $z/h = 0$ and the average synthetic jet velocity W_{sj} at $z/h = 2$. The measurement point for W_{sj} was chosen as a compromise between being too close to the synthetic jet orifice where flow reversal takes place, and too far to measure the momentum affecting the emerging jet flow. At $z/h = 2$ flow reversal was either minimal or non-existent for all cases.

Root mean square chamber pressure, P_c' and synthetic jet frequency, f_{sj} were measured by a Validyne DP15 pressure transducer fitted to the a pressure port on the chamber. Acquisition and processing of all pressure and hot-wire sensor data was done using a 12-bit AT-MIO-16-E National Instruments data acquisition board and LabVIEW® 4.1.1 at a sampling rate of 20 kHz.

3.2.4 Image Correlation Velocimetry

A reliable system was in place to visualize the JICF flow field. An aim of this study was to extend the visualization system to obtain whole field measurements of the wind tunnel centre-plane velocity field in the vicinity of the upstream jet shear layer. A form of Image Correlation Velocimetry was utilized for the measurements.

Apps (2001) and Apps et al. (2003) give a comprehensive overview of Image Correlation Velocimetry (ICV). The technique used here is similar to Particle Image Velocimetry, however the measurement relies on the correlation of patterns created by smoke structures rather than the imaging individual particles. The system was developed in-house to obtain velocity field information from streaklines which were generally used for flow visualization purposes already. Two strobes fitted with colour filters (one red and one blue) were flashed at a predefined time difference, Δt, to create a single image of the flow at two instants in time. An adaptation of the cross-correlation technique used by Papamoschou and Bunyajitradulya (1997) was used to determine the velocity field. The computational method applied cross-correlation between the scalar field enclosed by an interrogation window of predefined size (in this case 30 by 30 pixels) in the first (red) image and in the second (blue) image. The cross-correlation was repetitively calculated as the interrogation window was moved around the second image. The location where the cross-correlation was highest was assumed to be fluid displacement. The velocity was then determined from the displacement divided by the strobe delay, Δt. The algorithm also implemented an error correction technique named "correlation based correction" (Hart, 2000) to improve the result.

The imaging area in the present measurements extended out from the stack position upstream into the irrotational crossflow and downstream into the area where the jet evolved. The resulting raw red and blue smoke wire photograph spanned an image size that was 3008 by 1960 pixels, or was $10D$ in the cross-stream direction and $8D$ high. The ICV algorithm implements routines that improve its overall computational efficiency (Apps, 2001), however the calculation still would have required an enormous amount of time to analyze just one of the raw images (approximately 24 hours per image). In order to process the ICV results in a timely manner, while not compromising on vector resolution, the ICV algorithm was implemented on two smaller 800 by 600 pixels, overlapping sub-windows that enclosed the domain of interest. An example of the size and position of the sub-windows are indicated by the dashed boxes in Figure 3.2.

3.2.5 JICF Momentum Ratios

The characteristics of the JICF flow field are primarily defined by the jet-to-crossflow velocity ratio, R. All JICF tested in this study will be defined

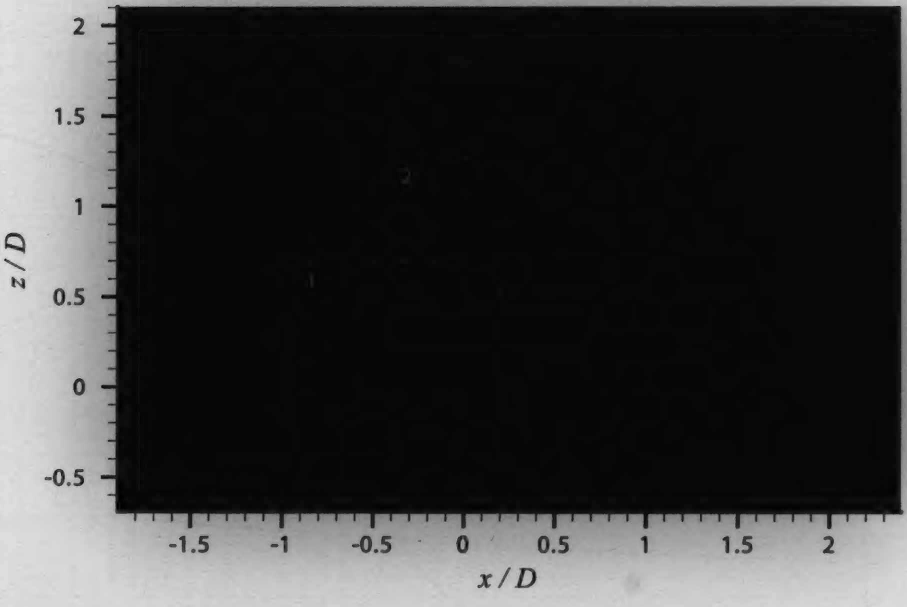

Figure 3.2: A sample image pair with time lapsed triggering of red/blue strobes. In this photograph, the red and blue components are instantaneous realizations of the scalar field taken $\Delta t = 2.2$ ms apart. The photograph shows the two 800 by 600 pixels sub-windows used in ICV.

by this ratio. Therefore, a precise definition of the R was important for the measurements. The jet-to-crossflow velocity ratio is a simplified form of a momentum ratio shown in expanded form below

$$R = \alpha^{\frac{1}{2}} \left(\frac{\rho_j}{\rho_\infty}\right)^{\frac{1}{2}} \left(\frac{W_j^2}{U_\infty^2}\right)^{\frac{1}{2}} \tag{3.1}$$

where α is the "momentum flux correction factor" which was used to account for the difference in momentum between an assumed top-hat velocity profile in the momentum flux equation and the actual viscous velocity profile of the jet flow. In this study, the JICF was neutrally buoyant, therefore the density ratio in Equation 3.1, ρ_j/ρ_∞, is unity.

The synthetic jet adds additional momentum to the total JICF profile. For the forced JICF, it is useful to account for the additional momentum in a new formulation of the velocity ratio named the "momentum velocity ratio", M_M, first derived by Diep and Sigurdson (2002). M_M is defined as a ratio of momentum fluxes

$$M_M = \left(\frac{F_t}{\rho_j U_\infty^2 A_m}\right)^{\frac{1}{2}} \tag{3.2}$$

where F_t is the total momentum flux of the jet and synthetic jet flows applied over the total stack area ($F_t = F_j + F_{sj}$) and A_m is the "momentum-weighted area." A_m is an empirical weighting which was formulated based on Diep and Sigurdson's experimental data which showed that the synthetic jet momentum dominates the elevated JICF at high velocity ratios. Both terms are shown in expanded form below

$$F_t = \alpha \rho_j A_j W_j^2 + \frac{\rho_\infty + \rho_j}{2} A_{sj} W_{sj}^2 \tag{3.3}$$

$$A_m = \frac{F_j A_j + F_{sj} A_{sj}}{F_t} \tag{3.4}$$

where A_j and A_{sj} are the initial jet and synthetic jet annulus areas, respectively. The synthetic jet momentum flux, F_{sj}, was estimated using the average centerline velocity of the synthetic jet, W_{sj}, and the exit area of the annular slit assuming a top-hat profile. The actual synthetic jet profile was not determined. The value was not precisely the momentum flux, but F_{sj} was expected to be proportional to the true momentum flux of the synthetic

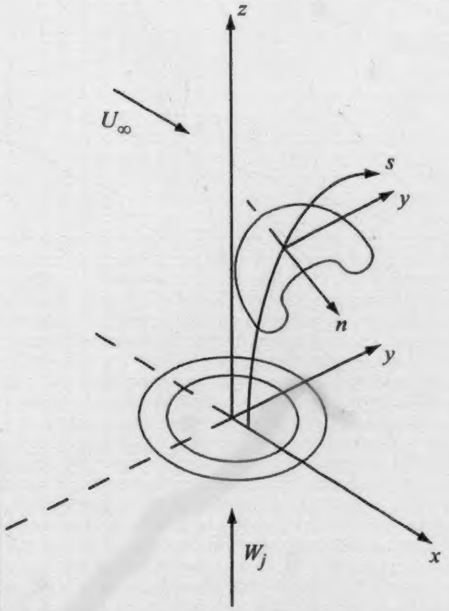

Figure 3.3: JICF coordinate systems.

jet. It should be noted that when the JICF is not forced by the synthetic jet, Equation 3.2 yields $M_M = R$.

3.2.6 Coordinate Systems

Figure 3.3 shows a schematic of the coordinate systems used in these experiments. For some of the measurements it was better to define a coordinate system that could convey the downstream evolution of the JICF. An orthogonal coordinate system was defined for this purpose such that the positive-s axis was tangential to the JICF scalar centreline. The negative-n axis pointed toward the oncoming crossflow towards the "upstream side" of the jet shear layer while the positive-n axis pointed toward the "downstream side." The (s, n) and (z, x) planes lay though the axis of symmetry ($y = 0$). The positive y axis pointed into the page.

There are many definitions for the JICF centreline. In the present study, the centreline was the approximate near field jet trajectory based on the *scalar concentration*. Therefore, the jet trajectory intersects the JICF's maximum mean concentration[2]. The trajectory was not based on velocity field measurements, nor was it based on a streamline originating at the centre of the stack exit. As noted by Smith and Mungal (1998), Kamotani and Greber (1972) and Haniu and Ramaprian (1989) reported that for high momentum, wall-issued, turbulent JICF in the far field, centrelines based on the maximum local velocity penetrated $5 - 10\%$ deeper than the scalar centreline[3]. We also expect a similar difference in the centrelines in the near field as well (see Appendix B).

3.3 The Relaminarization Phenomenon

We begin our presentation of the results with flow visualization. The visualizations gave important initial insights into the JICF's structure and behaviour which guided us in subsequent measurements. This section presents side view photographs of the low momentum JICF in its natural, unforced condition and also its modified structure when it is forced by an annular synthetic jet. A great deal was learnt from the visualizations, however only the information relevant to this chapter will be discussed here.

We shall start with the unforced JICF. Huang and Lan (2005) carried out an extensive survey of the unforced jet shear layer vortices under similar geometric and flow conditions. Their survey identified five characteristic jet shear layer vortex structures whose occurrences were highly dependent on momentum ratio, R^2. Experiments in this wind tunnel have reproduced the same characteristic vortex structures, but all the structures will not be presented here, nor will the vortices' evolution be discussed in detail. We have selected only a few photographs which are relevant to the scope of the study.

Figure 3.4 shows a sequence of three elevated unforced JICFs with decreasing velocity ratios. The velocity ratio was lowered by decreasing the jet velocity. The crossflow velocity is constant. Figure 3.4(a) shows that the JICF is unstable at $R = 1.36$. The instability begins with the formation of a train of counter-clockwise rotating vortices on the upstream side of the jet shear layer, however the whole JICF becomes unstable as the flow evolves.

---

[2] for more information on how the jet trajectory was determined please see Appendix B.

[3] the scalar quantity in these measurements was temperature.

Huang and Lan (2005) termed this flow structure "jet-type vortices." The jet shear layer vortices come and go intermittently, however when they develop the roll up of the vortices appears to be periodic.

When the velocity ratio is reduced the roll up of vortices in Figure 3.4(a) occurs farther from the stack exit until the JICF becomes completely stable in the near field at $R = 1.13 \pm 0.09$. Figure 3.4(b) represents the minimum observed mixing between the jet and crossflow for the unforced case.

At lower velocity ratios there is an abrupt transition back to an unstable flow structure. The general configuration of the vortex structure, which resembles Huang and Lang's "backward-rolling vortices," is shown in Figure 3.4(c) at $R = 0.69$. Vorticity visible in the jet shear layer originates from fluid inside the stack boundary layer and separated flow from the outer stack wall (Andreopoulos, 1989). The structure and formation of the vortices at these low velocity ratios are quite different from Figure 3.4(a). Roll-up of vortices in the jet shear layer are regular and periodic. The vortices' frequency is highly dependent on velocity ratio over a wide range of crossflow Reynolds numbers (Huang and Lan, 2005). Roll-up of vorticity occurs in the upstream and downstream jet shear layers close (less than a diameter) from the stack exit plane and are locked into the same natural formation frequency, f_n. The vortex structures seen in the photographs, are actually quite strongly three-dimensional. These photographs are two-dimensional projections of the three-dimensional translucent structures integrated along the light path to the camera.

The elevated JICF's natural stability is strongly dependent on the jet-to-crossflow velocity ratio. Complete natural suppression of the instabilities in the near field occurred at $R = 1.13 \pm 0.09$ up to a critical jet Reynolds number of $\mathrm{Re}_{d,\mathrm{crit}} \approx 1660$, which approaches the accepted Reynolds number for transition from laminar to turbulent pipe flow. These observations are consistent with other studies. Megerian et al. (2006) measured a reduction in the strength of the upstream jet shear layer instabilities with decreasing velocity ratio until $R \approx 1.25$ for the constant jet Reynolds numbers $\mathrm{Re}_d =$ 2000 and 3000. The difference in the velocity ratios from our study could be related to differences in the JICF geometry. Megerian et al. (2006) used a nearly top-hat jet profile with a relatively small jet momentum thickness ($\theta/D = 0.053$) and a much shorter stack height than in this case. Huang and Lan (2005) also report a notable change in the jet shear layer vortex structure in a similar JICF geometry from unstable "swing-induced vortices"

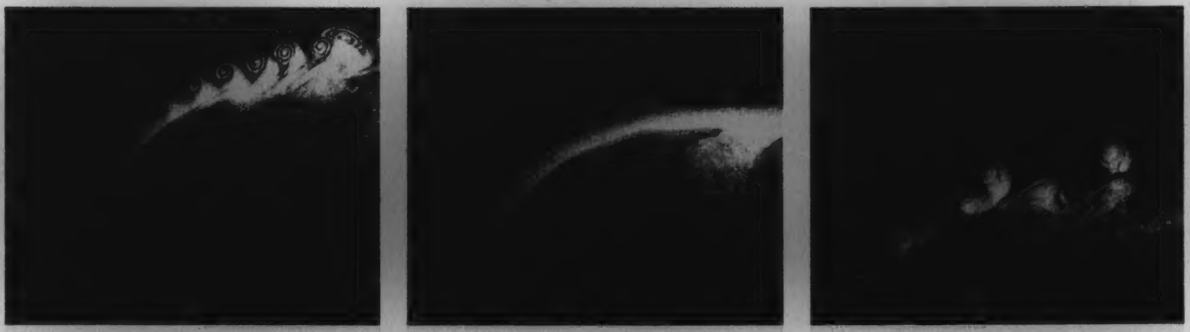

(a) (b) (c)

Figure 3.4: Photographs of some of the unforced JICF jet shear layer structures for the range of velocity ratios $1.36 \leq R \leq 0.69$. The crossflow velocity is constant, $\mathrm{Re}_\infty = 1270$, (a) unstable jet shear layer with "jet-type vortices." $R = 1.39$, $\mathrm{Re}_d = 1147$, (b) stable jet shear layer. $R = 1.17$, $\mathrm{Re}_d = 975$, (c) unstable jet shear layer with "backward-rolling vortices." $R = 0.69$, $\mathrm{Re}_d = 574$.

to "jet-type vortices" at $R \approx 1.16^4$. However, they do not report complete natural suppression of the jet shear layer instabilities. Huang and Lan's tests were done at a crossflow Reynolds number of $\mathrm{Re}_\infty = 2051$, which for their geometry translates to a jet Reynolds number of $\mathrm{Re}_d = 1602$ at $R \approx 1.16$. The jet Reynolds number is close to our transitional value which may be why Huang and Lan (2005) did not report the dramatic change in the stability properties of the JICF that we have observed.

We shall now briefly present a series of photographs in Figure 3.5 of structural changes that occur when the low velocity ratio elevated JICF is forced by the annular synthetic jet. Initial observations of this case are presented as a sequence of photographs in Diep and Sigurdson (2001) and Diep and Sigurdson (2002), but the photographs presented here provide additional insight into the phenomenon. Figure 3.5(a) shows the initial unforced JICF vortex structure. It is the same unstable "backward-rolling" vortex structure photographed in Figure 3.4(c). The crossflow and jet velocity are $U_\infty = 0.75$ m/s and $W_j = 0.45$ m/s, respectively giving an initial velocity ratio of $R = 0.69$. The crossflow and jet velocities are constant throughout the sequence of photographs. Streaklines in the crossflow-seeded photograph show the periodic roll-up of a vortex above the leading edge of the stack which contains negative vorticity (into the page by the right hand rule) from the boundary later on the outer stack wall. The negative vortices are periodically shed into the upstream jet shear layer and then evolve downstream as part of the unstable jet shear layer vortex structure.

A striking change in the jet shear layer vortex structure in Figure 3.4(b) occurs with low amplitude 60 Hz synthetic jet forcing. In these photographs $W_{sj} \approx 0.3$ m/s. Eventually the JICF is made steady and the jet flow completely relaminarizes in the near field. The near field is defined as the area where the JICF's trajectory still has a non-negligible vertical component, which is approximately three to four jet diameters in this case. Relaminarization is a forced suppression of the naturally occurring jet shear layer instabilities in a naturally unstable JICF which is formed from laminar pipe flow. In this chapter, we shall term this behaviour "the relaminarization phenomenon." We will only use this term when discussing controlled suppression of the JICF instabilities in this range of velocity ratios, $R \leq 1.13$. In this photograph, the relaminarization corresponds to approximately a 66%

---

[4] the velocity ratio presented here for the Huang and Lan (2005) data has been corrected to account for their parabolic profile.

(a) Reference photographs of the JICF with no forcing, $W_{sj} = 0$ m/s, $\mathrm{Re}_d = 570$, $R = M_M = 0.69$. The upstream and downstream vortices have the same formation frequency.

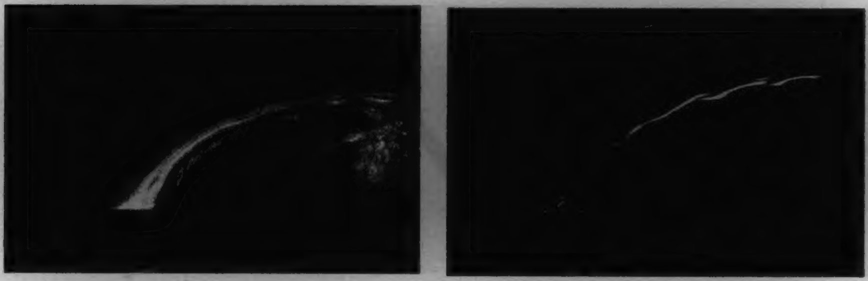

(b) JICF Relaminarizes, $W_{sj} \approx 0.3$ m/s, $\mathrm{Re}_d \approx 660$, $M_M \approx 0.77$.

Figure 3.5: For caption see the next page.

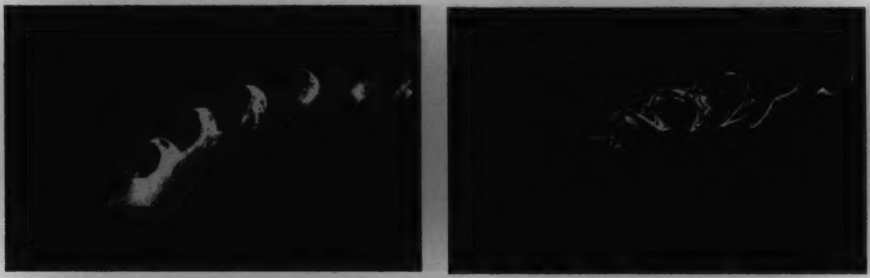

(c) Vortices reappear on the upstream side of the jet shear layer locked into the forcing frequency. Vortices are downstream-pointing, $W_{sj} \approx 0.9$ m/s, $\mathrm{Re}_d \approx 1130$, $M_M \approx 1.26$.

(d) JICF lifting off and more turbulent, $W_{sj} \approx 1.2$ m/s, $\mathrm{Re}_d \approx 1500$, $M_M \approx 1.6$.

Figure 3.5: Change in structure of a low momentum elevated JICF with 60 Hz synthetic jet forcing increasing in amplitude. Paired photographs show the JICF at the same operating parameters, but visualized with jet-seeded and crossflow-seeded flow in the left and right photographs, respectively. In the sequence of photographs the crossflow velocity is constant, $\mathrm{Re}_\infty = 1270$. All yet Reynolds numbers are back calculated from M_M.

drop in turbulence intensity ($w_{j,o}/W_j$) along the centreline of the jet profile at $z/h = 2$. The crossflow-seeded photograph shows the evolution of negative vorticity not visible in the jet-seeded photograph. The vortices are locked into the forcing frequency near the stack exit, however the definition in the smoke structures diminishes rapidly downstream. It should be noted that the relaminarization is only effective in the near field. It does not stop the JICF's eventual transition to turbulence in the far field. It only delays the transition.

A vortex structure shown in Figure 3.5(c) grows out of the relaminarized JICF with increased forcing amplitude. The vortices are locked into the synthetic jet forcing frequency. A vortex pair which originates from the annulus is visible in the crossflow-seeded photograph. The vortex pair appears to be the basic component which comprises the mushroom vortex arrangement on the upstream jet shear layer. In this photograph, the mushroom vortices roll clock-wise and point downstream entraining jet fluid as they evolve. However, the direction of pointing can also be made to point upstream depending on the forcing amplitude (Diep and Sigurdson, 2001). Pointing refers to the direction the pairs would self-propagate, which is connected to the impulse of the pair.

The JICF begins to lift off and become more turbulent as forcing amplitude is further increased in Figure 3.5(d). The JICF penetrates into the cross-stream much deeper and shows a considerable amount of vertical jet spread. A vortex pair is visible in the the crossflow-seeded photograph which is laminar when ejected from the annulus, but it quickly becomes turbulent as it evolves along the jet shear layer. The formation process is typical of fully formed synthetic jet flows and is commonly seen in visualizations of synthetic jets in a quiescent fluid (Smith and Glezer, 1998). Smith and Glezer (1998) showed that the vortex pairs consistently transitioned to turbulence when the suction stroke began. The pairs ultimately broke down into a mean turbulent jet flow profile in the far field. This formation process may indeed be occurring in this case as well.

3.4 Testing the Limits of the Relaminarization Phenomenon

3.4.1 The Experiment

A parameter survey was undertaken to determine the limits of the relaminarization phenomenon. A range of naturally unstable low momentum elevated

JICFs, with R less than the stable unforced condition at $R \approx 1.13$ (shown in Figure 3.4b), were forced with synthetic jets over a range of formation frequencies in an attempt to suppress the jet shear layer instabilities over a wide parameter range. The frequency range was 50 Hz $\leq f_{sj} \leq$ 250 Hz. Three crossflow Reynolds numbers were also chosen to test for Reynolds number effects, $\mathrm{Re}_\infty = 1200$, 1500 and 1800.

The JICF stability was characterized visually with jet-seeded flow visualization. For each synthetic jet frequency, f_{sj}, the forcing amplitude was increased until minimum mixing was observed between the jet and the crossstream. At this point, the synthetic jet operating parameters were measured with a single component hot-wire along the centreline of the annulus at the exit plane ($z/h = 0$) and RMS chamber pressure readings. Measurements at the annulus exit were made with the crossflow turned off. Thirteen frequencies were tested within the frequency range 50 Hz $\leq f_{sj} \leq$ 250 Hz. Within the lower range 50 Hz $\leq f_{sj} \leq$ 150 Hz, where the synthetic jet apparatus performed well, the frequencies were spaced ten hertz apart. Two additional frequencies were used at 200 Hz and 250 Hz which were at the operational limit of the forcing apparatus. At the lower end of the frequency range, the synthetic jet's operation was limited by the minimum amplitude of the oscillator. The natural frequencies of the jet shear layer vortices were 25 Hz $\lesssim f_n \lesssim$ 40 Hz. Therefore, all synthetic jet frequencies were above the natural frequency of the jet shear layer vortices being approximately twice to ten times higher than the lowest f_n.

3.4.2 Synthetic Jet Measurements

Characterization of synthetic jets in the near field is complicated by the periodic and spatially evolving nature of the flow field. We had to make do with some standard assumptions since an understanding of the synthetic jet's formation and characteristics is still an ongoing area of research.

Compressibility effects can be significant within the chamber since the apparatus is effectively a Helmholtz resonator (Holman et al., 2005). Therefore, calculation of the synthetic jet operating parameters cannot be determined by knowing the oscillator motions and applying continuity. Instead, direct measurement of the flow velocity at the annulus exit must be done to determine the parameters.

The standard approach is to characterize the synthetic jet based on dimensionless parameters related to the initial formation of the vortex pairs.

These parameters are based on a simple "slug-velocity profile model" (Smith and Glezer, 1998). The first parameter is the dimensionless "stroke" length which is defined as L_o/h where L_o (the "slug length") is the distance that a slug of ejected fluid travels during the ejection phase. The slug length is defined formally as

$$L_o = \int_0^{\tau} \langle w_{sj,o}(t) \rangle dt \tag{3.5}$$

where $w_{sj,o}(t)$ is the centreline synthetic jet velocity at the exit plane of the annulus and τ is the time of discharge or the half period of the piston motion, $\tau = 1/(2f_{sj})$. The triangular brackets denote ensemble averaging. A second parameter is a Reynolds number based on the impulse of the vortex pair (or the momentum of the fluid discharge) per unit depth, $\mathrm{Re}_{I_o} = I_o/\mu h$. I_o is defined as

$$I_o = \rho h \int_0^{\tau} \langle w_{sj,o}(t) \rangle^2 dt \tag{3.6}$$

Additional dimensional parameters are the synthetic jet frequency, f_{sj} and the duty cycle, which is fixed at 100%. Based on this information L_o and I_o can be simplified assuming a sinusoidal centreline velocity fluctuation

$$L_o = \frac{\langle w_{sj,max} \rangle}{\pi f_{sj}} \tag{3.7}$$

$$I_o = \frac{\rho h \langle w_{sj,max} \rangle^2}{4 f_{sj}} \tag{3.8}$$

where $w_{sj,max}$ is the peak ejection velocity at the exit plane of the annulus. Other researchers (Smith and Glezer, 1998; Holman et al., 2005) have also found it useful to define an approximate synthetic jet Reynolds number based on the velocity scale $U_o = L_o f_{sj}$ which gives $\mathrm{Re}_{U_o} = U_o h/\nu$. U_o is essentially a measure of the celerity of the vortex pairs determined from the distance the slug travels during the ejection phase, but is averaged over the synthetic jet's full cycle.

3.4.3 Results

We have found that the occurrence of the relaminarization phenomenon does not depend on the applied forcing frequency. Forced suppression of the jet shear layer instabilities was observed for all JICFs tested over the entire synthetic jet frequency range. In most cases, the synthetic jet causes complete suppression of the jet shear layer instabilities, however the quality of the suppression varies. Ridges in the forced jet shear layer locked into the forcing frequency do occur in some cases, especially in cases that require relatively large synthetic jet amplitudes for instability suppression to occur.

Quantitative measurements of the synthetic jet flow gave additional insight into the forced relaminarization phenomenon. Figure 3.6 summarizes the results of hot-wire measurements of the impulse of the synthetic jet's vortex pairs, I_o, at the point of maximum observed instability suppression. I_o can be regarded as the total impulse of the fluid in the annulus required to generate the vortex rings from rest. In an unbounded fluid the impulse is an invariant in the vortex pair motion. The invariance of I_o once the vortex ring moves away from the annulus makes the impulse one of the main parameters that allows the synthetic jet to be ordered according to the strength of the vortex rings. The impulse measurements have been non-dimensionalized into a Reynolds number, Re_{I_o}. The Reynolds numbers are plotted against a Strouhal number $\mathrm{St}_d = f_{sj}d/W_j$ whose characteristic dimension and velocity are from the jet flow. For clarity, only the five JICFs tested at a crossflow Reynolds number of $\mathrm{Re}_\infty = 1200$ are shown on the graph. It was found that the impulse measurements were a stronger function of velocity ratio than crossflow Reynolds number and that the lowest crossflow Reynolds number gives the widest possible velocity ratio range. There is considerable scatter, however the general trend in the data shows that more impulse (i.e. more synthetic jet momentum) is required to suppress the jet shear layer instabilities at lower velocity ratios. The higher impulse corresponds to higher forcing amplitudes and, therefore, larger velocity fluctuations ($w'_{sj,o}/W_j$) in the vicinity of the synthetic jet exit plane. The "peaks" in the impulse curves suggest a non-linear behaviour, however the peaks line up roughly when synthetic jet frequency is normalized by St_d.

At this crossflow Reynolds number, $8.23 \leq \mathrm{Re}_{U_o} \leq 37.24$ and $0.41 \leq L_o/h \leq 2.83$, which are lower than the typical values of fully formed synthetic jets reported in the literature. For this annular geometry Holman et al. (2005) predict a synthetic jet formation threshold of $L_o/h > 2$, which is higher than most dimensionless stroke lengths in this study. Holman et al. (2005) define the formation threshold as the minimum dimensionless stroke length required for vortex breakdown to occur and a fully turbulent synthetic jet to form in the far field. Their idea of a formation threshold is similar in some respects

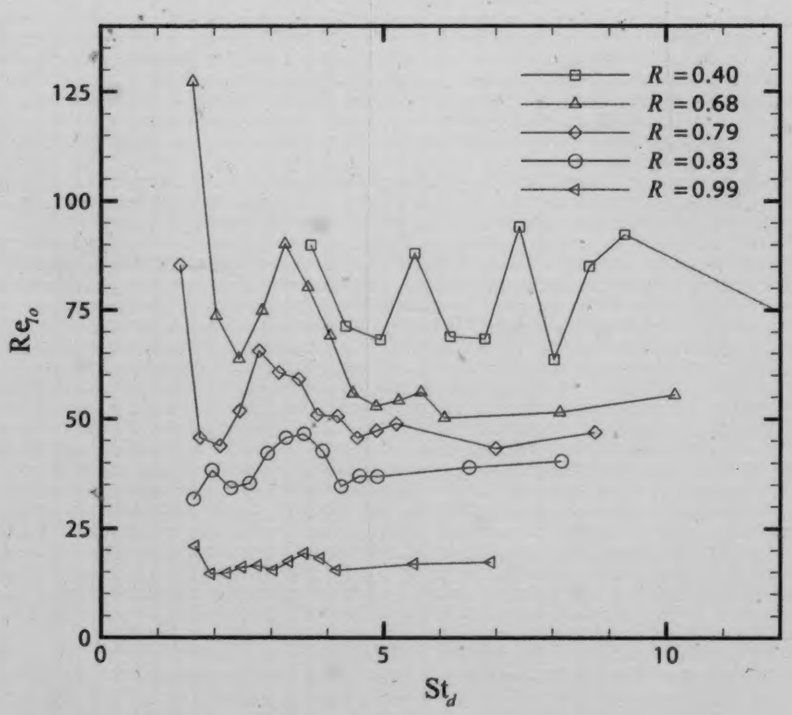

Figure 3.6: Reynolds number based on the hydrodynamic impulse, $\mathrm{Re}_{I_o} = I_o/\mu h$, verses Strouhal number based on synthetic jet forcing frequency, $\mathrm{St}_d = f_{sj}d/W_j$.

to the Gharib et al. (1998) theory for a universal time scale for the roll up and formation of vortex pairs and rings. In this experiment $L_o/h = 2$ is only surpassed in the lowest velocity ratio cases where the impulse is highest, for $R < 0.68$. Therefore, the synthetic jets used to relaminarize the JICF may not be considered by some (Holman et al., 2005) as being fully formed, but rather may be considered to be in a "transitional state."

There are two important findings that must be emphasized before moving on. The occurrence of relaminarization phenomenon does not depend on the forcing frequency. It is actually strongly affected by the synthetic jet momentum. Higher forcing amplitudes and, therefore more synthetic jet momentum, is required to relaminarize JICF at lower velocity ratios.

3.5 JICF Operating Points

We have presented an overview of the relaminarization phenomenon. However, field measurements were needed to obtain a more detailed description of the flow field to propose a mechanism for the flow's behaviour.

Operating points for the jet and crossflow velocities were chosen to obtain field information over a range of velocity ratios. The operating points consisted of a constant jet velocity of $W_j = 0.7$ m/s and four crossflow velocities. The unstable JICFs were relaminarized with three synthetic jet frequencies: 60 Hz, 100 Hz and 140 Hz. There was less than 5% total harmonic distortion in the forcing frequencies. A summary of the operating points are listed in Table 3.1 with their velocity ratios, R and M_M, and their forcing frequencies. M_M was determined from synthetic jet velocities W_{sj} determined after the field measurements were taken by matching synthetic jet frequency and RMS chamber readings, therefore M_M should be viewed as approximate values.

The operating points in Table 3.1 have also been assigned run letters. From here on, the results will be referred to as cases by these run letters. It should be noted that cases designated with an 'A' as their second letter correspond to unforced JICFs. These cases were considered to be the baseline conditions from which the forced data was compared. Case DA has no corresponding forced case because the JICF is naturally stable at its velocity ratio, $R = 1.17$. Strouhal numbers relating to the natural frequencies of the jet shear layer vortex structures (i.e. the frequency of the global instabilities) are also given.

Table 3.1 also gives information pertaining to the ICV parameters used for each test case. A summary of the location and size of the sub-windows is

Table 3.1: Experimental Operating Parameters: The table is split into JICF and ICV parameters. The Strouhal numbers, St_d, are based on the frequency of the vortices in the jet shear layer, f_n, and the synthetic jet frequency, f_{sj}, respectively. A Strouhal number is not reported for two reasons: (i) the jet shear layer was stable and the JICF was steady, or (ii) no synthetic jet forcing was applied.

	JICF Parameters							ICV Parameters		
					St_d					
Case	Re_∞	Re_d	$R \simeq W_j/U_\infty$	M_M	$f_n d/W_j$	$f_{sj} d/W_j$	Jet Shear Layer Condition	Number of Photographs	Δt (ms)	Potential Maximum Pixel Error (cm/s)[% $/W_j$]
AA	1170	890	1.17 ± 0.09	1.17 ± 0.09	–	–	stable	114	3.00	±1.22[1.74]
BA	1480	890	0.92 ± 0.07	0.92 ± 0.07	0.80	–	unstable	102	2.50	±1.46[2.08]
BB	1480	890	0.92 ± 0.07	0.93 ± 0.09	–	1.64	stable	105	2.50	±1.46[2.08]
BC	1480	890	0.92 ± 0.07	0.93 ± 0.09	–	2.73	stable	107	2.50	±1.46[2.08]
BD	1480	890	0.92 ± 0.07	0.93 ± 0.09	–	3.82	stable	103	2.50	±1.46[2.08]
CA	1830	890	0.75 ± 0.06	0.75 ± 0.06	1.10	–	unstable	112	2.20	±1.65[2.36]
CB	1830	890	0.75 ± 0.06	0.77 ± 0.07	–	1.64	stable	107	2.20	±1.65[2.36]
CC	1830	890	0.75 ± 0.06	0.79 ± 0.07	–	2.73	stable	107	2.20	±1.65[2.36]
CD	1830	890	0.75 ± 0.06	0.78 ± 0.07	–	3.82	stable	113	2.20	±1.65[2.36]
DA	2235	890	0.61 ± 0.06	0.61 ± 0.07	1.57	–	unstable	113	2.00	±1.82[2.60]
DB	2235	890	0.61 ± 0.06	0.66 ± 0.07	–	1.64	stable	107	2.00	±1.82[2.60]
DC	2235	890	0.61 ± 0.06	0.66 ± 0.07	–	2.73	stable	111	2.00	±1.82[2.60]
DD	2235	890	0.61 ± 0.06	0.67 ± 0.07	–	3.82	stable	110	2.00	±1.82[2.60]

	JICFs Relaminarized with synthetic jets with frequencies $f_{sj} = 60$ Hz, 100 Hz and 140 Hz		
Case AA $R = 1.17 \pm 0.09$	Case BA $R = 0.92 \pm 0.07$	Case CA $R = 0.75 \pm 0.06$	Case DA $R = 0.61 \pm 0.06$
		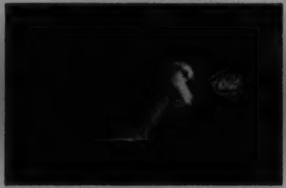	

Figure 3.7: A visual representation of the operating parameters. The photographs show jet-seeded visualizations of the initial unforced jet shear layer structures. The unsteady JICFs were relaminarized with synthetic jets with three formation frequencies (not shown).

given along with the pixel resolution. For each case, multiple realizations of the flow field were taken and averaged to produce a time-averaged vector field. The number of photographs used in the calculation are listed in the table. Δt between the firing of the red and blue strobes are in the table as well. The time was chosen as a compromise between errors related to cross-correlation and to the potential maximum pixel error. The potential maximum pixel error has been shown in the table as well, however it is estimated that the error in the measured velocity is larger Sigurdson and Apps (2003).

Figure 3.7 shows a visual representation of the operating parameters. The photographs show jet-seeded visualizations the initial unforced jet shear layer structures. The JICF ranges from being stable at the highest velocity ratio ($R = 1.17$) to unstable at lower velocity ratios with swing-induced, forward rolling and backward-rolling vortex structures, respectively.

3.6 Results and Discussion

3.6.1 Jet Velocity Profiles

Figure 3.8 shows a hot-wire trace of the emerging jet flow profile in the absence of a crossflow ($R \to \infty$). The measurements were taken at $z/h = 2$ above the stack exit plane along the (x, z) plane of symmetry. The shape of the velocity profile is close to a perfect parabola. It has a momentum flux that is only 0.7% higher than an ideal axi-symmetric parabolic profile. Turbulence intensity values are also somewhat symmetric with a maximum value of 3.6% close to the centreline. Due to the jet profile's closeness in shape and momentum to an axi-symmetric parabolic profile, a fixed momentum flux correction factor of $\alpha = 4/3$ has been used for the jet flux throughout the data analysis. This is indeed a reasonable assumption since W_j is a control variable in the sense that the volume flux through the jet tube is fixed at $W_j = 0.7$ m/s for these experiments. It must be emphasized that the vorticity in the profile has diffused inwards to its fullest extent at the stack exit plane. Therefore, the viscous region of the jet profile has an initial thickness which is already sizable ($0.5d$) at the stack exit plane. Therefore, the jet shear layer does not develop from negligible thickness, as it would in a top-hat profile.

JICF velocity profiles were also measured for all test runs. Figure 3.9(a) and (b) shows a comparison of the profiles for the stable and relaminarized JICFs for case BA and BC, respectively. The profiles where also measured along $z/h = 2$ through the JICF symmetry plane. The wire was perpendicu-

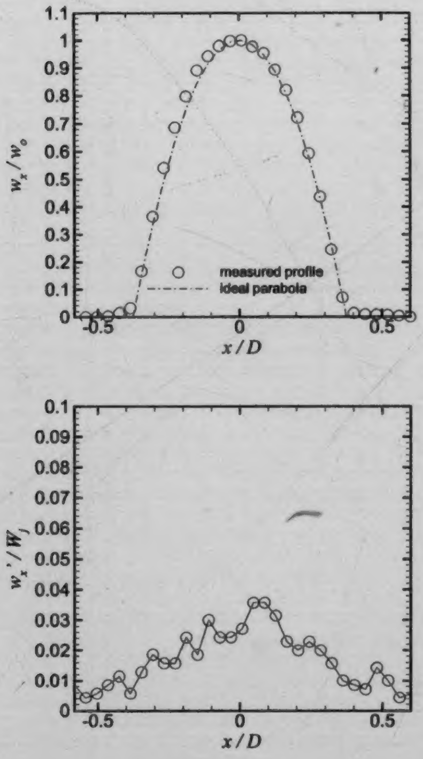

Figure 3.8: Jet velocity and turbulence intensity profiles in no crossflow, $R \rightarrow \infty$. Velocities are normalized by the peak centreline velocity in the profile, w_o. The profile is measured at a location $z/h = 2$ above the stack exit plane. The conditions correspond to a jet Reynolds number of $\mathrm{Re}_d = 890$.

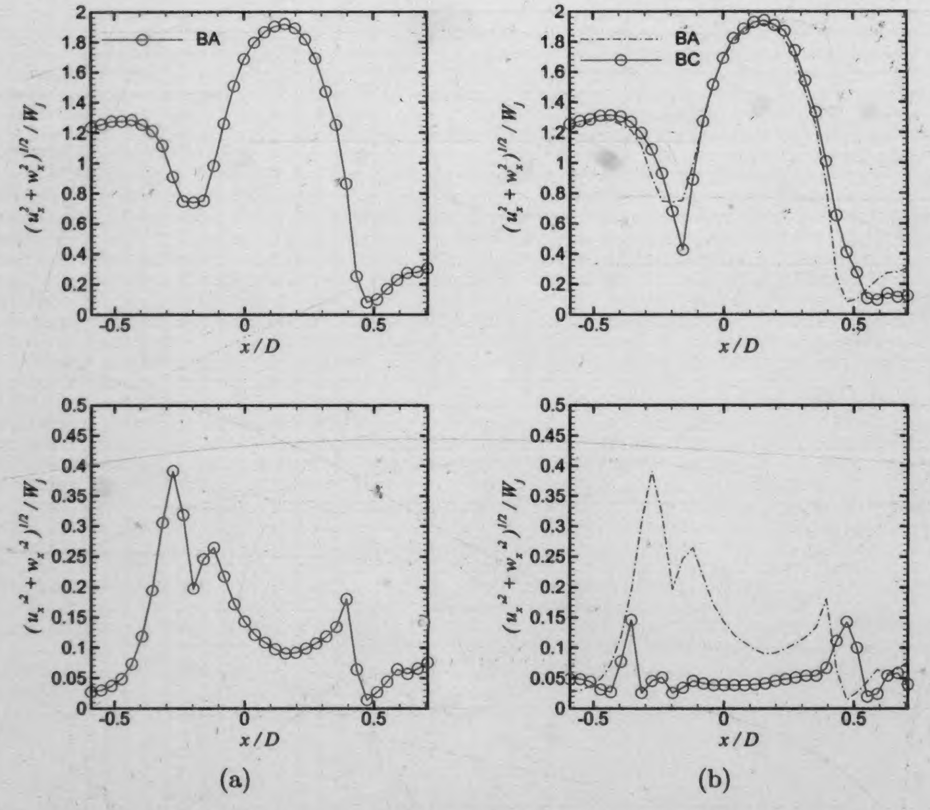

Figure 3.9: Jet velocity and turbulence intensity profiles for unforced and relaminarized JICFs, cases BA and BC. Velocities are normalized by the mean jet velocity, W_j. The profiles are measured at a location $z/h = 2$ above the stack exit plane. The conditions correspond to a jet Reynolds number of $\mathrm{Re}_d = 890$. (a) Case BA, unstable, (b) Case BC, relaminarized.

lar to the symmetry plane. A single component hot-wire was used for these measurements, therefore was no way to tell flow direction. The v component of the velocity is negligible along the JICF symmetry plane, therefore the velocity is assumed to be the magnitude of the u and w components. The unforced, unstable JICF velocity and turbulence intensity profiles are shown in Figure 3.9(a). A co-flow is visible external to the upstream jet profile, however the exact magnitude of the co-flow velocity is unknown since it is expected that there are errors in the velocity readings due to hot-wire orientation. For these measurements, the hot-wire probe holder was perpendicular to the crossflow. It was determined that the error external to the jet shear layer could be as high as 25% if the flow was perpendicular to the probe holder. However, it is expected that the error is smaller within the jet core, where the flow velocity was still primarily vertical.

There are significant changes in the relaminarized profile, in Figure 3.9(b). Overall, additional synthetic jet momentum increases the total momentum of the JICF profile, as was indicated by the higher M_M values in Table 3.1. In this case, the peak velocity in the jet profile is 1% higher than the unforced case, however the change in the peak velocity a maximum of 8% higher at the lower velocity ratios in the experiment, where more synthetic jet momentum is needed to relaminarize the flow. Relaminarization of the JICF also coincides with large reductions in the turbulence intensity in the JICF profile. The peaks in turbulence intensity on upstream and downstream sides of the profile (at $x/D \approx 0.5$ and -0.5) are the result of fluctuations in the unsteady synthetic jet flow.

3.6.2 Vector Field Measurements

Figure 3.10 shows the extracted time-averaged vector field on the upstream side of the JICF for case AA, $R = 1.17$. Each vector is a description of the average magnitude and direction of the flow velocity at a point on the spatial grid from 114 realizations of crossflow-seeded red/blue photographs. The contour field is the average intensity of the red and blue images which gives a representation of the time-averaged smoke field. The coordinate system is normalized by stack diameter, D, and the stack and the annulus are drawn for reference.

The ICV algorithm requires that photographs contain at least some scalar structure for the method to work. It is best for the interrogation windows to contain a dense field of distinct scalar structures since it improves the corre-

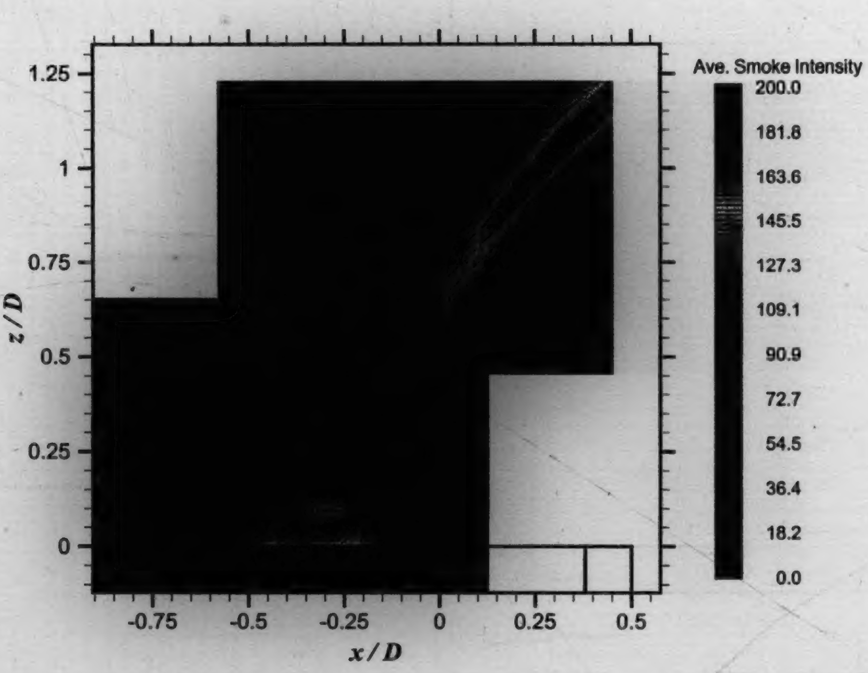

Figure 3.10: Time-averaged vector field for case AA. The colour contours represent the average intensity of the red and blue components in the photographs.

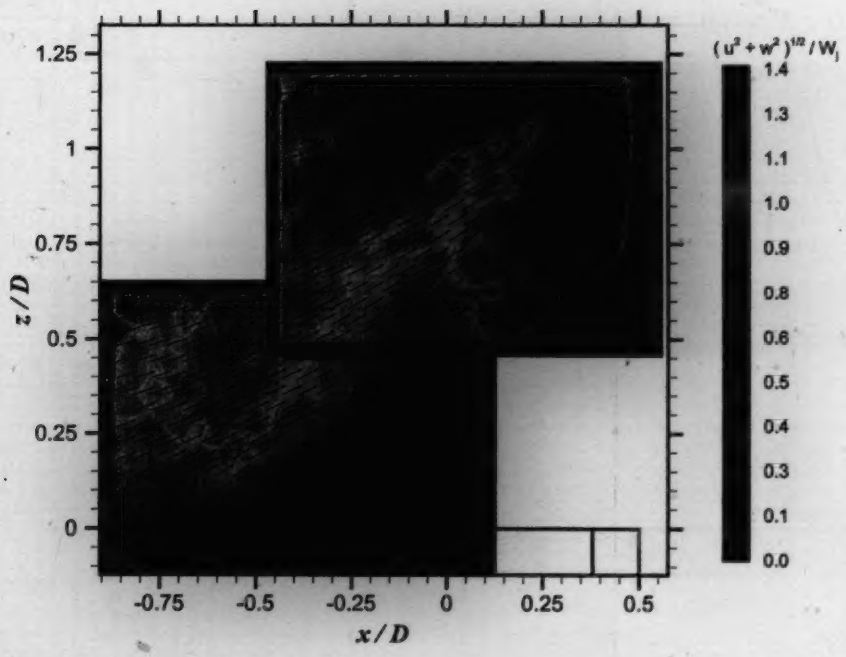

Figure 3.11: (a) Time-averaged vector field for case BA. The colour contours are the magnitudes of the of the vectors normalized by W_j.

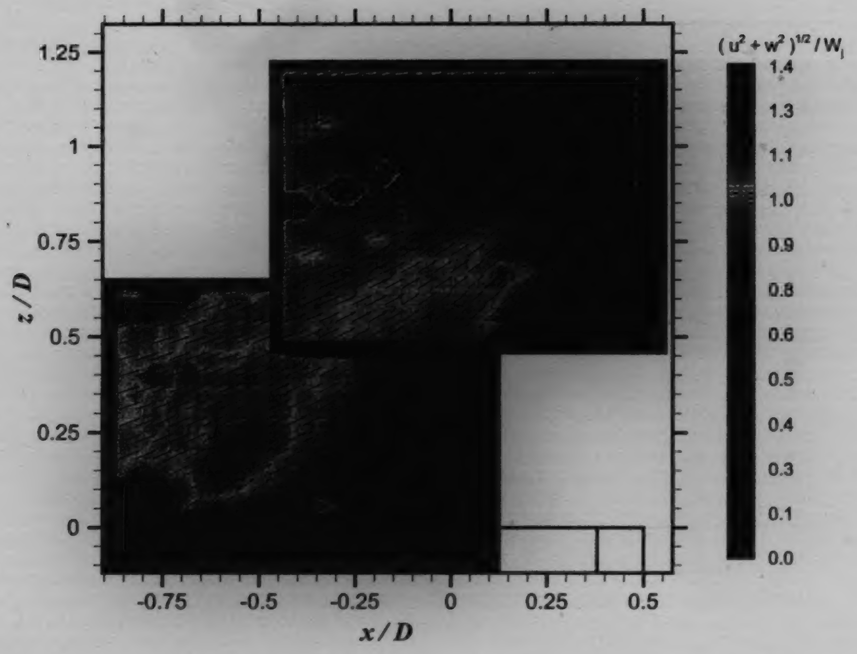

Figure 3.11: (b) Time-averaged vector field for case BC. The colour contours are the magnitudes of the of the vectors normalized by W_j.

lation between the red and blue images and gives better results. Sometimes there was not enough structure within the interrogation windows to obtain a high enough correlation between the images. Only vectors determined from at least an 85% correlation between the red and blue images are used in the analysis. All time-averaged vectors reported here are the average of at least 40 instantaneous vectors. Above 40 vectors fluctuations in the moving average were less than 6% of the averaged value. Vectors were also deleted from the time-averaged velocity field in areas where the flow structure was observed not to be primarily two-dimensional.

ICV obtains full vector field information in the near field on the crossflow side of the jet shear layer. Figure 3.10 shows what may be the formation of a time-averaged separation bubble above the leading edge of the stack which contains vorticity from the outer stack wall boundary layer. The formation of the vortex is also observed in crossflow-seeded visualizations of the unsteady cases in Figure 3.5(a). In this case, there is no instability in the jet shear layer and the flow is steady. Therefore, the separation bubble exists as a steady flow structure in both instantaneous and time-averaged velocity fields.

The effect of synthetic jet forcing on the flow field will be discussed qualitatively by comparing the time-averaged vector fields of the unsteady and relaminarized 'B' series cases in Figure 3.11(a) and (b), respectively. Only the unforced case BA and the forced case BC are discussed to simplify the comparison. However, the trends which will be noted in the comparison are common to all 'B' series cases and to the 'C' and 'D' series as well. The contour plots in the figures represent the magnitudes of the time-averaged vectors normalized by the mean jet flow velocity, W_j. The magnitude and direction of the fluid entering and exiting the measurement domain are similar in both cases. Cross-stream fluid entering the measurement area upstream from the stack has already begun to slow down and deflect upwards. Flow that enters the domain below the stack exit plane is particularly slow, with speeds that are approximately 30% of the free-stream value, U_∞, and a direction which is almost parallel to the stack and the emerging pipe flow. The flow accelerates as it moves parallel to the jet shear layer. The flow velocity exiting the measurement domain is approximately 130% of the free-stream value. The magnitude of the deflected crossflow is most affected close to the stack and JICF boundaries. The flow away from these boundaries are deflected upwards, however their magnitudes are close to the free-stream velocity. The slowdown and then acceleration of the cross-stream does indeed have some similarities to the flow pattern over a blunt faced object. In this case, it is the stack and jet flow that act as the flow obstacle, however the flow field is more complex primarily due to the fact that the jet flow is not a solid boundary.

The synthetic jet's effect is most pronounced in a region close to the stack exit plane. For the unsteady case BA in Figure 3.11(a) there appears to be the time-averaged formation of a separation bubble above the leading edge of the stack which is similar in structure to the vortex in the time-averaged vector field in case AA (see Figure 3.10). Velocity magnitudes on the crossflow side of the jet shear layer in the vicinity of the stack exit plane are approximately 30% of the mean jet velocity. The velocity deficit persists for a short distance along the jet shear layer, but ultimately diminishes as the flow accelerates along the JICF trajectory.

The synthetic jet has drastically modified the flow field close to the stack exit plane in case BC. The steady, relaminarized time-averaged velocity field in Figure 3.11(b) does not show the the formation of a time-averaged vortex above the stack leading edge, nor is velocity deficit in the vicinity of the stack exit plane as severe. The synthetic jet appears to have two effects on the initial development of the jet shear later. First, it entrains faster moving fluid closer to the jet shear layer's upstream side, and secondly it reduces the magnitude of the velocity deficit near the stack exit plane. Time-averaged velocity magnitudes local to the stack exit plane are about 2.7 times higher than in case BA. The velocity field measurements indicate that the synthetic jet flow modifies the time-averaged jet shear layer profile by the addition of momentum and/or entrainment. Synthetic jet momentum is added to the whole JICF profile, as was shown in Section 3.6.1. However, the synthetic jet's effect on the upstream flow profile is mostly localized, having the most effect on the initial development of the jet shear layer.

3.6.3 Time-Averaged Jet Shear Layer Velocity Profiles

Velocity profiles were extracted from the field information to obtain quantitative information of the synthetic jets' effects on the evolution of the upstream jet shear layer profiles. A schematic of the data extraction method is in Figure 3.12. The velocity profiles were obtained from the time-averaged vector fields along straight lines at different locations, s/D, perpendicular to the JICF trajectory. The extracted vectors were then projected onto the s-axis so that a common axis could be used to compare the velocity magnitudes.

Seeding the crossflow did not allow for measurements of the jet side of

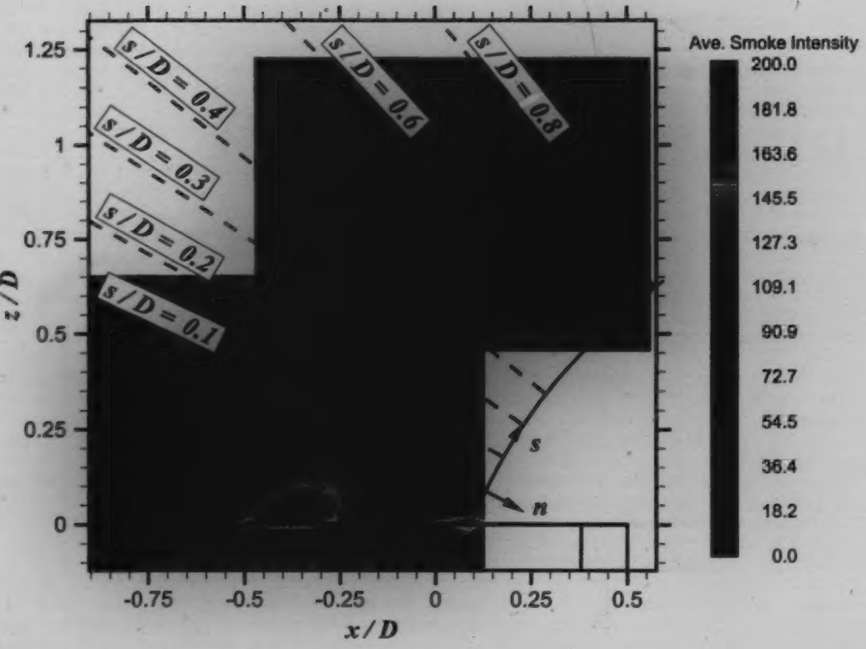

Figure 3.12: Schematic of locations of velocity profiles for case BA. Velocity profiles are extracted from time-averaged velocity fields perpendicular to the approximate JICF trajectory (the s-axis).

the upstream jet shear layer profile. This is certainly a weakness in the analysis since characterization of the jet shear layer instabilities requires at least approximate dimensions of the jet side of the profile. To make-up the shortfall in the measurements, the JICF trajectory and W_j were used to approximate the viscous thickness and the peak velocity on the jet side of the profile, respectively. Due to the axi-symmetric parabolic profile close to the exit plane, the peak velocity is approximated as simply $2W_j$. Error bars will displayed with the results to account for the upper and lower bounds for these approximations, and other measurement uncertainties.

Another potential issue of inaccuracy relates to the averaging method used and the oscillatory fluctuations close to the synthetic jet annulus. Use of time-averaging of the flow field instead of ensemble averaging likely affects the accuracy of velocity measurements above the synthetic jet annulus due to the large periodic fluctuations caused by flow reversal. Velocity measurements in this region are also probably not accurate due to the three-dimensionality of the flow separation around the leading edge of the stack. Therefore, the velocity profiles are extracted outside of this region at least $z/h = 2$ from the synthetic jet annulus where flow reversal due to the source/sink flow does not occur and the flow structures are primarily two-dimensional.

The evolution of the time-averaged profiles along the JICF trajectory, $0.1 \leq s/D \leq 0.8$, are shown in Figure 3.13 for case BA. The figure documents the transition of the crossflow side of the jet shear layer from what appears to be a wake-like profile near the stack exit to the initial development of what may be a jet shear profile further downstream. Data points in the profiles have increased spread furthest from the stack exit. There is maximum 8% deviation in velocity from the fitted lines. The reduction in accuracy may be related to a degradation in ICV performance due to a decline of distinct scalar structures in the crossflow-seeded photographs further along the jet trajectory. There are a great deal of distinct scalar patterns in the streaklines near the stack exit. A higher density of structural information has a beneficial effect on the accuracy of the correlation technique. However, as the streaklines evolve downstream there is a reduction in the distinctiveness of the scalar patterns that is useful for image correlation. Downstream, the ICV technique must instead rely on the striations in the streaklines of denser and lighter smoke to correlate the images. This typically results in reduced accuracy of the method (Apps, 2001; Sigurdson and Apps, 2003). Therefore, we assume a 15% error in all ICV measurements when reporting the results (Sigurdson and Apps, 2003).

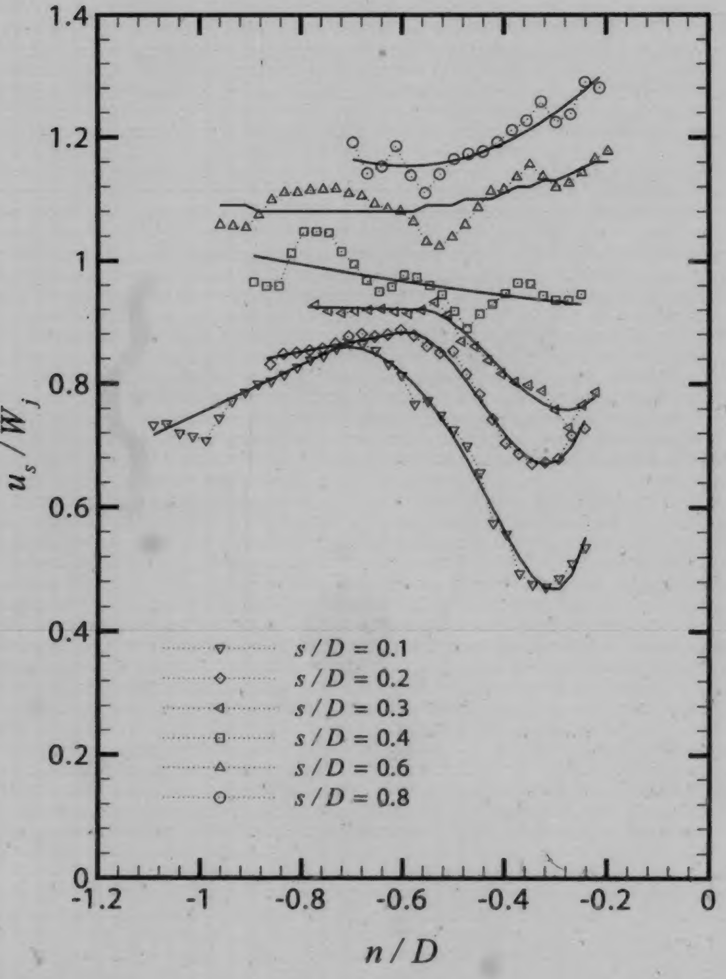

Figure 3.13: Evolution of time-averaged velocity profiles at different positions s/D along the jet trajectory. This is case BA. The velocities are normal to the jet trajectory.

The synthetic jet's effect is most pronounced nearest to the stack exit plane, therefore from now on we shall restrict our discussion to the flow profiles at $s/D = 0.1$. Regardless of the errors, there is indeed a well defined boundary between the viscous jet shear layer profile and the irrotational crossflow. The boundary's location is where there is an abrupt drop in the magnitude of the flow velocity. There is also a monotonic decrease in the velocity magnitude with distance away from the JICF in the irrotational flow, however the effect is caused by the crossflow's direction being more horizontal upstream from the stack. The apparent reduction in velocity is not due to the diffusion of vorticity.

In nominally parallel viscous flows in a uniform irrotational stream, such as the Blasius boundary layer and symmetrical wake flows, it is standard practise to define the viscous thickness based on δ_{99} taken at the point where the velocity in the profiles becomes $0.99U_\infty$. In this flow, a strict definition for δ is more difficult. The flow evolution of the JICF is neither parallel to the free-stream, nor does the irrotational flow exterior to the jet shear layer have a fixed velocity magnitude. The jet shear layer has an evolving profile with exterior irrotational velocity magnitudes which are non-uniform in the streamwise direction. For these measurements we shall approximate the boundary of the viscous region as being located at the peak velocity magnitude in these profiles. For such an approximation to work, it has been assumed that flow in the time-averaged profiles are locally quasi-parallel in the region directly surrounding the jet shear layer.

Figure 3.14 is a schematic of the anatomy of the complete upstream jet shear layer profile at $s/D = 0.1$. The jet shear layer is the viscous region of the profile between the peak jet and crossflow velocities. The schematic shows only the upstream side of the JICF profile – the downstream side of the JICF is not shown. The total thickness of the upstream jet shear layer is defined by δ. There are two velocity differences in the profile. The first is the velocity difference between the peaks of the profile ΔU_{peak}, which is an indicator of the strength of the co-flow external to the upstream jet shear layer. The second is the velocity deficit in the profile $\Delta U_{profile}$ defined as the difference between the average velocity of the peaks, U_p, and the lowest velocity within the jet shear layer profile. The dominant velocity difference likely dictates the local flow behaviour.

Figure 3.15 tracks the magnitudes of ΔU_{peak} and $\Delta U_{profile}$ as a function of velocity ratio. When $R \gtrsim 1.13$, it is ΔU_{peak} that dominates the profile. The peak jet velocity is largest at these velocity ratios, therefore it may be best in

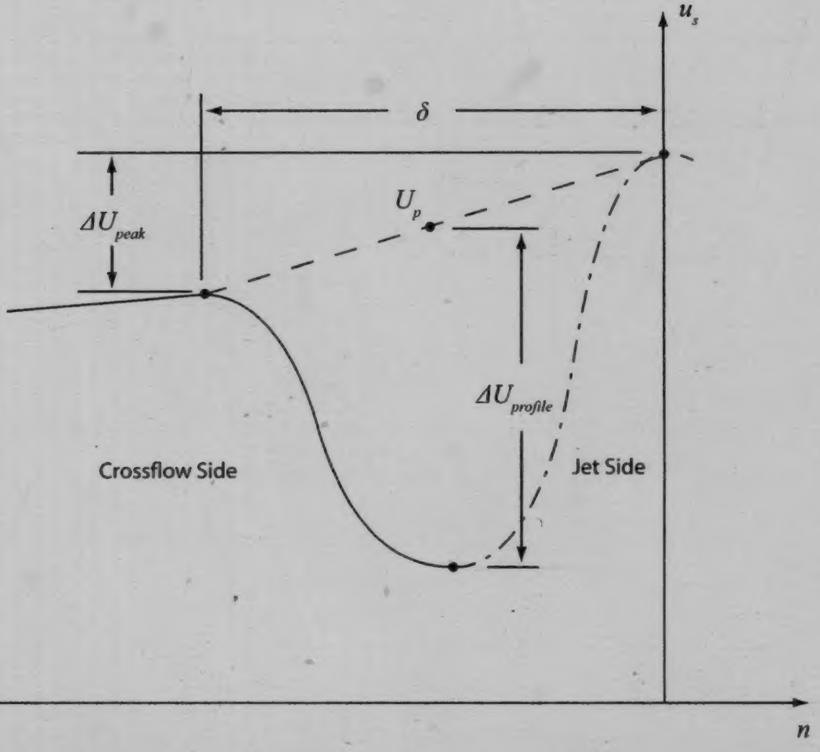

Figure 3.14: Schematic of local upstream jet shear layer velocity profile parameters at $s/D = 0.1$. The profile is split into regions labeled the "crossflow side" and "jet side". The crossflow side of the profile is determined from ICV. Relevant jet side values are approximated from jet trajectory and hot-wire measurements.

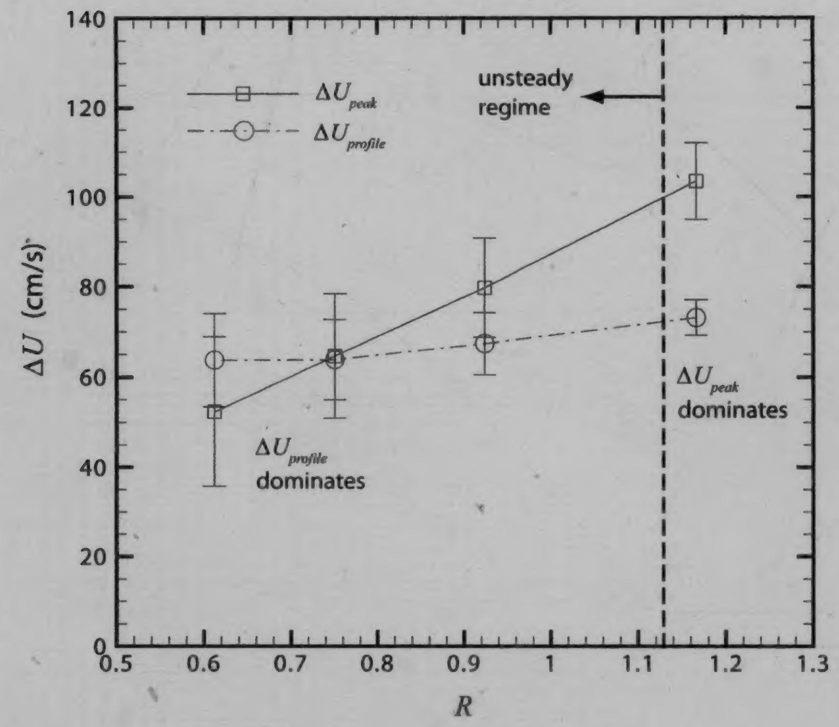

Figure 3.15: Velocity differences, ΔU as a function of velocity ratio, R. The line separating the co-flow and wake flow regions at $R = 1.13$ is based on flow visualizations of the JICF vortex structure.

this case to characterize the upstream profiles using a co-flowing jet scaling. The magnitude of ΔU_{peak} rapidly diminishes as R decreases. W_j is constant in these measurements, therefore the reduction in the magnitudes of ΔU_{peak} are due to increasing velocities in the region exterior to the jet shear layer. This trend was also measured by Megerian et al. (2006) in their elevated geometry. For $R \lesssim 1.13$, within the present domain of the measurements, we surmise that it is $\Delta U_{profile}$ that matters when characterizing the profile. Within this domain of velocity ratios, the magnitude of the velocity deficit in the local jet shear layer profile, $\Delta U_{profile}$, is equivalent to or is larger than ΔU_{peak}.

3.6.4 Critical Reynolds Numbers

Approximate local Reynolds numbers of the upstream jet shear layer profiles were calculated based on a wake flow scaling using the dimensions obtained at $s/D = 0.1$. The initial developing region of the jet shear layer does indeed have some properties that make it analogous to a wake flow. The most apparent property being a velocity deficit near the stack exit plane. The width of the jet shear layer, δ, and the magnitude of the velocity deficit, $\Delta U_{profile}$, are used to calculate the local Reynolds number of the upstream jet shear layer profile, $\mathrm{Re}_\delta = \Delta U_{profile}\delta/\nu$. The results of the Re_δ scaling are are shown in Figure 3.16 and are tabulated in Table 3.2. This data reduction is the result of the determination of 2822 velocity fields and approximately 59 days of continuous computational time. Local Reynolds numbers of the unforced jet shear layer profiles increase monotonically with decreasing velocity ratio. The values coincide with the observed behaviour of the JICF in Figure 3.7, which transitions from a stable flow in case AA ($R = 1.17$) to an unstable flow at lower velocity ratios.

The synthetic jet has a remarkable effect on the local Reynolds number of the profile. The forced data in Figure 3.16 indicates the Re_δ necessary for relaminarization. To differentiate these values from the unforced, unstable cases, the Reynolds numbers will be labeled $\mathrm{Re}_{\delta,\mathrm{crit}}$. Relaminarized jet shear layer profiles have lower Reynolds numbers than the unstable profiles. The synthetic jet flow reduces the local Reynolds number of the jet shear layer profile below a critical value for suppression of an unstable flow. Another interesting trend in the forced data is that suppression of the instabilities at lower velocity ratios occurs at lower $\mathrm{Re}_{\delta,\mathrm{crit}}$. The trend in the data could be related to the synthetic jet forcing amplitude. In Section 3.4.3 we noted

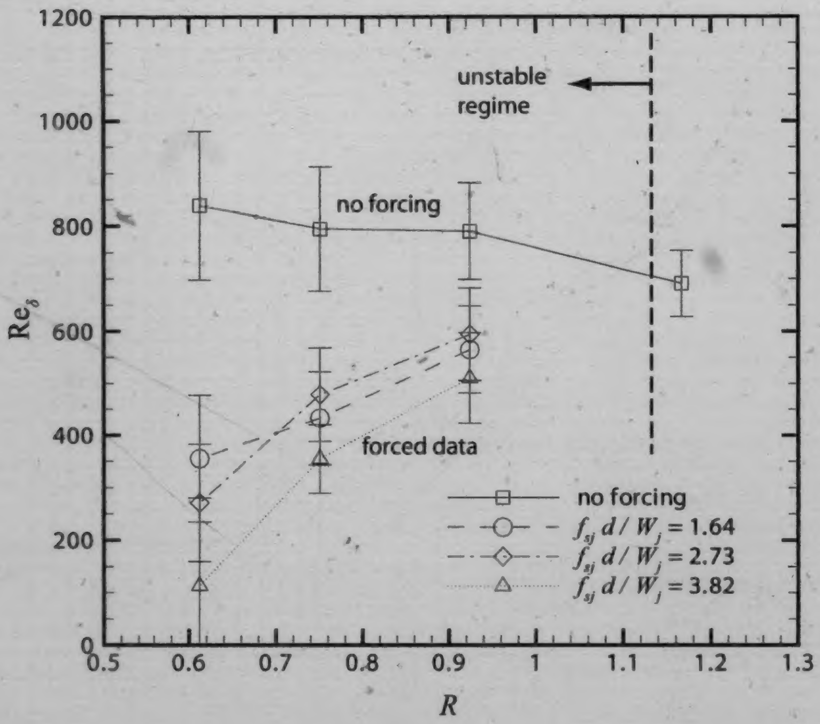

Figure 3.16: Changes in the local Reynolds numbers, Re_δ, with velocity ratio. Local Reynolds numbers are calculated from velocity profiles at $s/D = 0.1$. All data to the left of the vertical dashed line are in the unstable regime where the unforced JICF is naturally unstable. The forced data indicates the maximum Re_δ necessary for relaminarization ($\mathrm{Re}_{\delta,\mathrm{crit}}$).

that higher forcing amplitudes are required to relaminarize the flow at lower velocity ratios. Therefore, the lower Reynolds numbers, or the stabilizing effect of viscous damping, could be required to damp out the larger amplitude velocity fluctuations in the synthetic jet's near field. In any case, as velocity ratios increase, and the fluctuations from the synthetic jet flow decrease, the local Reynolds numbers of the relaminarized jet shear layer profiles become closer to the unforced, stable value of $\mathrm{Re}_{\delta,\mathrm{crit}} \approx 700$, which is outside the unstable regime.

The decreasing trend in $\mathrm{Re}_{\delta,\mathrm{crit}}$ could also bean artifact of the data analysis, to some extent. The computed Reynolds numbers do not account for increases in the peak jet velocity due to the contribution of additional synthetic jet momentum to the whole JICF profile. The Reynolds numbers are instead based on an approximation for the peak jet velocity which only accounts for the jet volume flux, which is fixed in these experiments. The increase in the peak velocity is greater at lower velocity ratios due to increasing forcing amplitudes. Therefore, the drop off in $\mathrm{Re}_{\delta,\mathrm{crit}}$ with lower velocity ratios could be shallower than what is reported here.

It should be emphasized that the Reynolds numbers presented here characterize the local stability properties of the jet shear layer profiles only at $s/D = 0.1$. The value of Re_δ for the time-averaged profiles changes with downstream distance, however the trends at $s/D = 0.1$ may also occur at other streamwise positions. We speculate that this will be the case closer to the stack exit plane where the velocity deficit in the profile is expected to be much larger.

The jet shear layer/wake flow analogy can be extended further by defining an additional global Reynolds number for the whole upstream jet shear layer. The definition will be similar to the standard Reynolds number scaling for bluff body wake flows. The scaling is based on a fixed characteristic dimension, usually the base thickness of the buff body, and the approaching free-stream velocity. In bluff bodies, changes in this Reynolds number are primarily linked changes in the approaching irrotational free-stream velocity. Kármán vortex shedding ceases when a drop in the free-stream velocity reduces the Reynolds number of the wake from a supercritical to a subcritical value $Re < Re_{crit}$.

The global Reynolds number of the upstream jet shear layer is scaled by the outer annulus width, H, and the average peak velocity in the profile, U_p, measured at at $s/D = 0.1$, giving $\mathrm{Re}_H = U_p H/\nu$. For this data reduction it may be helpful to think of U_p as a loose approximation of the irrotational

Table 3.2: Approximate Reynolds Numbers Computed from Velocity Profiles of the Jet Shear Layer at $s/D = 0.1$, $1.17 \leq R \leq 0.61$: Different parameter combinations are presented. Re_δ is the local Reynolds number of the profile and Re_H is the global Reynolds number of the wake flow.

Case	$\mathrm{Re}_\delta = \Delta U_{profile}\delta/\nu$	$\mathrm{Re}_H = U_p H/\nu$
AA	691 ± 63	184 ± 7
BA	791 ± 92	208 ± 10
BB	565 ± 83	210 ± 10
BC	594 ± 89	209 ± 10
BD	511 ± 87	210 ± 10
CA	795 ± 118	224 ± 12
CB	434 ± 90	220 ± 12
CC	479 ± 90	224 ± 13
CD	355 ± 65	217 ± 11
DA	839 ± 141	237 ± 15
DB	356 ± 121	235 ± 14
DC	271 ± 112	238 ± 15
DD	114 ± 167	245 ± 16

component of the viscous profile. Therefore, U_p is, in some ways, analogous to the approaching free-stream velocity in bluff bodies. The results of the calculation are listed in the right column of Table 3.2. The trend in Re_H with changes in velocity ratio are less important than what occurs at fixed velocity ratios between the unforced and relaminarized cases. The unforced, unstable jet shear layer Reynolds numbers are supercritical. However, Re_H is not reduced when the jet flow is relaminarized, but stays in the same supercritical range as the corresponding unstable cases. Therefore, suppression of the jet shear layer instabilities does not coincide with a reduction in the global Reynolds numbers of the jet shear layer from supercritical to a subcritical values. Instead, the stability properties of the flow appear to be connected to changes in the local stability properties of the jet shear layer profiles in the region where the jet shear layer initially develops.

3.6.5 Base Bleed

A well-known method for the suppression of nominally two-dimensional bluff body instabilities is to continuously inject fluid at the base directly into the wake region. The method, commonly termed "base bleed," was initially studied because of its potential value for drag reduction (Wood, 1964, 1967), but has once again risen in prominence as a tool for fundamental studies (Schumm et al., 1994). The base bleed mechanism is well understood for two dimensional bluff bodies (Monkewitz, 1988). In an unstable wake flow, the near wake time-averaged velocity profile is subjected to flow reversal and is governed by a local absolute instability which acts as a resonator to external disturbances. The wake then changes to convective instability amplifying the initial disturbance as the wake flow evolves downstream and the velocity deficit diffuses away. The connection between base bleed suppression and the stability properties of the wake is that the local absolute instability in the near wake is reduced by eliminating reverse flow. Therefore, base bleed suppresses the local absolute instability at some supercritical global Reynolds number inhibiting the global instability and the initiation of Kármán vortex shedding.

It was recognized that there are striking similarities between base bleed and the relaminarization phenomenon in that both control methods appear to suppress free stream instabilities by modifying the initial growth of the spatially developing flow profile. As a comparison to the synthetic jet relaminarization, base bleed control was applied to the low momentum elevated

JICF to test the method's effectiveness of suppressing the jet shear layer instability. Minimal changes to the apparatus were necessary to accommodate the blase bleed technique since steady upward-directed annular blowing could be introduced from the same slit used to generate the synthetic jet. To facilitate a comparison between the control methods both the average synthetic jet velocity, W_{sj}, and the bleed velocity, W_b, were determined by a mean centreline velocity taken two slit diameters from the stack exit ($z/D = 2$). It is the volume flux which is important in these measurements. Therefore the centreline velocities were corrected for assumed profiles, in this case a top-hat profile for the synthetic jet and a 2/3 correction factor to account for the fully developed base bleed flow profile emerging from the annular slit.

Figure 3.17 shows jet-seeded photographs comparing the unforced JICF in case CA with 60Hz synthetic jet forcing (case CB) and base bleed control. The test is at the lower limit of the tested velocity ratios ($R = 0.61$), therefore, relatively large synthetic jet amplitudes were required for instability suppression. The high amplitude forcing is apparent in Figure 3.17(b) since large 60 Hz ridges in the jet shear layer are clearly visible, however, the synthetic jet is still effective in suppressing the jet shear layer instability in the unforced JICF. The effect of base bleed is shown in Figure 3.17(c). Complete suppression of the jet shear layer instability is possible at a bleed velocity of $W_b = 0.95$ m/s. The most striking feature when comparing photographs (b) and (c) is the lack of pulsation in the JICF with steady blowing. At these JICF operating parameters it appears that base bleed is a more effective suppression method, but it should be noted that the bleed velocity is approximately four times higher than the measured average synthetic jet velocity.

To extend the comparison over all the test cases a non-dimensional bleed coefficient (Wood, 1964) is defined in terms of the synthetic jet velocity W_{sj} or bleed velocity W_b, and the average peak velocity of the profile U_p by

$$C_{sj} = \frac{W_{sj}h}{U_pH} \tag{3.9}$$

$$C_b = \frac{W_bh}{U_pH} \tag{3.10}$$

The average peak velocities of the wake profiles U_p were determined from ICV measurements along a line perpendicular to $s/D = 0.08$ which for all cases intersects a region close to $z/h = 2$. Consequently, there is likely some

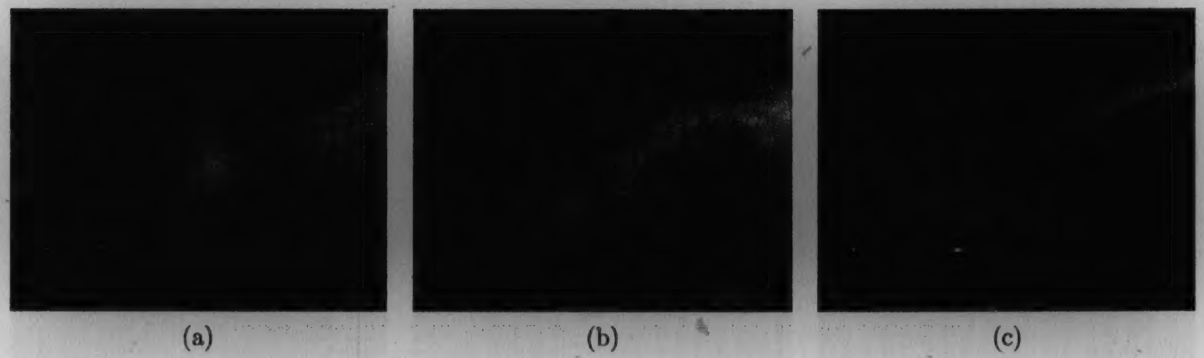

Figure 3.17: A comparison of synthetic jet and based bleed suppression of the jet shear layer instability, (a) the unforced JICF. Case CA, $R = 0.61$, $\mathrm{Re}_\infty = 2235$, (b) case CB, 60Hz synthetic jet forcing, $W_{sj} = 0.25$ m/s, (c) base bleed, $W_b = 0.95$ m/s.

Table 3.3: Summary of Critical Bleed Coefficients: Bleed coefficients at maximum suppression of the jet shear layer instability by synthetic jet forcing, C_{sj}, and base bleed, C_b. Case BB is not given because the synthetic jet velocity was too low to obtain an accurate reading. U_p is determined from profile measurements of the unforced JICF at $s/D = 0.08$ which intersects $z/h = 2$.

Case	C_{sj}	C_b
BA	0.133	–
CA	0.173	–
CB	–	0.048
DA	0.291	–
DB	–	0.109

error in the value of U_p related to the placement of the line. There is an additional error in C_b since U_p was determined from velocity profiles of the unforced case and not direct measurements of the profile under the influence of base bleed. The errors are likely not large considering that there is little change (a maximum of 5%) in U_p between the unforced and synthetic jet forced cases. In any case, the bleed coefficients should be considered only as approximate values computed to facilitate a loose comparison.

The results of the data reduction are listed in Table 3.3. The run letters correspond to the data used in calculation of the critical bleed coefficients. Base bleed coefficients tend to increase with decreasing velocity ratio which is similar to the trend in synthetic jet impulse measurements in Section 3.4.3. Therefore, more bleed momentum is required to stabilize the jet shear layer as the local Reynolds numbers of the unforced jet shear layer profile increase. The published bleed coefficients for synthetic jet forcing are much lower than the base bleed cases, which is a result of the lower synthetic jet velocities required for instability suppression (in case BB, W_{sj} was too low to get an accurate reading). It is unclear why more base bleed momentum is required to relaminarize the JICF flow, but the unsteadiness of the synthetic jet flow in the near field is likely to play a role. There is likely higher entrainment in the vicinity of the orifice in the synthetic jet case which is related to the periodic suction and ejection phases of the actuator.

Base bleed has a similar suppression effect a the synthetic jet on unstable JICFs in this R range, however, as was the case with synthetic jet forcing, base bleed suppression of the JICF instabilities does not occur above $R \simeq 1.13$.

3.7 Summary and Conclusions

The principle findings relate to the relaminarization phenomenon that occurs when a low momentum elevated JICF with laminar pipe flow is influenced by an annular synthetic jet created by low amplitude forcing. The phenomenon occurs over a wide parameter range of synthetic jet frequencies and velocity ratios below $R \simeq 1.13$. Whether or not the instability suppression occurs appears to be highly dependent on the natural stability properties of the jet shear layer. An investigation of the unforced low momentum elevated JICF found two regimes where there are unstable jet shear layers separated by a regime of stability at $R = 1.13 \pm 0.09$. The jet shear layer vortex structures and their behaviour appear to have different properties in both unstable regimes. It is only in the lower velocity ratio unsteady regime ($R < 1.13$) where the synthetic jet stabilizes the jet shear layer. The JICF control used here is fundamentally different from other studies (M'Closkey et al., 2002; Johari et al., 1999; Eroglu and Breidenthal, 2001) since forcing is introduced at the base of the jet shear layer from a temporally synthesized synthetic jet flow rather than by pulsation of the entire jet flow profile.

The occurrence of the relaminarization phenomenon is insensitive to the applied synthetic jet frequencies. It is the addition of synthetic jet momentum rather than the frequency of excitation which drives the suppression effect. Velocity field measurements show that the synthetic jet's influence on the time-averaged jet shear layer profile is most pronounced in a localized region near to the stack exit plane. The synthetic jet modifies the local jet shear layer profile inhibiting growth of instabilities by driving down the local Reynolds number of the jet shear layer in the near field.

Our measurements indicate that there isn't a single value for the critical local Reynolds number, but a range of values $100 \lesssim \mathrm{Re}_{\delta,\mathrm{crit}} \lesssim 600$ where relaminarization occurs. $\mathrm{Re}_{\delta,\mathrm{crit}}$ appears to drop monotonically with decreasing velocity ratio. The lowering of the local Reynolds number corresponds with an increase in forcing amplitude. With decreasing velocity ratio, increasing synthetic jet amplitude is required for forced suppression of the instabilities.

Therefore, lower Reynolds numbers could be required to damp out larger velocity fluctuations at the annulus due to the higher forcing amplitudes.

The suppression of the instability only occurs in the near field. As is the case with all open flows, the relaminarized JICF will eventually transition to turbulence as the flow convects downstream. Therefore the synthetic jet may inhibit instabilities in the JICF in the near field, but it only delays the flow's eventual transition to turbulence.

Our data is complementary to what is now a growing body of evidence of the presence of a local absolute instability close to the stack exit plane that defines the global characteristics of the elevated JICF at these low velocity ratios, in this case $R < 1.13$. Megerian et al. (2006) was the first to suggest this mechanism from their spectral measurements – that there is a transition in the nature of the jet shear layer instabilities from what is likely a convectively unstable flow at higher velocity ratios to a self-excited, globally unstable flow at these lower velocity ratios. Our visualizations of the natural JICF structure in Section 3.3 and our results in Section 3.6 provide additional support for their hypothesis, however the results do not provide conclusive evidence that such a transition occurs.

Features of the time-averaged unstable upstream jet shear layer profile do indeed have similarities to other flows undergoing absolute instabilities. The velocity deficit in the wake-like profile at $s/D = 0.1$, which dominates the profile with decreasing R, and the time-averaged leading separation bubble observed in the time-averaged vector fields are indications that a negative flow, or counter-flow, could exist in the vicinity of the stack exit. Such features are also present in bluff-body flows which are known to undergo local absolute instabilities in the near wake region (Huerre and Monkewitz, 1990).

The JICF's response to forcing provides further evidence that an absolutely unstable flow may exist at these low velocity ratios. Low amplitude synthetic jet forcing has a globally stabilizing effect on the supercritical JICF even though its influence appears to be most pronounced only in a localized area close to the stack exit plane. The synthetic jet's effect has similarities to the well understood base bleed control method which suppresses local absolute instabilities in bluff body flows. Base bleed was tried on this geometry and was found to have a similar stabilizing effect on the JICF jet shear layer. Regardless of the control method's practical applications, the bleed method demonstrated here is also a viable control mechanism to impulsively switch between stable and unstable flow structures for further fundamental exploration of the initial growth of the instabilities.

It is interesting that the three-dimensional jet shear layer exhibits many stability properties that are similar to wake flows that are primarily two-dimensional. More work is needed to understand the stability properties of this complex three-dimensional flow, but Reynolds numbers are highest along the plane of symmetry which we focused on here. Therefore, this location may have a controlling influence on the transitional properties of the flow.

BIBLIOGRAPHY

Andreopoulos, J. (1989). Wind tunnel experiments on cooling tower plumes. I. in uniform crossflow. *Transactions of the ASME. Journal of Heat Transfer*, 111(4):941–8.

Apps, C. P. (2001). Study of synthetic fence jets using image correlation velocimetry. Master's thesis, Department of Mechanical Engineering, University of Alberta.

Apps, C. P., Chen, T., and Sigurdson, L. (2003). Image correlation velocimetry applied to discrete smoke-wire streaklines in turbulent pipe flow. *Experiments in Fluids*, 35:288–90.

Broadwell, J. E. and Breidenthal, R. E. (1984). Structure and mixing of a transverse jet in incompressible flow. *Journal of Fluid Mechanics*, 148:405–12.

Chapple, D. (1998). The role of turbulence in pulsation induced orifice plate flow metering error. Master's thesis, Department of Mechanical Engineering, University of Alberta.

Corke, T., Koga, D., Drubka, R., and Nagib, H. (1977). A new technique for introducing controlled sheets of smoke streaklines in wind tunnels. *ICIASF 1977 Record IEEE Publication*, pages 74–80.

Crow, S. C. and Champagne, F. H. (1971). Orderly structure in jet turbulence. *Journal of Fluid Mechanics*, 48(3):547–91.

Diep, J. and Sigurdson, L. (2001). Cross-jet influenced by a concentric synthetic jet. *Physics of Fluids*, 13(9):S16.

Diep, J. and Sigurdson, L. (2002). *Low velocity ratio transverse jets influenced by concentric synthetic jets*. Manipulation and Control of Jets in Crossflow, CISM Courses and Lectures No. 439. International Centre for Mechanical Sciences.

Eiff, O. S., Kawall, J. G., and Keffer, J. F. (1995). Lock-in of vortices in the wake of an elevated round turbulent jet in a crossflow. *Experiments in Fluids*, 19(3):203–13.

Eiff, O. S. and Keffer, J. F. (1997). On the structures in the near-wake region of an elevated turbulent jet in a crossflow. *Journal of Fluid Mechanics*, 333:161–95.

Eroglu, A. and Breidenthal, R. E. (2001). Structure, penetration, and mixing of pulsed jets in crossflow. *AIAA Journal*, 39(3):417–23.

Fric, T. F. and Roshko, A. (1994). Vortical structure in the wake of a transverse jet. *Journal of Fluid Mechanics*, 279:1–47.

Gharib, M., Rambod, E., and Shariff, K. (1998). A universal time scale for vortex ring formation. *Journal of Fluid Mechanics*, 360:121–40.

Haniu, H. and Ramaprian, B. R. (1989). Studies on two-dimensional curved nonbuoyant jets in cross flow. *Journal of Fluids Engineering, Transactions of the ASME*, 111(1):78–86.

Hart, D. P. (2000). PIV error correction. *Experiments in Fluids*, 29(1):13–22.

Haven, J. P. and Kurosaka, M. (1996). Improved Jet Coverage Through Vortex Cancellation. *AIAA Journal*, 34(11):2443–4.

Holman, R., Utturkar, Y., Mittal, R., Smith, B. L., and Cattafesta, L. (2005). Formation criterion for synthetic jets. *AIAA Journal*, 43(10):2110–16.

Huang, R. F. and Lan, J. (2005). Characteristic modes and evolution processes of shear-layer vortices in an elevated transverse jet. *Physics of Fluids*, 17(3):034103.

Huerre, P. and Monkewitz, P. A. (1990). Local and global instabilities in spacially developing flows. *Annual Review of Fluid Mechnaics*, 22:473–537.

Johari, H. (2006). Scaling of Fully Pulsed Jets in Crossflow. *AIAA Journal*, 44(11):2719–25.

Johari, H., Pacheco-Tougas, M., and Hermanson, J. C. (1999). Penetration and mixing of fully modulated turbulent jets in crossflow. *AIAA Journal*, 37(7):842–50.

Johnson, M. R. and Kostiuk, L. W. (2000). Efficiencies of low-momentum jet diffusion flames in crosswinds. *Combustion and Flame*, 123(1):189–200.

Kamotani, Y. and Greber, I. (1972). Experiments on a turbulent jet in a cross flow. *AIAA Journal*, 10(11):1425–29.

Kelso, R. M., Lim, T. T., and Perry, A. E. (1996). An experimental study of round jets in cross-flow. *Journal of Fluid Mechanics*, 306:111–44.

Koch, W. (1985). Local instability characteristics and frequency determination of self-excited wake flows. *Journal of Sound and Vibration*, 99:53–83.

M'Closkey, R. T., King, J. M., Cortelezzi, L., and Karagozian, A. R. (2002). The actively controlled jet in crossflow. *Journal of Fluid Mechanics*, 452:325–35.

Megerian, S., Davitian, J., de B. Alves, L. S., and Karagozian, A. R. (2006). Transverse jet shear layer instabilities - Part I: Experimental studies. to appear in the *Journal of Fluid Mechanics.*

Monkewitz, P. A. (1988). The absolute and convective nature of instability in two-dimensional wakes at low Reynolds numbers. *Physics of Fluids*, 31(5):999–1006.

Moussa, Z. M., Trischka, J. W., and Eskinazi, S. (1977). The near field in the mixing of a round jet with a cross-stream. *Journal of Fluid Mechanics*, 80(1):49–80.

Papamoschou, D. and Bunyajitradulya, A. (1997). Evolution of large eddies in compressible shear layers. *Physics of Fluids*, 9(3):756–65.

Schumm, M., Berger, E., and Monkewitz, P. A. (1994). Self-excited oscillations in the wake of two-dimensional bluff bodies and their control. *Journal of Fluid Mechanics*, 271:17–53.

Shapiro, S. R., King, J. M., M'Closkey, R. T., and Karagozian, A. R. (2006). Optimization of controlled jets in crossflow. *AIAA Journal*, 44:1292–8.

Sherlock, R. H. and Stalker, E. A. (1941). A study of flow phenomena in the wake of smokestacks. *Engineering Research Bulletin No. 29, University of Michigan, Ann Arbor, MI. 49 pp.*

Sigurdson, L. and Apps, C. (2003). Image Correlation Velocimetry Applied to Diffuse Smoke in a Turbulent Jet. Proceedings of the 19th Canadian Congress of Applied Mechanics.

Smith, B. L. and Glezer, A. (1998). The formation and evolution of synthetic jets. *Physics of Fluids*, 10(9):2281–97.

Smith, S. H. and Mungal, M. G. (1998). Mixing, structure and scaling of the jet in crossflow. *Journal of Fluid Mechanics*, 357:83–122.

Watson, G. and Sigurdson, L. (2006). Relaminarization of the vortex structure in a low velocity ratio jet-in-crossflow. *Bulletin of the American Physical Society*, 51(9):124–5.

Watson, G. and Sigurdson, L. (2007). Suppression of jet shear layer instabilities in a low momentum elevated jet-in-crossflow. Proceedings of the 21st Canadian Congress of Applied Mechanics, pages 271–72, Toronto, ON.

Wood, C. J. (1964). Effect of base bleed on periodic wake. *Royal Aeronautical Society – Journal*, 68(64):477–82.

Wood, C. J. (1967). Visualization of incompressible wake with base bleed. *Journal of Fluid Mechanics*, 29:259–72.

CHAPTER 4

DIGITIZATION OF JET-IN-CROSSFLOW JET SHEAR LAYER VORTEX STRUCTURE VIA AUGMENTED REALITY[1]

4.1 Acknowledgements for Chapter 4

This work is the sum of a group effort. The results presented in this chapter were obtained from a measurement system developed in-house. Thanks to Josh Nault for development of the stereoscopic image capture system and to Bernie Faulkner for building it. Also to Christopher Strand, Graeme Watson and Ryan Tucker for writing the critical elements of the stereo data analysis software. Chris Ausford also made notable contributions in testing and system validation. Finally, thanks to Dr Lorenz Sigurdson for devising the experimental technique and guiding all stages of the project.

4.2 Introduction

In turbulent flows there is often an orderly and readily identifiable large-scale structure that exists within the apparent chaos (Roshko, 1976). The structures are essentially composed of filaments of vorticity which form coherent regions of vorticity. As the vorticity evolve downstream it interacts with one another in an evolving three-dimensional vortex flow. Since the discovery of the phenomenon by Roshko (1976) there has been an explosion of work in the area of mapping the large-scale structures in turbulence. The maps are best displayed as vortex skeleton models which represent the vortex tubes in the large-scale structure. There are numerous examples of skeleton models in the literature; some are the Bernal-Roshko vortices in shear layers (Bernal and Roshko, 1986), the inter-linked vortices in co-flowing jets (Perry and Lim, 1978), the numerous vortex structures in jets-in-crossflow (Fric and Roshko, 1994; Eiff and Keffer, 1997; Kelso et al., 1996; Cortelezzi and Karagozian, 2001), the staggered arrangement of hairpin loops in separation bubbles (Sigurdson and Roshko, 1984; Sigurdson, 1986), and the vortex ring models for impacting water droplets (Peck and Sigurdson, 1994). By modeling the turbulence as the creation, evolution, interaction and decay of vortices scientists have gained greater insight into the flow physics and the gross characteristics turbulent flows.

---

[1] Part of the results in this chapter were presented in poster entitled "3-D Digitization of Stereoscopic Jet-in-Crossflow Images," by Watson, G., Strand, C., Nault, J., Tucker, R., and Sigurdson, L., at the Annual Meeting of the Fluid Dynamics Division of the American Physical Society, Tampa, FL., Nov. 2006.

Recently, there has some success in determining the large-scale structure of jets-in-crossflow (JICFs). JICFs are important due to their practical significance in a wide range of applications. They are typically formed from two geometries whereby the jet flow emits into the crossflow either from a pipe which is flush with a wall, inside the wall boundary layer, or from an elevated position though a stack. The JICF's flow behaviour is actually the result of an interaction of many systems of vortices, a review of the structures can be found in the introduction of Huang and Lan (2005). We will focus on the JICF's jet shear layer vortices as many aspects of these vortices' near field formation and evolution remain poorly understood. A skeleton model for the jet shear layer vortices has been proposed for the wall-issued case (Kelso et al., 1996). However, a recent survey of the elevated case by Huang and Lan (2005) shows that the jet shear layer vortices have a structure and behaviour which are quite different from their wall-issued counterparts. A visualization method that takes into account the three-dimensional nature of the jet shear layer vortices must be used to propose a model to explain the vortices' behaviour.

Flow visualization has proven to be a useful tool for determining the nature of the large-scale structures in many flow geometries. It is a straight forward method of obtaining field measurements of the vortex structures. The general methodology is to inject a tracer, which is typically smoke or dye, into a location where there is creation of vorticity. The tracer then follows the path of the vorticity as the flow evolves. The photographs are usually obtained with back lighting or a columnated strobe. It is currently standard practise to process the visualizations as two-dimensional photographs, therefore depth information is lost in the visualization. Also, care must be taken when interpreting the two-dimensional photographs because the optical integration along the line of sight distorts the three-dimensional structures. Therefore, multiple two-dimensional views from different angles are often required to visualize the large-scale structure, however even with this information the spatial nature of the vorticity field can usually only be inferred from the visualizations.

Three-dimensional imaging techniques overcome problems with spatial distortion by preserving a perceived three-dimensionality of the flow volume. Techniques to image large-scale structures in three dimensions are not new. Stereo imaging is a promising method that provides volumetric information of the flow structure. The method is an extension of the concept of human binocular vision, whereby a region of the flow is viewed from two, left and right perspectives which are separated by some distance. Usually two still or video cameras are triggered together to obtain *instantaneous* photographs of the visible components of the large-scale structure in the flow volume. The images are then post-processed and displayed as stereoscopic photographs. The method has been used with considerable success in elucidating qualitative information about the large-scale structure in turbulent boundary layers (Praturi and Brodkey, 1978). This paper presents an extension of the stereoscopic method to extract quantitative spatial information. Another technique involves the use of laser sheets to slice the flow volume into a series of cross-sectional images. The stack of cross-sections are then reconstructed later to generate a three-dimensional image of the flow volume. Early implementations of this technique used single scan laser sheets and, therefore could only be applied to flows that were highly periodic in nature (Perry and Lim, 1978). For intermittent flows, apparatuses have been developed which are capable of taking multiple sectional planes at different spatial locations (Delo et al., 2004). However, both implementations of the slicing method are only, at best, capable of obtaining quasi-instantaneous images of the flow volume which brings about errors in the three-dimensional reconstruction.

The difficulties occur when attempting to extract spatial information from stereoscopic photographs of the turbulent flow field. To determine depth information, a one-to-one matching or correlation of the left and right images is necessary. A possible solution is to employ an automatic image correlation algorithm to calculate the three-dimensionality of the flow volume. Such an approach has been attempted to some degree of success by Cheung and Zhang (2006) to study three-dimensional flame structures. However, the semi-transparent nature of the flow field does present the computer algorithm with difficulties as there were a significant number of correlation errors in Cheung and Zhang's data extractions. We propose to transcend these difficulties by using the human brain to naturally perform the difficult computation. The brain has an astonishing capacity to first calculate, then present to the observer a complex turbulent smoke volume. A technique has been developed whereby a virtual cursor is introduced into the stereoscopic photograph which creates an "Augmented Reality." The perceived position of the cursor in the three-dimensional field can be precisely controlled by the observer and can be brought near the characteristic vortex structures in order to digitally estimate the spatial coordinates of the features. With this information the observer is able to construct a three-dimensional vortex skeleton model of the large-scale structure.

Augmented Realities are a class of displays which creates a human interface that combines the real world with computer rendered images (Milgram et al., 1994). In this case the "real world" are the stereoscopic flow visualizations. The technique is thought to be ideal for use in applications which require humans to interact with objects in hard to reach places. It has been shown that Augmented Reality has the potential to be useful in telepresence (Lawson et al., 2002) and in surgical applications (Kim et al., 2000) for tasks that require remote three-dimensional measurements. We wished to extend the technique for use in the fluid mechanics field as a tool to extract quantitative spatial information of the three-dimensional elevated JICF jet-shear layer vortex structure.

4.3 Experimental Setup

The apparatus and method will only be discussed briefly here. For more information please consult Strand et al. (2007).

4.3.1 JICF Apparatus

The apparatus was essentially the one used in Diep (2001). The elevated JICF apparatus consisted of a 25.4 mm diameter, *D*, "stack" inserted half way into a 30.5 cm by 30.5 cm wind tunnel test section with a crossflow turbulence intensity of 0.6%. The crossflow is from left to right in all photographs. The jet flow issued into the cross-stream through a central tube aligned with the stack centre which had an inside diameter, *d*, of 19.12 mm. The jet flow in the pipe was laminar with a fully developed parabolic profile at the stack exit in no crossflow. Surrounding the central tube was an annulus with an inner width, h of 1.64 mm through which a sinusoidal velocity fluctuation could be introduced, however, forcing was not used in these experiments.

4.3.2 Stereo Image Capture

The stereoscopic images were photographed with an image capture system developed by Joshua Nault (Nault, 2005). The image capture system consisted of two Nikon D1X cameras with 60 mm lenses mounted on camera supports that allow for pitch, roll and yaw corrections to ensure that the cameras were level. The cameras have excellent performance traits, however their size presented several challenges when designing the image capture system. Placing the cameras side-by-side was not a viable option due to the what would be the large separation distances between the cameras. Instead, a mirror assembly was designed to reduce the apparent separation distance between the cameras. Support for the cameras and mirror assembly was provided by an inverted 'T' shaped structure. The mounting heads and traverses allowed for fine adjustment of the imaging system's level and apparent separation distance. The apparatus' two cameras were connected to an in-house built timing box and strobe which allowed for precise control of exposure times and lighting.

The image pairs were converted to a red/blue anaglyph photograph before the analysis using StereoPhoto Maker, which is a freely available software tool developed by Masuji SUTO and David Sykes (Suto and Sykes, 2006).

4.3.3 Stereo Extraction Software

The stereo data extraction software was developed by Christopher Strand, Graeme Watson and Ryan Tucker (Sigurdson et al., 2006; Strand et al., 2007). The software is an Augmented Reality display which uses red/blue anaglyph rendering to allow for extraction of spatial information from the stereoscopic flow visualizations. The operator was immersed into the interface via the use of red/blue eye glasses. A three-dimensional cursor was rendered within the stereoscopic photograph. The cursor's perceived position in the stereoscopic perception could be controlled in real time by the observer and could be brought near the centres of the vortex tubes to digitally estimate the coordinates of the feature. The spatial coordinates could then be joined together to form a vortex tube model which consisted of three-dimensionally rendered lines that were super-imposed over the stereoscopic photograph. The spatial coordinates were also stored in data files for later use by other graphics systems for further data analysis.

4.4 Results and Discussion

Figure 4.1 shows a conventional two-dimensional side view photograph of the jet shear layer vortex structure. The vortices are visible by seeding the jet fluid with a semi-translucent glycerol and water based fog vapour. Smoke injected directly into vorticity bearing fluid, in this case into the jet flow's inner pipe boundary layer, will mark the progress of the jet flow's vorticity and the roll-up of vortices. However, the tracer can also reveal the formation of other vortices if the fluid that it marks is drawn into the vortices' cores. The jet and crossflow Reynolds numbers are 630 and 1200, based on the inner and outer stack diameters respectively. The jet-to-crossflow momentum ratio is 0.81, which is a ratio of the momentum fluxes of the two fluid streams.

Only a two-dimensional interpretation of the vorticity field is possible from this side view. For the low velocity ratio in this study, vorticity in the jet shear layer structure originates from the boundary layer of the jet flow inside the stack and from separated flow on the outside of the stack (Andreopoulos, 1989). A short time after leaving the stack surfaces, the initially uniform distribution of vorticity in the jet shear layer organizes itself into vortex tubes that, if viewed two-dimensionally, appear as a reoccurring "tri pole" vortex structure. The roll-up of these vortices is periodic. The tri pole structure appears to be the basic structural component which makes up the jet shear layer's large scale structure. It consists of mushroom vortices (two vortices of opposite rotation, also known as a dipole) which form periodically on the upstream side of the jet shear layer. The clockwise rotating vortices (labeled 'A') originate from the separated outer stack flow while the counter-clockwise rotating vortices (labeled 'B') are from the upstream jet flow boundary layer. Formation of the mushroom vortices occurs simultaneously and with the same frequency as the clockwise roll-up of vortices (labeled 'C') on the downstream jet flow boundary layer. Therefore, the tri pole consists of two vortices of the same sign and one vortex of opposite sign.

The large scale structure appears to have a complex evolution. For now, the discussion will again be restricted to a two-dimensional interpretation of the flow structure. In this case, the mushroom vortices' orientation appears to rotate clock-wise as they convect around the bend in the JICF. When the mushrooms evolve around the bend in the jet, their pointing direction is perpendicular to a line joining the mushrooms. They point downstream in the far-field, however they always have an upwards-biased pointing direction. "Pointing" is a term first used by Diep and Sigurdson (2002) to describe the direction that the mushrooms would self-propagate. The pointing direction is connected to the impulse of the pair. It has been shown that the direction of rotation and the pointing direction of the mushroom vortices is highly dependent on the jet-to-crossflow velocity ratio (Huang and Lan, 2005). The tri pole vortices form at a fixed frequency, however the wavelength of the vortices on the lee side are much smaller than the wavelength of the mushroom vortices. The vortex structure in the near field has been called a tri pole for convenience, in the sense that the initial formation of the three vortices in the structure occur at the same frequency. However, in the far field the vortices relative proximities to one another on either side of the JICF diverge due to their different wavelengths. In the far field it may be better to separately describe the evolution of the structures as the motion of dipoles on the upstream side and shear layer vortices on the downstream side. The two-dimensional view of the flow structure limits our ability to draw conclusions about the mechanisms responsible for these observations since the photographs do not give an accurate representation of the actual three-dimensional vortex structure. An understanding of the full three-dimensional structure of the flow is required to gain a better understanding of the flow behaviour.

A better understanding of the tri pole observed in the two-dimensional photographs can be obtained from stereoscopic photographs. Figure 4.2 shows the right and left close-up stereoscopic photographs of the formation and initial evolution of the jet-shear layer vortex structure. The flow field is viewed from a side position orthogonal to the cross-stream direction, and at an angle of 30 degrees above the stack exit plane. The three-dimensional image can be reconstructed with a stereoscopic viewer available from Berezin Stereo Photography Products or can be viewed without a viewer by focusing at a distance and placing the image in the line of sight. The side-by-side technique does require some practise to see the image in three dimensions. An alternative rendering of the stereoscpic pairs presented in this chapter have been included as red/blue anaglyphs at the end of the chapter (Figure 4.4 and 4.5). These images can be viewed with red/cyan or red/blue filtered eye glasses.

Initial roll-up of the vortices on the upstream and downstream sides of the jet column are visible less than a stack diameter from the exit plane, but the vortex tubes become more evident as the structure evolves. The laminar vortex tubes are visible in the photograph because the JICF Reynolds numbers are low enough so that the large-scale structures are not concealed by smaller scales. In the figure, some of the tubes have been traced with the virtual cursor (top right) as lines for superposition of a partial vortex skeleton model. Vorticity from the inner pipe boundary layer are shed into the flow as vortex rings. The rings are tilted and distorted into a saddle shape by the velocity gradient between the crossflow and the slower fluid in the wake of the jet and stack (Moussa et al., 1977). The formation and folding of the vortex ring is indeed consistent with the findings of Kelso et al. (1996) who modeled the jet shear layer structure as a collection of vortex rings in a wall-issued JICF.

The jet shear layer is also composed of vorticity from flow separated off the upstream outer stack wall. A vortex tube which consists of oppositely signed vorticity wrapped around the vortex ring is indeed evident in the photograph. However, further analysis of the tube's behaviour is not possible because the ends of the vortex tubes are lost below the stack exit plane. The failure to trace the ends of the tube has little to do with the data extraction method, but is related to the method used to tag the vorticity in the structure. The vortex tubes created on the outer stack wall are not initially tagged with smoke when they are created. Instead, the tracer convects into the cores as the tube evolves. In any case, the solenoidal condition of the vorticity vector requires that the vortex tubes not terminate in the flow, but must close on themselves, or end on a rotating solid, a free surface or at infinity (Saffman, 1995). We speculate that at this initial point in the vortices' evolution, the tubes may be connected in some way to vortex structures in the wake region behind the stack. The vortices in the wake region consist primarily of vorticity which originate in the same outer stack wall boundary layer as the vortex loop in the jet shear layer. We have no data to confirm this hypothesis, though a different method to tag the stack vorticity would likely resolve a connection between the vortex structures, if such a connection exists.

When the vortex tubes are traced, their spatial coordinates are calculated and stored by the data extraction software. Some of the spatial coordinates along the vortex loop are displayed in Figure 4.2. The coordinates are normalized by stack diameter. The coordinates of the lines can also be readily obtained for display in other graphics systems to allow complete exploration from any perspective. Figure 4.3 shows a rendering of the extracted partial skeleton model. The pipe and Cartesian coordinate system are also rendered to provide a visual reference of the size and orientation of the skeleton model. From this vantage point the stereoscopic visualization method was only able to capture one side of the vortex tube structure because the smoke obscures the other side from view. In this flow this is not a problem because the vortex structure is symmetrical along the JICF (z, x) centre plane at $y = 0$. However, in non-symmetrical flow patterns the visualization method would be incapable of instantaneously viewing the entire flow structure. In these cases, it may be better to use the slicing approach of Delo et al. (2004).

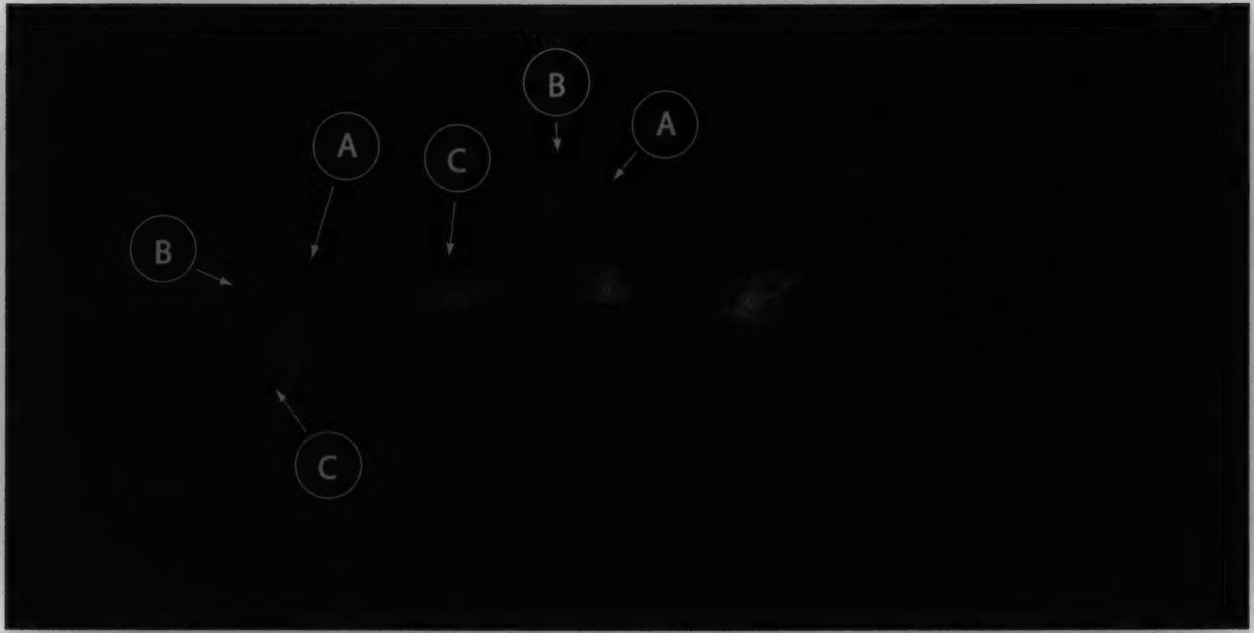

Figure 4.1: Two-dimensional side view photograph of the JICF jet shear layer vortex structure. $\mathrm{Re}_\infty = 1200$, $\mathrm{Re}_d = 630$ and $R = 0.81$. Crossflow and jet Reynolds numbers are based on the outer stack diameter, D, and inner pipe diameter, d, respectively. The labels 'A', 'B' and 'C' are the three vortices that make up the repeating tri pole vortex arrangement.

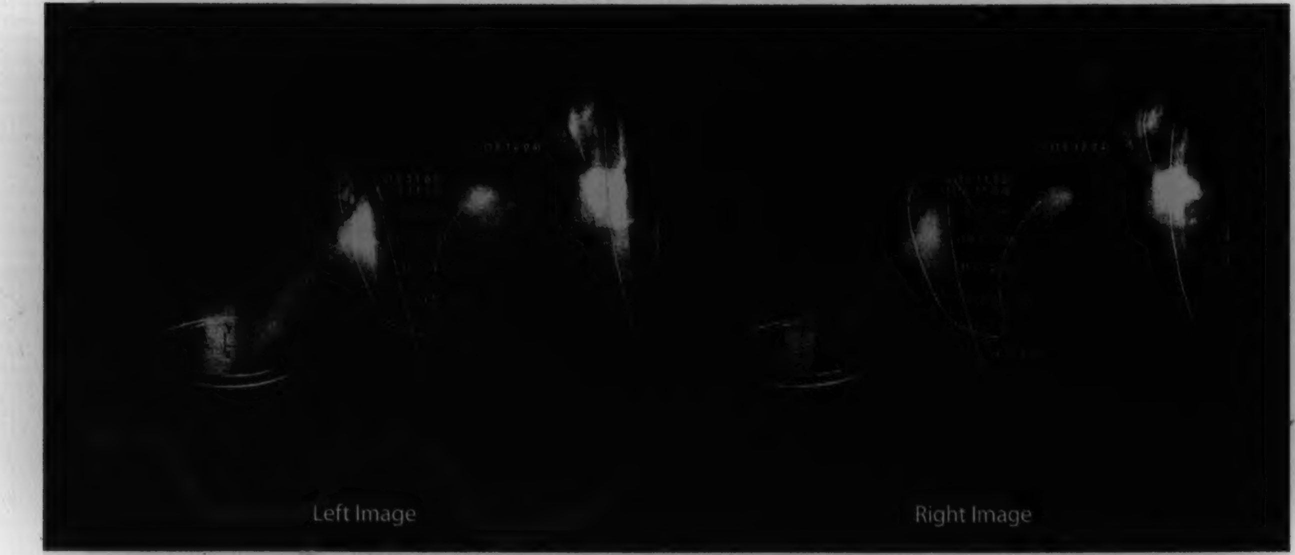

Figure 4.2: Stereoscopic visualization of the near field of the turbulent JICF plume. The image can be constructed using a stereoscopic viewer. A vortex skeleton model of the jet shear layer vortex tubes is drawn over the stereo photograph with a virtual cursor (top right). The spatial coordinates of one of the lines has also been displayed.

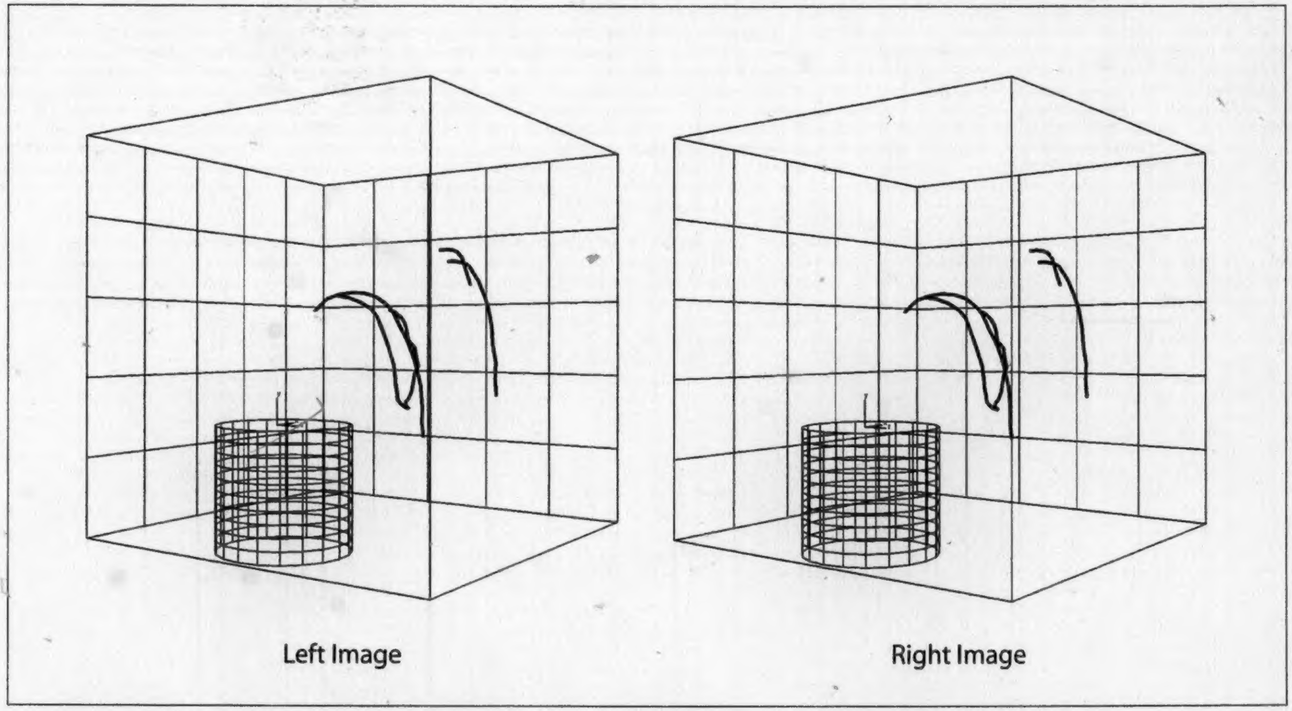

Left Image

Right Image

Figure 4.3: Stereoscopic rendering of the vortex skeleton model of the jet shear layer vortex structure can be rotated and viewed from any angle. The pipe and Cartesian coordinate system provide a visual reference of the size and orientation of the skeleton model.

4.5 Conclusions

Stereo imaging and analysis have been carried out to determine the near field formation of the elevated JICF jet shear layer vortices. The Augmented Reality interface allowed for the determination of spatial coordinates and the extraction of a spatially accurate three-dimensional vortex skeleton model. The basic constituents of the large-scale jet shear layer structure appear to be a periodic arrangement of vortices which originate from the jet column and from separated flow on the leading edge of the outer stack wall. In two-dimensional views the vortices are observed to occur periodically in a tri pole arrangement. However, the actual three-dimensional structure consists of a vortex ring shed from the jet column surrounded by a vortex loop of outer stack vorticity. The structure is symmetrical on both sides of the JICF centre plane. The vortex rings have an evolution in the near field which is similar to the model proposed by Kelso et al. (1996) for ground-level JICF. The vortex loop, however, is a unique structure in the elevated case. The ends of the vortex loop are lost below the area marked by the smoke tracer so it is unclear how the vortex loops connect with the overall JICF structure. The augmented reality technique is, of course, limited by the ability of the tracer method's ability to track the vorticity, as is the case with all visualization methods.

The proposed model shows the initial configuration of the vortices, but does not address their evolution in the far field. Cancellation, pinch-off and reconnection could definitely occur as the vortices interact and the structure evolves. In Figure 4.2, the vortex tubes appear to be stretched as they evolve downstream. The vortex loop is in close proximity to the ring that consists of a tube of oppositely signed, counter rotating vorticity. The photograph and the extracted partial model suggest that the vorticity in these structures may pinch off and reconnect to form mini saddle shaped rings on the upstream side of the jet shear layer. This possibility is presently under investigation, however a model for the evolution of the elevated jet shear layer vortices will have to account for the initial configuration of the three-dimensional structure displayed here.

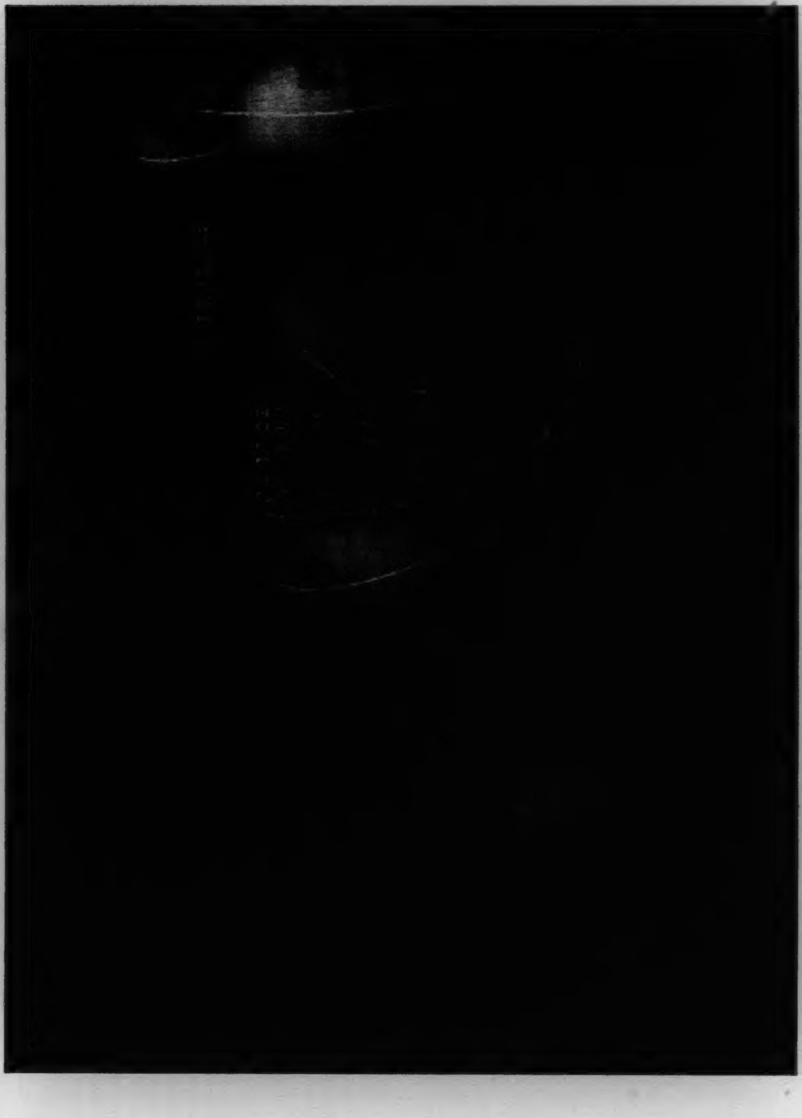

Figure 4.4: An alternative photograph of the near field of the turbulent JICF plume displayed in a red/cyan anaglyph. The anaglyph can be constructed using red/cyan eye glasses.

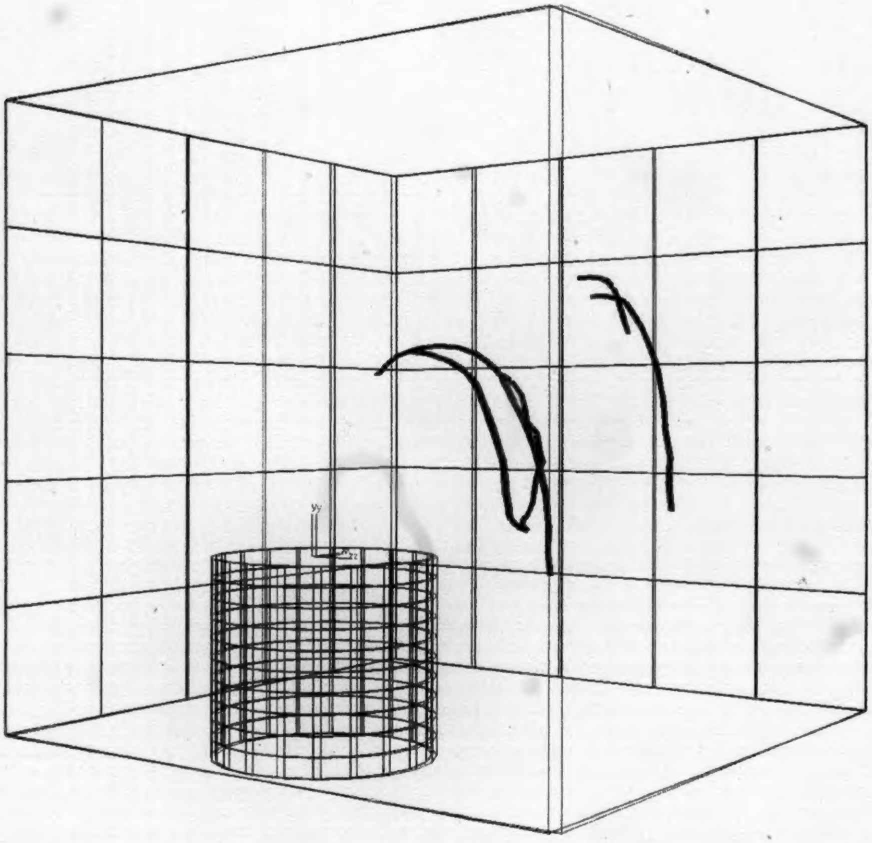

Figure 4.5: An alternative rendering of the vortex skeleton model of the jet shear layer vortex structure displayed in a red/cyan anaglyph.

BIBLIOGRAPHY

Andreopoulos, J. (1989). Wind tunnel experiments on cooling tower plumes. I. in uniform crossflow. *Transactions of the ASME. Journal of Heat Transfer*, 111(4):941–8.

Bernal, L. P. and Roshko, A. (1986). Streamwise vortex structure in plane mixing layers. *Journal of Fluid Mechanics*, 170:499–25.

Cheung, K. Y. and Zhang, Y. (2006). Stereo imaging and analysis of combustion process in a gas turbine combustor. *Measurement Science & Technology*, 17:3221–28.

Cortelezzi, L. and Karagozian, A. R. (2001). On the formation of the counter-rotating vortex pair in transverse jets. *Journal of Fluid Mechanics*, 446:347–73.

Delo, C. J., Kelso, R. M., and Smits, A. J. (2004). Three-dimensional structure of a low-Reynolds-number turbulent boundary layer. *Journal of Fluid Mechanics*, 512:47–83.

Diep, J. (2001). Flow Control Reduction of Smokestack Downwash. Master's thesis, Department of Mechanical Engineering, University of Alberta.

Diep, J. and Sigurdson, L. (2002). *Low velocity ratio transverse jets influenced by concentric synthetic jets.* Manipulation and Control of Jets in Crossflow, CISM Courses and Lectures No. 439. International Centre for Mechanical Sciences.

Eiff, O. S. and Keffer, J. F. (1997). On the structures in the near-wake region of an elevated turbulent jet in a crossflow. *Journal of Fluid Mechanics*, 333:161–95.

Fric, T. F. and Roshko, A. (1994). Vortical structure in the wake of a transverse jet. *Journal of Fluid Mechanics*, 279:1–47.

Huang, R. F. and Lan, J. (2005). Characteristic modes and evolution processes of shear-layer vortices in an elevated transverse jet. *Physics of Fluids*, 17(3):034103.

Kelso, R. M., Lim, T. T., and Perry, A. E. (1996). An experimental study of round jets in cross-flow. *Journal of Fluid Mechanics*, 306:111–44.

Kim, M. Y., Drake, J. M., and Milgram, P. (2000). Virtual Tape Measure for the Operating Microscope: System Specifications and Performance Evaluation. *Computer Aided Surgery*, 5:148–55.

Lawson, S. W., Pretlove, J. R., Wheeler, A. C., and Parker, G. A. (2002). Augmented Reality as a Tool to Aid the Telerobotic Exploration and Characterization of Remote Environments. *Presence: Teleoperators and Virtual Environments*, 11(4):352–67.

Milgram, P., Takemura, H., Utsumi, A., and Kishino, F. (1994). Augmented reality: a class of displays on the reality-virtuality continuum. In *Proceedings of SPIE Telemanipulator and Telepresence Technologies*, volume 2351, Boston, MA.

Nault, J. (2005). Stereoscopic Visualization of Flows. Technical report, Department of Mechanical Engineering, University of Alberta.

Peck, B. and Sigurdson, L. (1994). The three-dimensional vortex structure of an impacting water drop. *Physics of Fluids*, (2):564–76.

Perry, A. E. and Lim, T. T. (1978). Coherent structures in coflowing jets and wakes. *Journal of Fluid Mechanics*, 88(3):451–63.

Praturi, A. K. and Brodkey, R. S. (1978). Stereoscopic visual study of coherent structures in turbulent shear flow. *Journal of Fluid Mechanics*, 89(2):251–72.

Roshko, A. (1976). Structure of turbulent shear flows: a new look. *AIAA Journal*, 14(10):1349–57.

Sigurdson, L., Strand, C., Watson, G., Nault, J., and Tucker, R. (2006). 3-D Digitization of Stereoscopic Jet-in-Crossflow Vortex Structure Images via Augmented Reality. *Bulletin of the American Physical Society*, 51(9):37.

Sigurdson, L. W. (1986). *The structure and control of a turbulent reattaching flow.* PhD thesis, Aeronautics Department of California Institute of Technology.

Sigurdson, L. W. and Roshko, A. (1984). The large-scale structure of a turbulent reattaching flow. *Bulletin of the American Physical Society*, 29(9):1542.

Strand, C., Watson, G., Nault, J., Tucker, R., Ausford, C., and Sigurdson, L. (2007). An Augmented Reality 3-D digitization system for stereoscopic flow visualization images. In preparation for submission to the *Journal of Visualization.*

Suto, M. and Sykes, D. (2006). Stereophoto Maker Version 3.10. http://stereo.jpn.org/eng/stphmkr/.

CHAPTER 5

SUMMARY AND CONCLUSIONS

The three manuscripts in this thesis presented experimental investigations related to the structure and control of low momentum elevated jets-in-crosssflow (JICF). The objectives of the manuscripts fall into two categories: the determination of the formation and evolution of jet shear layer coherent structures in the forced and unforced JICF (Chapter 2 and Chapter 4, respectively), and a study of the control of the elevated JICF jet shear layer instabilities (Chapter 3). The manuscripts complement each other in the sense that they strengthen a fundamental understanding of this complex class of flows in a regime that has received little attention from researchers. The contributions to the JICF field are summarized below.

5.1 Formation and Evolution of the JICF Vortices

The chapter "Formation and evolution of low momentum elevated jet-in-crossflow vortices" surveyed the wide variety of vortex phenomena that occurs in the low momentum elevated JICF jet shear layer. For this geometry, strikingly different behaviours were observed in the unforced and forced jet shear layers above and below $R = 1.13 \pm 0.09$. The low momentum elevated JICFs are best classified by splitting the operating parameters into "low R" ($R < 1.13$) and "high R" regimes ($1.13 < R < 1.5$). Alternately seeding the jet flow and crossflow was important for correct interpretation of the vortex structures.

The unforced jet shear layer vortices' structure and evolution were similar to those presented in Huang and Lan (2005) in the low and high R regimes. In the low R regime, the structures are highly three-dimensional, but if the jet shear layer vortices are viewed perpendicularly to the plane of symmetry they appear to be arranged in a tri pole arrangement consisting of jet vorticity and vorticity from the outer stack wall.

The visualization techniques employed in this experiment were especially useful in the low R regime. Interesting similarities to the mode switching in the unforced vortex structure found by Huang and Lan (2005) have been noted, however further work is necessary to fully understand the natures of these complex vortex arrangements. The visualizations also strengthen the interpretations of Diep and Sigurdson (2002) relating to the mushroom vortices in the "pointing" transition. The visualizations strengthened our understanding of the synthetic jet's role in the formation and evolution of vortices in the forced jet shear layer. As the forcing amplitude increases, the vortices that are ejected from the annulus appear to become stronger and entrain fluid more quickly. These vortices become the mushroom structures visible on the upstream side of the jet shear layer.

The behaviour of the jet shear layer vortices is much different in the high R regime. The structure of the jet shear layer vortices are not changed unless the jet is forced near to the frequency associated with the unforced jet shear layer roll-up. This behaviour is similar to what has been reported by Kelso et al. (1996) and Megerian et al. (2006). Relaminarization of the jet shear layer does not occur, however there appears to be some increase in mixing in the JICF at higher synthetic jet forcing amplitudes. However in this regime, relatively little change in the vortex structure, jet penetration or spread is attained though this method of forcing.

5.2 Relaminarization of the Elevated JICF

The second manuscript "Suppression of jet shear layer instabilities in a low momentum elevated jet-in-crossflow" presented an experimental investigation into an instability suppression phenomenon first observed by Diep and Sigurdson (2001). An initially unstable low momentum elevated JICF can be made steady and completely relaminarized in its near field when it is forced by a low amplitude synthetic jet coaxial to the jet flow. The reasons for instability suppression have not been addressed in previous JICF control literature. Measurements of the flow field characterized the phenomenon and a mechanism was proposed to explain the flow's behaviour.

For this particular JICF geometry and Reynolds number range, $1200 \leq \mathrm{Re}_\infty \lesssim 2200$, forced suppression of the jet shear layer instabilities occurs within a regime of initially unstable JICFs bounded by a well defined, finite range of velocity ratios, $R < 1.13$. The relaminarization phenomenon does not occur above this velocity ratio range. An interesting transformation in the unforced jet shear layer vortex structure at $R = 1.13 \pm 0.09$ occurs at the exact velocity ratio at which the relaminarization phenomenon no longer occurs. This may not be coincidental, but rather may be evidence that supports the hypothesis of Megerian et al. (2006), that there is a transition in the jet shear layer to a new type of instability that responds differently to methods of control. We thank Dr. Anne Karagozian and her team for kindly sharing their insights into the JICF instabilities while their paper was under review.

Measurements of the flow field were important in determining the instability suppression mechanism. The occurrence of the phenomenon is independent of synthetic jet forcing frequency, but instead is linked to the addition of momentum from the synthetic jet. More momentum is needed to suppress the instabilities at lower velocity ratios due to the growth and increased influence of a non-negligible velocity deficit in the upstream jet shear layer profile close to the stack exit plane. The additional momentum modifies the jet shear layer profile close to the stack exit to reduce the local Reynolds number of the profile. Once the Reynolds number is below a critical value for the jet instabilities to occur, relaminarization results.

The effect of the synthetic jet on the time-averaged jet shear layer profile appears to have many similarities to base bleed suppression of Kármán vortex shedding in two-dimensional wake flows. Continuous fluid injected through the annulus does indeed relaminarize the elevated JICF as well. It is interesting that the relaminarization of the three-dimensional JICF flow closely resembles what is usually regarded as a primarily two-dimensional phenomenon. However, in the near field the Reynolds numbers are expected to be highest along the plane of symmetry on the upstream side of the JICF, so it may be here where the JICF instabilities will first form.

It should be noted that suppression of the instability only occurs in the near field. As is the case with all open flows above a critical Reynolds number, the relaminarized JICF will eventually transition to turbulence as the flow convects downstream. Therefore, the synthetic jet may inhibit the growth of instabilities in the near field of the elevated JICF, but it only delays the flow's eventual transition to turbulence.

5.3 Digitization of the Three-Dimensional Large-Scale Structures

In "Digitization of jet-in-crossflow jet shear layer vortex structure via Augmented Reality" a "mixed reality" interface (Milgram et al., 1994) consisting of a stereoscopic flow image and a virtual three-dimensional cursor was used to extract some spatial features of the three-dimensional vortex tube structure in the unforced elevated JICF jet shear layer. The study is, to the author's knowledge, the first time that the three-dimensional nature of the elevated jet shear layer vortices has been explored.

The large-scale jet shear layer structure appears to be composed of a periodically reoccurring arrangement of vortices which originate from the jet column and from separated flow on the leading edge of the outer stack wall. Stereoscopic visualization allowed for a new interpretation of the vortex structure in order to determine the connections between the vortices. The three-dimensional structure consists of a vortex ring containing vorticity from the jet column surrounded by a vortex loop of outer stack vorticity. The vortex ring evolves in the near field into a configuration which is similar to the saddle arrangement proposed by Kelso et al. (1996) for ground-level JICFs. The vortex loop appears to be a unique component of the structure which has not been observed in other JICF geometries, however we are limited in what we can say about the structure due to the limitations of the tracer method employed in the experiment. The ends of the vortex loops are lost below the the area marked by the smoke tracer, but we believe that the loops may be connected in some way to vortices in the stack wake.

5.4 Further Research

The following are suggested as future work for the project:

- *Flow control of a wall-issued JICF with annular blowing*: A possible avenue for investigation is to apply the forcing technique to the wall-issued case. Present methods of JICF control in this geometry require special temporal programming of the actuator via active control to modify the wall-issued JICF structure at low velocity ratios (M'Closkey et al., 2002). Changes in the forced low momentum JICF vortex structure appear to agree with the ideas of Gharib et al. (1998) on the existence of a universal time scale required for the generation of vortex rings used for forcing (Shapiro et al., 2006; Johari, 2006). The annular geometry may have some advantages over other proposed methods of control in this regard. Also, Megerian et al. (2006) report that the spectral characteristics of the instabilities in the wall and elevated cases are similar at low velocity ratios. Perhaps suppression of the jet instabilities by annular synthetic jet forcing or base bleed would work in the wall-issued case as well.

- *Field measurements with PIV*: A form of Image Correlation Velocimetry was used in this study to determine velocity fields of the JICF. The method was useful for carrying out initial exploratory work on the low momentum JICF field, however there were drawbacks related to errors in the velocity measurements and not being able to extract measurements of the entire velocity field due to 3-D effects. More refined measurements of the flow field could be made using Particle Imaging Velocimetry and a laser sheet to image the flow.
- *JICF instabilities*: An interesting hypothesis been drawn from the relaminarization experiments in Chapter 3 related to the possible existence of a global JICF instability at these low velocity ratios. Further work could be rewarding from a fundamental perspective. The author suggests that the reader consult Huerre and Monkewitz (1990) and Schumm et al. (1994) for possible strategies to approach the problem.
- *Determination of complete elevated JICF large scale structure*: We have only begun the process of creating a model for the low momentum elevated JICF's large-scale structures. The Augmented Reality technique has shown promise. Visualization of the vorticity shed from the outer stack wall boundary layer into the stack wake could reveal the possible connection between vortices in the stack wake and vortices in the jet shear layer.

BIBLIOGRAPHY

Diep, J. and Sigurdson, L. (2001). Cross-jet influenced by a concentric synthetic jet. *Physics of Fluids*, 13(9):S16.

Diep, J. and Sigurdson, L. (2002). *Low velocity ratio transverse jets influenced by concentric synthetic jets.* Manipulation and Control of Jets in Crossflow, CISM Courses and Lectures No. 439. International Centre for Mechanical Sciences.

Gharib, M., Rambod, E., and Shariff, K. (1998). A universal time scale for vortex ring formation. *Journal of Fluid Mechanics*, 360:121–40.

Huang, R. F. and Lan, J. (2005). Characteristic modes and evolution processes of shear-layer vortices in an elevated transverse jet. *Physics of Fluids*, 17(3):034103.

Huerre, P. and Monkewitz, P. A. (1990). Local and global instabilities in spacially developing flows. *Annual Review of Fluid Mechnaics*, 22:473–537.

Johari, H. (2006). Scaling of Fully Pulsed Jets in Crossflow. *AIAA Journal*, 44(11):2719–25.

Kelso, R. M., Lim, T. T., and Perry, A. E. (1996). An experimental study of round jets in cross-flow. *Journal of Fluid Mechanics*, 306:111–44.

M'Closkey, R. T., King, J. M., Cortelezzi, L., and Karagozian, A. R. (2002). The actively controlled jet in crossflow. *Journal of Fluid Mechanics*, 452:325–35.

Megerian, S., Davitian, J., de B. Alves, L. S., and Karagozian, A. R. (2006). Transverse jet shear layer instabilities - Part I: Experimental studies. to appear in the *Journal of Fluid Mechanics.*

Milgram, P., Takemura, H., Utsumi, A., and Kishino, F. (1994). Augmented reality: a class of displays on the reality-virtuality continuum. In *Proceedings of SPIE Telemanipulator and Telepresence Technologies*, volume 2351, Boston, MA.

Schumm, M., Berger, E., and Monkewitz, P. A. (1994). Self-excited oscillations in the wake of two-dimensional bluff bodies and their control. *Journal of Fluid Mechanics*, 271:17–53.

Shapiro, S. R., King, J. M., M'Closkey, R. T., and Karagozian, A. R. (2006). Optimization of controlled jets in crossflow. *AIAA Journal*, 44:1292–8.

Appendix A

Low Speed Hot-wire Calibration

A.1 Background

A 1.25 mm long, 5 μm diameter, single-component hot-wire (Dantec Dynamics, platinum-plated tungsten, type 55P1) was used to obtain low velocity measurements of the flow field. In principle, the favorable sensitivity, frequency response, and spatial resolution characteristics of a hot-wire make it a accurate method for low velocity investigations. In practise, however, complications arise that require special approaches to make measurements to a high degree of confidence.

The conventional hot-wire calibration method is to use a pitot-static tube as a velocity standard, where the flow velocity is determined by a pressure difference. However, when the velocity becomes smaller than 1 m/s, which is within the domain of the present measurements, the pressure difference becomes small (less than 1 Pa) and it is difficult to obtain an accurate velocity reading. For example, at 1 m/s a Setra Model 264 ±0.1 in.WC pressure transducer has approximately 10% error in its pressure reading. An alternative method was needed to carry out the calibration.

Several methods are in the literature for low speed hot-wire calibration; the two most popular methods are discussed here. Perry (1982) proposed that the hot-wire be placed in the settling chamber of the wind-tunnel upstream of the contraction. The velocity is measured by a pitot-static tube in the test section where the velocity is higher. Using this method, it would be possible to obtain a speed reduction of 1:6 in the wind-tunnel used in this study. Conservation of mass is used to determine the hot-wire velocity, however it is necessary to check flow uniformity across where the two probes are placed and to compensate for boundary layer growth. The second method, successfully used by Roshko (1954), utilizes periodic vortex shedding behind a cylinder in a crossflow at low Reynolds number. Typically, a cylinder that has a nominal diameter of 3 mm is spanned across the tunnel test section. The tunnel velocity is determined by measuring the cylinder shedding frequency with a hot-wire signal post-processed via Fast Fourier Transform analysis. The relationship that links shedding frequency to Reynolds number is well known (Roshko, 1954; Williamson, 1989). This method is attractive since it relies on a well understood physical phenomenon. Additionally, Roshko (1954) also reported high accuracies especially for velocities lower than 0.4 m/s. However, there are drawbacks. It is assumed that the frequency follows the shedding relationship for an infinite cylinder, however if the cylinder is not designed carefully end effects will cause non-parallel vortex shedding behind the cylinder causing inaccuracies in the calibration (Williamson, 1989). Lee and Budwig (1991) have suggested improvements to the method using end modifications to account for these factors, however regardless of this, the cylinder apparatus must be carefully designed, mounted and tested over a range of crossflow speeds before it can be used with high degree of confidence as a measurement standard.

A.2 Method and Results

The calibration methods described above require carefully designed equipment that was not available. An alternative calibration method was developed which leveraged equipment already in operation in the lab. The velocity standard used in the low speed hot-wire calibration in this experiment was horizontal velocity measurements of in situ generated streaklines using image correlation velocimetry (the method was reviewed in Section 3.2.4. With all obstructions removed from the wind-tunnel test section, a vertically mounted 0.005 in. diameter smoke-wire was fitted into the wind-tunnel test section a short distance downstream from the contraction. The hot-wire to be calibrated was also mounted in the wind-tunnel test section with the wire perpendicular to the crossflow. The hot-wire was placed three inches downstream from the smoke-wire, moved off to one side such that it was in a region of unform flow unaffected by perturbations in the free stream caused by the smoke-wire. A Nikon D1X camera and a 105 mm lens connected to a timing box provided high resolution photographs of the streaklines at a resolution of 410 pixels/cm. It was not difficult to obtain accurate velocity readings from the magnified streakline photographs since the small oscillations in the streaklines, likely generated from small perturbations in the crossflow, were clear and distinguishable. Shedding behind the smoke-wire was also not a problem over the calibration range in this experiment (from 0 to 3 m/s) since the Reyonlds number of the smoke-wire ($0 \leq \mathrm{Re} \leq 24$) stayed below the critical Reynolds number where Kármán vortex shedding occurs. Any effect caused by a velocity defect due to a wake profile behind the smoke-wire was minimised by carrying out measurements at least three inches downstream from the smoke-wire (or 600 wire smoke-wire diameters), where the wake has been given time to dissipate. The time between the firing of the red and blue strobes was set for each crossflow velocity to insure that the error in the velocity due to pixel error was kept approximately constant at 1.5% of reading. An average of six vectors were used to determine each value of the standard crossflow velocity. Overall, the time of flight method described here worked well over the calibration range, except below 8 cm/s where buoyancy affected the results.

Figure A.1 shows the hot-wire calibration curve for the low velocity range $0\ \mathrm{m/s} \leq U_\infty \leq 3\ \mathrm{m/s}$ and a overhead ratio of 1.3. For high velocities, heat transfer from the sensor is dominated by forced convection. However, when the flow velocity is reduced, the hot-wire comes upon a mixed-flow regime in which both forced and natural convection influences the hot-wire response. The calibration law of Ligrani and Bradshaw (1987) is used here to plot the calibration data. For the forced convection regime, data is plotted based on "King's Law" with the equation

$$E^2 = A + BU^{0.45} \tag{A.1}$$

In this case, the coefficients $A = 2.246$ and $B = 1.447$ gave good agreement. For the mixed-flow regime, the calibration data is approximated by the third-order polynomial

$$\alpha = a_o + a_1\beta + a_2\beta^2 + a_3\beta^3 \tag{A.2}$$

where $\alpha = U^{0.45}$ and $\beta = E^2 - A$. The lower limit of the forced convection regime is where the calibration data deviates from the line representing King's Law (eqn A.1). In this case, the lower Reynolds number limit, Re_c, for the forced convection regime is $\mathrm{Re}_c = 0.07$, which is in agreement with Ligrani and Bradshaw (1987).

A disadvantage that should be noted in the present calibration is that the method required the use of a horizontal free stream, however, subsequent

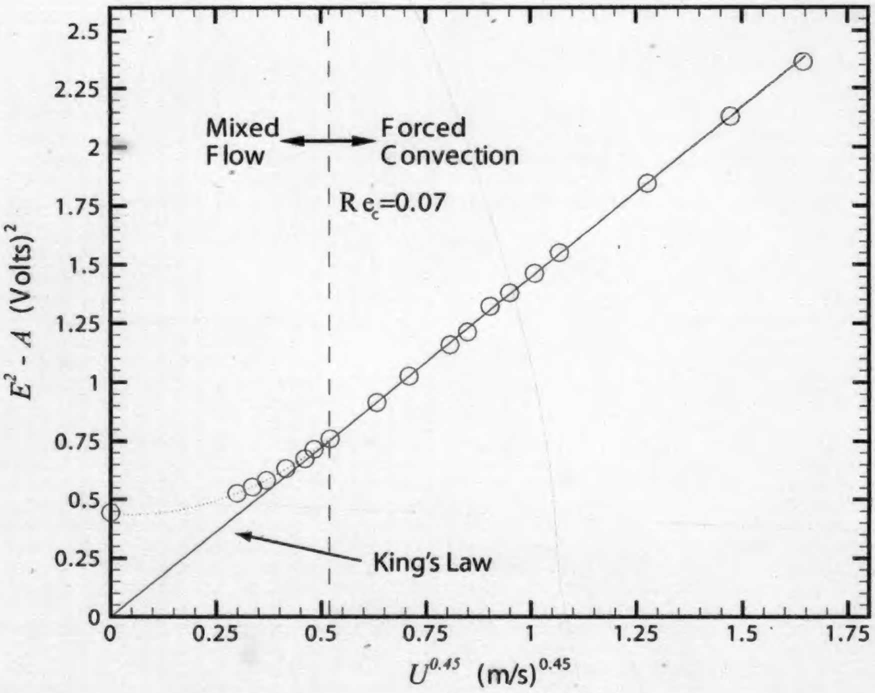

Figure A.1: Hot-wire calibration for the range 0 m/s $\leq U \leq$ 3 m/s and an overheat ratio of 1.3. The hot-wire is a Dantec Dynamics type 55P11 (1.25 mm long, 5 μm diameter). The vertical line represents the lower limit where forced convection dominates, at a lower Reynolds number limit $\mathrm{Re_c}$ = 0.07. Below this value the hot-wire is in a mixed-flow regime in which both forced and natural convection influence its response.

measurements with the calibrated hot-wire were made in vertical flows. The effect of probe orientation in both low velocity vertical and horizontal flows was studied by Christman and Podzimek (1981). Their studies with a similar single wire probe (DISA 55P11), but at a higher overheat ratio of 1.8, demonstrated that there was a small but consistent difference in the hot-wire reading over the range 1 cm/s to 10 cm/s that depended on flow orientation. Their work also looked at differences in the hot-wire response between upwards and downwards flows. A more pronounced, consistent difference of approximately 12% full scale at 10 cm/s was reported over the same velocity range. It was suggested the difference for upward and downward flow is caused by the natural convection velocity being added to or subtracted from the forced convection velocity. In any case, this disadvantage is common amongst all low speed insitu methods used for hot-wire calibration and translated into approximately a 3% error in the velocity reading in the lowest velocity fluctuations recorded in the experiment.

BIBLIOGRAPHY

Christman, P. J. and Podzimek, J. (1981). Hot-wire anemometer behaviour in low velocity air flow. *Journal of Physics E (Scientific Instruments)*, 14(1):46–51.

Lee, T. and Budwig, R. (1991). Two improved methods for low-speed hot-wire calibration. *Measurement Science and Technology*, 2:643–46.

Ligrani, P. M. and Bradshaw, P. (1987). Subminiature hot-wire sensors: development and use. *Journal of Physics E (Scientific Instruments)*, 20:323–32.

Perry, A. E. (1982). *Hot-wire Anemometry.* Oxford Science Publications.

Roshko, A. (1954). On the development of turbulent wakes from vortex streets. *NACA Report 1191*, pages 801–25.

Williamson, C. H. K. (1989). Oblique and parallel modes of vortex shedding in the wake of a circular cylinder at low Reynolds numbers. *Journal of Fluid Mechanics*, 206:579–627.

APPENDIX B

JICF TRAJECTORIES

B.1 Background

Scaling the JICF trajectory has been the objective of numerous studies. It is customary to scale the JICF trajectory based on the experimental observations of Pratte and Baines (1967). Using photographs of flood-lit jet-seeded smoke to define the centreline, Pratte and Baines (1967) demonstrated that the length scale RD could be used to collapse the trajectories at different R. Their results were confirmed by the experiments of Broadwell and Breidenthal (1984) and later by Smith and Mungal (1998) for wall-issued and elevated JICFs. However, the scaling has only been tested for turbulent JICF in the far field where the jet exit can be considered as a point source of momentum flux. In the near field, Keffer and Baines (1963) reported considerable success using the JICF momentum ratio, R^2, to collapse the trajectories of high momentum wall-issued JICFs, but for the low momentum cases ($R < 2$) the trajectories were lower than the proposed scaling due to the greater influence of pressure forces on the trajectory.

An alternative approach is to model the trajectory. The "Briggs 1/3 law for bent-over jets" was formulated by Briggs (1975) to predict the trajectory of turbulent, non-buoyant plumes from elevated stacks. The semi-empirical model has since been used by many others to model plume dispersion from large scale stacks and laboratory model studies. The model works best for high momentum, elevated JICF in the far field, however Overcamp and Ku (1986) has reported some success in the near field if a virtual origin correction is implemented. In the semi-empirical model, the jet height scales with the fixed parameter $x^{1/3}$ (x is in the cross-stream flow direction) and a "variable entrainment coefficient" is used as an adjustment parameter to account for different behaviour of JICF at different R. For lower velocity ratios, $R < 1.5$, Johnston and Wilson (1997) proposed modifying the Briggs law with an additional theory to account for the enhanced effect of downwash on the plume trajectory. The trajectory profiles in the adjusted model were predicted using an entrainment coefficient and an additional parameter named the "downwash correlation coefficient" which was also determined from empirical data. Agreement of the model with experiments was good, which is to be expected considering the two adjustable parameters.

B.2 Determining JICF Trajectories

Approximate near field jet trajectories based on scalar concentration were determined from side-view photographs of the JICF with jet-seeded flow. The data was obtained from an averaged photograph of at least fifty instantaneous photographs of the smoke field. A sample averaged photograph is in Figure B.1(a). The influence of the region of uniform concentration distribution was not neglected in the analysis. In the near field of the unstable JICFs, the region of uniform scalar concentration comprises of a considerable portion of the vertical jet width. The region's effect on the measurement is more pronounced for stable JICFs since there is negligible mixing of the crossflow and jet fluid in the near field. Theoretically, the uniform scalar region should contain an even distribution of the maximum concentration in the jet's concentration profile. As a consequence, the mean distance between the upstream and downstream boundaries of the region of uniform concentration were chosen to be the scalar centreline, along which the approximate JICF trajectory was based. Figure B.1(b) shows a profile of the pixel intensity taken along a horizontal line passing through the photograph in Figure B.1(a) at $z/h = 2$. The steep drop-offs in the pixel intensity corresponds to the upstream and downstream boundaries. The upstream and downstream boundaries of the region of uniform concentration were determined along the streamwise direction in the near field up to the point where the region ceased to visually exist. Then, a fourth degree polynomial signifying the scalar trajectory (or the average of the boundaries) was fit to the data using linear regression. The method used here only allows for the measurement of an approximate trajectory in the near field, however the measurement domain was adequate for our measurements. It should also be noted that the jet trajectory was not determined by tracking the locations of maximum pixel intensities in the averaged photographs. The photographs were taken with columnated light,

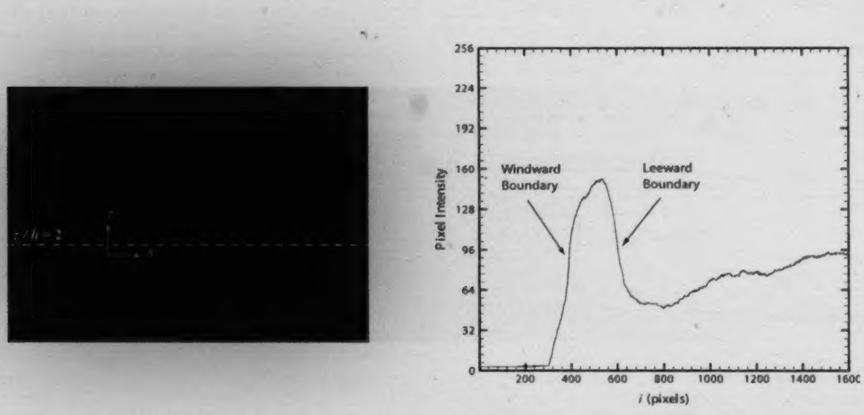

(a) (b)

Figure B.1: A sample image used to determine the JICF trajectory. (a) Case BA, $R = 0.75$. The image is an average of 50 instantaneous photographs. (b) An pixel intensity profile along a horizontal line passing through $z/h = 2$. The upstream and downstream boundaries of the region of unform scalar concentration are discernible.

therefore in the photographs information is integrated along the light path. The jet column develops into a kidney shape not far after leaving the stack exit. This could especially effect intensity measurements in the centre of the jet column.

It should be noted that the authors were unable to find a standard method in the literature to determine the scalar centreline of low momentum, elevated JICF. Methods developed in other studies are for strong, turbulent JICF and measurements are usually made in the far field. In any case, the approach used here to determine the scalar trajectory is non-standard in two respects. First, a fourth degree polynomial function was used to define the approximate jet trajectory rather than fitting the data to a scaling law found in the literature. This was a practical consideration since scaling laws in the literature are for strong, turbulent jet flows and not for the cases in this study. A low momentum elevated JICF's trajectory is influenced by a number of factors, such as downwash and inner pipe separation, which are neglected in present trajectory models. Secondly, a laser sheet was not used to image the symmetry plane ($y = 0$), therefore the side view photograph is an integration of the three dimensional structure of the JICF. A concern is the kidney shape that begins to develop a short time after the jet fluid exits the pipe. In the near field the kidney shape is in the initial stages of development, however it is expected that the scalar trajectory may be slightly higher that what was measured. Before the advent of laser technology flood lighting was the standard method for trajectory measurements. Several studies have used flood lighting to make trajectory measurements, including Vadot (1967); Fan (1967); Overcamp and Hoult (1971); Hoult and Weil (1972); Pratte and Baines (1967). The results of Pratte and Baines (1967) are still extensively cited in the literature and are the basis of scaling laws that are commonly used in the literature (Hasslebrink and Mungal, 2001; Su and Mungal, 2004; Smith and Mungal, 1998).

B.3 Results and Discussion

Plots of the approximate near field jet trajectories of the unforced JICFs are shown in Figure B.2. The axes are normalized by stack diameter, D. As expected, the trajectories are lower with decreasing velocity ratio. Near the stack, the trajectories also do not intersect the stack centreline at the exit plane, but instead are "pushed" further downstream by stronger crossflows as velocity ratios decrease. The measurements suggest that in these conditions bending of the streamlines may begin when the jet flow is still inside the stack and that flow separation of jet flow on the upstream side may occur. The deflection angle of the JICF is quite severe which suggests the existence of a strong pressure force pushing the jet downstream. If this is true, an adverse pressure gradient may exist just above the upstream side of the stack exit that would have an effect on the in-stack flow profile. Static pressure measurements coupled with velocity measurements upstream of low momentum, wall-issued JICFs have proven the existence of severe pressure gradients with streamline curvature and regions of flow separation (Andreopoulos, 1982; Kelso et al., 1996). Similar pressure measurements for the elevated case are more difficult to obtain, therefore no further work was done in measuring the phenomenon other than these preliminary observations. In any case, the measurements demonstrate that a trajectory model based on the assumption of the JICF emanating from a point source, like the models used for strong JICF, are not applicable under these conditions. Perhaps the "virtual origin correction" technique of Overcamp and Ku (1986) could be used for low momentum JICFs to correct the trajectory models in the near field, however,

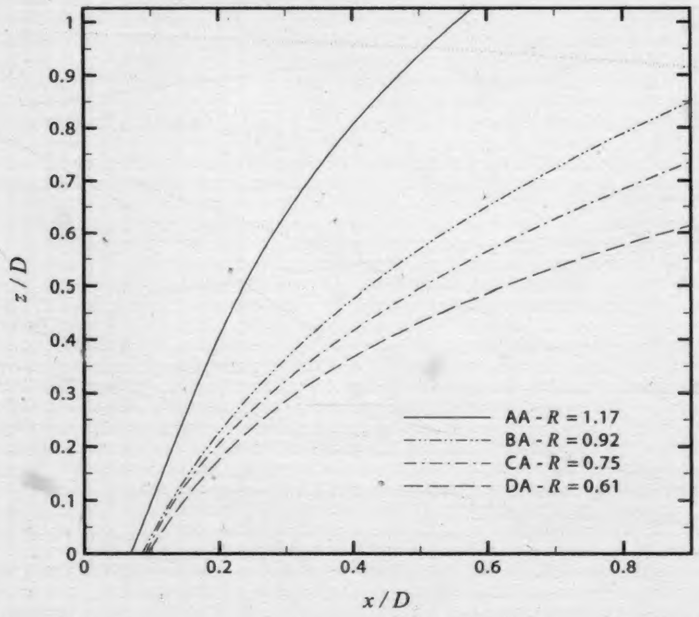

Figure B.2: A comparison of approximate unforced jet trajectories. Jet penetration decreases with reductions in the velocity ratio.

the utility of applying such a correction was not explored.

Figure B.3 compares the trajectories of the 'C' series test cases. Shown are the unforced case CA and the corresponding relaminarized trajectories (CB-CD). The trajectory for case AA is also included for comparison. The forced cases show a noticeable increase in penetration when compared to the unforced trajectory CA. This increase is likely due to additional of upward momentum from the synthetic jet. Cases CB-CD have similar trajectories in the near field, however, they do not penetrate as deeply as the unforced case AA. It appears that the additional synthetic jet momentum flux is not enough to bring the combined jet and synthetic jet flow up to a velocity ratio of $R \approx 1.17$. The relaminarized flows in cases BB-BD and DB-DD have a similar trend to the 'C' series data. Overall, the forced, relaminarized JICF have trajectories that penetrate into the crossflow deeper than their initial unforced cases, but their trajectories do not approach the height of the unforced case AA. The result is interesting because both the forced JICF and the unforced JICF in case AA have stable jet shear layers, however, the trajectories at which the flows are stable are different. In any case, these observations gives a clue why suppression of the jet shear layer instability may not occurring. The studies of Andreopoulos and Rodi (1984) suggest that there is an effect of streamline curvature on the JICF turbulence. When the velocity increases in the positive direction of the radius of curvature it is stabilizing, however when the velocity decreases in the direction of radius of curvature the effect is destabilizing. The fact that the radius of curvature is is different for the stable cases lends to the conclusion that, in this case, streamline curvature on the (x, z) plane does not play a large role in the suppression of the instability for this phenomenon.

For the measurements presented in this report it was a requirement to check the accuracy of the scalar centrelines close to the exit plane and to determine the viability of using the measurement as a reasonable approximation of jet quantities which should be based on velocity fields. The scalar trajectory was checked against velocity profile measurements taken with a hot-wire along the symmetry plane at $z/h = 2$. The results of the comparison, which compare the values at a single point along the trajectory, are shown in Table B.1. It should be noted that the point signifying the location of the maximum velocity in the profile is probably not on a *centre streamline*, a line tangential to the time-averaged velocity field which originates at the centre of the stack exit. There is reasonable agreement near the exit plane at $z/h = 2$ between the scalar centreline and the point of maximum velocity in the jet profile, considering the spacial resolution in the profile measurement $(x/D = \pm 0.039)$. Direct comparison of the values gives differences of approximately 1.5-25%. To estimate the suitability of using the scalar centreline to determine JICF profile quantities, such as the thickness of the viscous region on the upstream side, the origin of the measurements was shifted from the centre of the stack to the stack leading edge. Although this is not the actual viscous thickness of the jet profile, the measurement is the same order of magnitude. Errors in using the scalar centreline drop to approximately 0.3 to 6%.

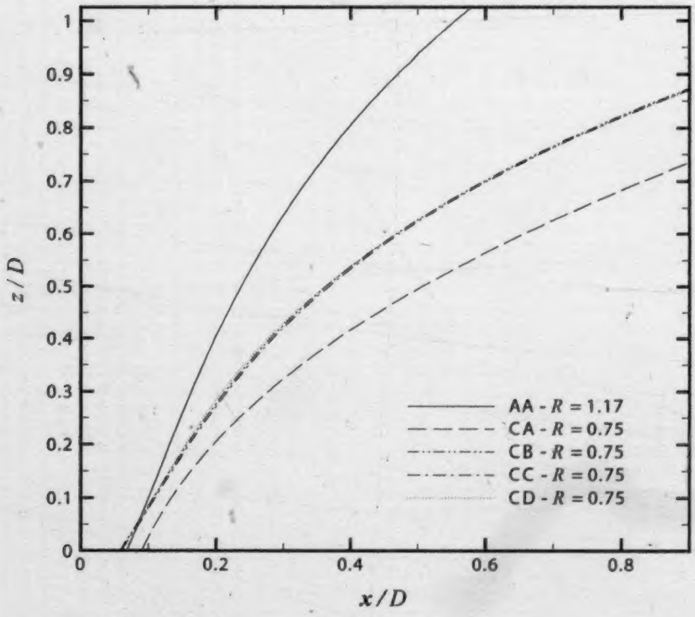

Figure B.3: A comparison of approximate jet trajectories at an initial velocity ratio of $R = 0.65$. The trajectory for $R = 1$ is also been included for reference. Forced trajectories have higher penetration than the unforced case.

Table B.1: Comparison of Scalar and Velocity Centrelines: The table displays errors in using the scalar centreline to approximate the peak velocity in the JICF profile. The velocity centreline is based on the maximum velocity in the velocity profile, and is not the centre streamline which originates at the centre of the stack at $x/D = 0$. The errors are determined by assuming the velocity centreline is the actual value.

	Measurements at $z/h = 2$	
	% Error	
Case	wrt. Stack Centre, $x/D = 0$	wrt. Stack LE, $x/D = -0.5$
AA	7.7	1.4
BA	8.8	2.1
BB	3.0	0.6
BC	1.5	0.3
BD	24.9	5.9
CA	4.9	1.2
CB	2.9	0.6
CC	21.3	5.1
CD	23.1	5.5
DA	15.4	4.3
DB	21.0	5.9
DC	15.8	4.5
DD	4.7	1.1

BIBLIOGRAPHY

Andreopoulos, J. (1982). Measurements in a jet-pipe flow issuing perpendicularly into a cross stream. *Transactions of the ASME. Journal of Fluids Engineering*, 104:493–99.

Andreopoulos, J. and Rodi, W. (1984). Experimental investigation of jets in a crossflow. *Journal of Fluid Mechanics*, 138:93–127.

Briggs, G. (1975). *Plume rise predictions, Lectures on Air Pollution and Environmental Impact Analyses*, pages 59–111. American Meteorological Society.

Broadwell, J. E. and Breidenthal, R. E. (1984). Structure and mixing of a transverse jet in incompressible flow. *Journal of Fluid Mechanics*, 148:405–12.

Fan, L. N. (1967). Turbulent Buoyant Jets into Stratified or Flowing Ambient Fluids. Technical report, W. M. Keck Laboratory of Hydrodynamics and Water Resources, California Institute of Technology, Pasadena, CA. Report KH-R-15.

Hasslebrink, E. F. and Mungal, M. G. (2001). Transverse jets and jet flames. Part 1. Scaling laws for strong transverse jets. *Journal of Fluid Mechanics*, 443:1–25.

Hoult, D. and Weil, J. (1972). Turbulent plume in a laminar cross flow. *Atmospheric Environment*, 6:513–31.

Johnston, C. R. and Wilson, D. J. (1997). A vortex pair model for plume downwash into stack wakes. *Atmospheric Environment*, 31(1):13–20.

Keffer, J. F. and Baines, W. D. (1963). The round turbulent jet in a crosswind. *Journal of Fluid Mechanics*, 15(4):481–96.

Kelso, R. M., Lim, T. T., and Perry, A. E. (1996). An experimental study of round jets in cross-flow. *Journal of Fluid Mechanics*, 306:111–44.

Overcamp, T. and Hoult, D. (1971). Precipitation in the wake of cooling towers. *Atmospheric Environment*, 5:751–65.

Overcamp, T. J. and Ku, T. (1986). Effect of a virtual origin correction on entrainment coefficients as determined from observations of plume rise. *Atmospheric Environment*, 20(2):293–300.

Pratte, B. D. and Baines, W. D. (1967). Profiles of round turbulent jet in cross flow. *American Society of Civil Engineers Proceedings, Journal of the Hydraulics Division*, 92:53–64.

Smith, S. H. and Mungal, M. G. (1998). Mixing, structure and scaling of the jet in crossflow. *Journal of Fluid Mechanics*, 357:83–122.

Su, L. K. and Mungal, M. G. (2004). Simultaneous measurements of scalar and velocity field evolution in turbulent crossflowing jets. *Journal of Fluid Mechanics*, 513:1–45.

Vadot, L. (1967). Étude de la Diffusion des Panaches de Fumée dans l'Atmosphère. Technical report, Centre Interprofessionnel Technique d'Études de la Pollution Atmosphérique, Paris.